UNIVERSITY OF SALAMANCA

Department of Cartographic and Land Engineering

INTERNATIONAL PhD DISSERTATION

Close-range Photogrammetry applied to Agroforestry Engineering

Mónica Herrero Huerta

Supervised by:

Dr. Diego González Aguilera

Dr. David Hernández López

2016

Department of Cartographic and Land Engineering

Higher Polytechnic School of Avila

University of Salamanca

AUTHOR:

Mónica Herrero Huerta

SUPERVISORS:

Dr. Diego González Aguilera

Dr. David Hernández López

2016

This Doctoral Thesis consists of a compendium of 3 scientific papers published in international journals of high impact factor which are specified below.

1. **Vicarious Radiometric Calibration of a Multispectral Sensor from an Aerial Trike Applied to Precision Agriculture**

   Mónica Herrero-Huerta[1], David Hernández-López[2], Pablo Rodriguez-Gonzalvez [1], Diego González-Aguilera[1], José González-Piqueras[2]

   [1]Department of Cartographic and Land Engineering, University of Salamanca, Higher Polytechnic School of Avila, Hornos Caleros 50, 05003, Avila, Spain.

   [2]Institute for Regional Development (IDR), University of Castilla La Mancha,02071,Albacete, Spain

   Computers and Electronics in Agriculture 108 (2014) 28–38

   doi:10.1016/j.compag.2014.07.001

2. **Vineyard Yield Estimation by Automatic 3D Bunch Modelling in Field Conditions**

   Mónica Herrero-Huerta[1], Diego González-Aguilera[1], Pablo Rodriguez-Gonzalvez[1] David Hernández-López[2]

   [1]Department of Cartographic and Land Engineering, University of Salamanca, Higher Polytechnic School of Avila, Hornos Caleros 50, 05003, Avila, Spain.

   [2]Institute for Regional Development (IDR), University of Castilla La Mancha, 02071, Albacete, Spain

   Computers and Electronics in Agriculture 110 (2015) 17–26

   doi:10.1016/j.compag.2014.10.003

3. **Dense Canopy Height Model from a low-cost photogrammetric platform and LiDAR data**

   Mónica Herrero-Huerta[1], Beatriz Felipe-García[2], Soledad Belmar-Lizarán[2], David Hernández-López[2], Pablo Rodriguez-Gonzalvez [1], Diego González-Aguilera[1]

   [1]Department of Cartographic and Land Engineering, University of Salamanca, Higher Polytechnic School of Avila, Hornos Caleros 50, 05003, Avila, Spain.

   [2]Institute for Regional Development (IDR), University of Castilla La Mancha, 02071, Albacete, Spain

   Trees

   Doi: 10.1007/s00468-016-1366-9

To the Great Crested Grebe, page 8, "In the pond"

«It is not the strongest of the species that survives, nor the most intelligent that survives.
It is the one that is most adaptable to change»

(Charles Darwin)

Acknowledgements

To all who feel identified. Thanks from my heart.

Abstract

Since the late twentieth century, Geotechnologies are being applied in different research lines in Agroforestry Engineering aimed at advancing in the modeling of biophysical parameters in order to improve the productivity. In this study, low-cost and close range photogrammetry has been used in different agroforestry scenarios to solve identified gaps in the results and improve procedures and technology hitherto practiced in this field. Photogrammetry offers the advantage of being a non-destructive and non-invasive technique, never changing physical properties of the studied element, providing rigor and completeness to the captured information.

In this PhD dissertation, the following contributions are presented divided into three research papers:

- A methodological proposal to acquire georeferenced multispectral data of high spatial resolution using a low-cost manned aerial platform, to monitor and sustainably manage extensive áreas of crops.

  The vicarious calibration is exposed as radiometric calibration method of the multispectral sensor embarked on a paraglider. Low-cost surfaces are performed as control coverages.

- The development of a method able to determine crop productivity under field conditions, from the combination of close range photogrammetry and computer vision, providing a constant operational improvement and a proactive management in the crop monitoring.

  An innovate methodology in the sector is proposed, ensuring flexibility and simplicity in the data collection by non-invasive technologies, automation in processing and quality results with low associated cost.

- A low cost, efficient and accurate methodology to obtain Digital Height Models of vegatal cover intended for forestry inventories by integrating public data from LiDAR into photogrammetric point clouds coming from low cost flights.

  This methodology includes the potentiality of LiDAR to register ground points in areas with high density of vegetation and the better spatial, radiometric and temporal resolution from photogrammetry for the top of vegetal covers.

Keywords: vicarious calibration, multispectral sensor, low-cost platform, reflectance, photogrammetry, computer vision, automation, non-invasive technologies, digital height model of vegetal cover, data fusion, LiDAR, radiometric segmentation.

CONTENTS

1. Introduction 19

2. Work hypotheses and objectives 25

2.1. Hypotheses 25

2.2. Objectives 25

3. Scientific papers 30

4. Conclusions and future works 71

Appendix A. Congress publications, ISPRS 2015 77

Appendix B. Indexation and impact factor of the publications 91

Appendix C. MULRACS sotware 100

Appendix D. Extra merits 106

I. Introduction

1. INTRODUCTION

Since the last decade of the twentieth century, research lines on the applicability of Geotechnologies to Agroforestry Engineering have been developed, in order to optimize agroforestry, environmental and economic management. In this PhD dissertation, contributions advancing in the direction of the application of methodologies derived from low-cost and close range photogrammetry in this field are made. Thus, numerous information is available regarding to filed monitoring, aids to making decisions and traceability requirements and improving the intrinsic quality of agricultural and forestry derived products.

Three case studies have been raised, generating a continuity in the research presented by this PhD dissertation:

- multispectral aerial photogrammetry for agronomic analysis: low-cost and close range photogrammetry over large crop areas through paraglider. The spectral range of the study is among the visible and near infrared (NIR), optimal range for vegetation studies that enables deriving vegetation indices. The contribution of this research line focuses on one of the first problems to be solved in the use of multispectral cameras boarded on aerial platforms: the radiometric calibration of the sensors which allows to obtain physical quantities from digital levels stored in the images. At the same time, it aims to advance in the convergence of photogrammetry and remote sensing.
- Terrestrial photogrammetry to estimate agricultural production: low-cost and close range photogrammetry by reflex and compact digital cameras. The contribution to this research line addresses the problem posed by the imprecision in crop predicting enough in advance for proper planning of the harvest. The experiment was conducted in a vineyard and variables as volume, weight and number of berries associated to each cluster are estimated.
- Aerial photogrammetry for forest management: low cost and close range photogrammetry through paraglider over large forest extension to forest inventory

applications. The contribution in this line of research line aims to develop a methodology that combines low cost aerial photogrammetry and LiDAR existing data to be applied to forest inventory. Thereby, exploiting the advantages of both techniques is possible: on one hand, terrain LIDAR information constant in time is extracted; and on the other hand, modeling of vegetal cover is achieved at the required time thanks to the low-cost offered by photogrammetry. The case study is an area of *pinus nigra.*

II. Work hypotheses and objetives

2. WORK HYPOTHESES AND OBJECTIVES

2.1. Hypotheses

Following an introduction in which a short overview of these applications based on low cost and close-range photogrammetry to Agroforestry Engineering are shown, a series of hypotheses that seek to verify the proposed methodologies are posed:

- Incorporation of aerial low cost and multispectral close range (visible and NIR) photogrammetry to agroforestry studies is an excellent technique to obtaine georeferenced and metric information with the required temporal, spatial and spectral resolution.

- Through terrestrial low cost and close-range photogrammetry and computer vision algorithms is possible to estimate crop production in field conditions and semi-automatically, particularly vineyards, by metrically modeling complex agronomic scenarios.

- By integrating point clouds from LiDAR open data and the photogrammetric output from an alternative platform, it is possible to quickly and efficiently generate documentation applicable to forest management in the required area and time.

2.2. Objectives

The overall objective of the research is to provide contributions to methodologies based on low cost and close-range photogrammetry in agroforestry scenarios for specific applications.
To achieve this overall objective the following **specific objectives** have been established:

1. Application of low cost and close-range multispectral aerial photogrammetry (visible and NIR) to agronomic analysis:

- adquisition of low cost georeferenced multispectral data with a high spatial resolution over crops.
- vicarious calibration of a low cost multispectral sensor from paraglider through economic control surfaces for crop applications.

2. Application of low cost and close-range photogrammetry to estimate vineyard yield:
   - vineyard yield estimation under field conditions by using a low cost and non-invasive method that serves as support tool to take decisions in advance.
   - 3D bunch modeling through technique hybridization of photogrammetric and computer vision ensuring semi-automatism, flexibility and quality, by a proper tool called PW (Photogrammetry Workbench) developed bt TIDOP research group.
   - development of different techniques of computational geometry for the recovery of the non-visible side of the bunch using convex hull techniques.
   - development of algorithms to estimate vineyards production variables.

3. Application of the low cost and close-range aerial photogrammetry to forest management:
   - development a low cost, efficient and accurate methodology to obtaine Canopy Height Models in the desired area and time, destined for forest inventories.
   - integration of LiDAR terrain open data data with minor temporal variability into photogrammetric point clouds obtained using a low-cost platform.
   - correction model between the two data sources to minimize the georeferencing errors.
   - supervised classification of vegetation based on image colour, using the radiometric values of the point cloud in the visible spectrum. The analysis is based on different digital levels percentages between two pairs of strips (R-G and R-B) according to a reference green.

III. Scientific papers

3. SCIENTIFIC PAPERS

Below, the three scientific papers published in hight impact journals are presented.

Computers and Electronics in Agriculture 108 (2014) 28–38

Contents lists available at ScienceDirect

Computers and Electronics in Agriculture

journal homepage: www.elsevier.com/locate/compag

Vicarious radiometric calibration of a multispectral sensor from an aerial trike applied to precision agriculture

Mónica Herrero-Huerta [a], David Hernández-López [b], Pablo Rodriguez-Gonzalvez [a,*], Diego González-Aguilera [a], José González-Piqueras [b]

[a] Department of Cartographic and Land Engineering, University of Salamanca, Higher Polytechnic School of Avila, Hornos Caleros 50, 05003 Avila, Spain
[b] Institute for Regional Development (IDR), University of Castilla La Mancha, 02071 Albacete, Spain

ARTICLE INFO

Article history:
Received 18 February 2014
Received in revised form 20 May 2014
Accepted 3 July 2014

Keywords:
Radiometric calibration
Vegetation index images
Precision agriculture
Multispectral sensor
Remote sensing
Vicarious calibration

ABSTRACT

This article proposes a vicarious calibration as a radiometric calibration method using an onboard multispectral sensor and a low-cost manned aerial platform, PPG (powered paraglider) trike. The statistical analysis of the errors shows the precision reached with this methodology. The greatest advantage offered by this type of manned platforms is its flexibility of flight, autonomy and payload capacity, allowing multiple sensors to be integrated without constraints to weight and volume. The results were validated at two different heights in order to verify the solution obtained with the method, demonstrating the insignificance of relative atmospheric influence between the aerial platform and ground using this platform according to the radiative transfer model on a clear and sunny day. At the same time, the study aims to develop a new trend for remote sensing that will assists in decision making for the sustainable management of extensive crop areas using low-cost geomatic techniques. As a result of the radiometric calibration process, georeferenced images with different vegetation indices over vineyards are obtained.

1. Introduction

The possibility of loading multispectral cameras on low-cost manned aerial platforms such as PPG trikes enables highly accurate radiometric studies to be performed. Therefore, it is desirable that the sensor should be subjected a calibration in which the radiometric behavior of each pixel in the different regions of the spectrum is analyzed, using as "ground truth" the radiance obtained on different targets with the calibrated spectroradiometer (Honkavaara et al., 2009). The basis of this behavior lies in the fact that each body has a typical and different pattern of reflected/emitted energy when it is influenced by electromagnetic energy, which distinguishes it from other materials (Chuvieco and Huete, 2009) depending on atmospheric conditions and the sensor characteristics (Biggar et al., 2003).

The main limitation of PPG trikes to make use of methodologies based on quantitative remote sensing is the need to develop radiometric calibration methodologies to obtain validated radiance data. As advantages, PPG trikes are able to acquire higher spatial, spectral and mainly temporal resolution data with a lower associated cost (Hailey, 2005) and, also, the relative atmospheric corrections required for validating the radiance data are likely to be insignificant on a clear and sunny day. The high spatial resolution data available from conventional platforms, such as satellites and manned aircrafts, is usually limited to a Ground-Sample Distance (GSD) of 50 cm/pixel. Instead, PPG trikes are capable of flying lower than a conventional manned aircraft and therefore acquire images of higher resolution, reaching up to 5–10 cm/pixel. In addition, the ease of flight planning permits better temporal resolution than classic photogrammetric flight planning (Hernandez-Lopez et al., 2013). In satellite systems, temporal resolution is limited by the coverage patterns of the satellite's orbit, involving lengthy periods in the delivery of the results (unfavorable temporal resolution) (Berni et al., 2009). Regarding unmanned aerial systems (UAS), the payload capacity and volume of onboard sensors as well as the limited flight autonomy means that the mapping and monitoring of large surfaces and ground covers are unviable. Last but not least, the progress of microelectronics in the field of navigation equipment (GNSS/IMU-Global Navigation Satellite System/Inertial Measurement Unit) has made it possible to provide these low-cost manned platforms with a quality solution to determine the spatial and angular position of the sensors and consequently their trajectory.

A key factor in the suitability of close-range remote sensing for vegetation analysis (i.e. precision agriculture) is based on the fact that such sensing procedures are non-destructive and non-invasive, providing similar accuracy to destructive field methods (Zhang and Kovacs, 2012). More specifically, the spectral signature

* Corresponding author.
E-mail address: pablorgsf@usal.es (P. Rodriguez-Gonzalvez).

http://dx.doi.org/10.1016/j.compag.2014.07.001
0168-1699/

of a given crop is directly related to its phenological, physiological and morphological characteristics, such that any change in the plant will also disturb its reflectance (Lass and Callihan, 1997; Schmidt and Skidmore, 2003). These differences in the intrinsic spectral behavior of each species allow their discrimination and mapping by analysis techniques and digital classification. This is why the spectral signatures of different types of vegetation can be assessed, supported by vegetation indices and the subsequent biophysical magnitudes used in agricultural applications.

The most widely used and most familiar vegetation index is the Normalized Difference Vegetation Index (NDVI) developed by Rouse et al. (1974), which is based on contrasts between maximum absorption in the red spectral region, because of chlorophyll pigments, and maximum reflection in the infrared region, caused by the cell structure of leaves and reflection of the cover due to its structure. Despite its intensive application, in cases of dense covers or those consisting of several layers the NDVI becomes saturated, such that a non-linear relationship with biophysical parameters such as the Leaf Area Index (LAI) (Baret and Guyot, 1991) is seen. The next generation of vegetation indices were developed taking into account the linearity of the cover fraction and the leaf area index, but normalizing soil brightness and color (Gilabert et al., 2011). As implied by their name, these indices refer to the soil and include the Soil Adjusted Vegetation Index (SAVI) (Huete, 1988) and the Modificied Soil Adjusted Vegetation Index (MSAVI) (Qi et al., 1994).

Other indices have been designed taking into account the spectral behavior of the soil in study areas, maintaining the sensitivity to biophysical magnitudes such as the Generalized Soil Adjusted Vegetation Index (GESAVI) (Gilabert et al., 2002). GESAVI showed good results for its linearity with LAI and soil noise reduction, simulating reflectances with radiative transfer models and with experimental data. A study by Broge and Leblanc (2001) addressing radiative transfer models has shown that the MSAVI is the best LAI estimator in terms of sensitivity-to-cover effects, variations in the cover parameters and the spectral properties of the soil. In the present work, the above vegetation indices were calculated in order to show the potential of multispectral calibrated images in agronomy.

Many studies have been carried out using multispectral and hyperspectral aerial and satellite images in the evaluation of crops (Herwitz et al., 2004; Chen et al., 2006; Zarco-Tejada et al., 2004). In fact, some authors have published works that, using multispectral, thermal or other conventional cameras on board small aircraft or unmanned helicopters, demonstrate the viability of these as platforms for image acquisition for plant studies (Esposito et al., 2007; Xiang and Tian, 2007; Turner et al., 2011; Zhao and Peng, 2006). However, to date there are no studies in which low-cost manned platforms such as PPG trikes have been used for crop monitoring. These offer an ideal platform for the study of large extensions of crops due to the above requirements.

The purpose of this article is to evaluate a new methodology aimed at acquiring georeferenced multispectral data of high spatial resolution after a radiometric calibration of the multispectral sensor for the monitoring of crops and the detection of areas with pathologies or hydric and nutritional deficiencies. To validate the methodology, a cultivated area of 5.4 ha was studied via aerial-trike overflights at different heights, using open-source software and tools. Thus, for vicarious calibration a GNU Octave (GNU, 2013) code was implemented.

The article is structured as follows: after the Introduction, Section 2 defines the method of vicarious radiometric calibration. In Section 3, the instruments used and the method developed are described. The experimental results and their discussion are given in Section 4, and the most significant conclusions are outlined in Section 5.

2. Vicarious radiometric calibration

The analysis of data captured by multispectral cameras requires prior knowledge of the radiometric calibration parameters of each channel to obtain correct interpretations. The calibration method chosen here was vicarious calibration (Dinguirard and Slater, 1999; Hernández-López et al., 2012), which involves performing an absolute radiometric calibration under flight conditions in an *in situ* radiometric measurement campaign. In this mode, the absolute method based on radiances was chosen because the digital level (DN) that defines each pixel is directly related to the radiance detected by the sensor (Hiscocks, 2011). The method based on radiances is theoretically more accurate than those based on reflectance, because it has an uncertainty of approximately only 2.8% as compared with 4.9% for the latter case (Biggar et al., 1994). This lower value is derived from the calibration and stability of the spectroradiometer required for calibration.

To carry out the radiometric adjustment, low-cost surfaces compared to other more expensive lambertian ones, have been selected as the ground control targets (invariant targets) to approximate comparable and homogenous spectral behavior under nadir observation angles to flight measurements (Davranche et al., 2009). In addition, via various laboratory tests and field studies the invariant reflective capacity for a period of time in which these surfaces were not damaged was confirmed. From the multispectral aerial images, the digital levels of these targets can be extracted and the radiance measured is obtained with the spectroradiometer on the ground, establishing a linear model for each spectral band of the sensor. To assess the effects of the atmosphere in terms of radiative transfer, the 6S Model (Vermote et al., 1997) was implemented, which transforms the radiance measured at the ground into that obtained at the height of the sensor. Finally, the results were validated with natural and artificial check targets (pseudo-invariant targets), contrasting the radiances calculated by the calibration parameters with those measured directly in the field.

Fig. 1 shows the workflow followed in the radiometric calibration process.

3. Materials and methods

3.1. Materials

The following equipment was employed for data acquisition:

- A GNSS device, Leica 1200. This consists of a RTK dual frequency receiver and geodetic GPS L2C and double dual-frequency antenna with L2C and serves to georeference control and check targets.
- A six-channel multispectral camera: Tetracam Mini-MCA. Each of the six channels of the camera is constituted by a CMOS (Complementary Metal–Oxide–Semiconductor) sensor and a filter with a preset performance against the spectral range. The spectral response of CMOS sensors is not uniform due to quantum efficiency and sensitivity. Neither do filters exhibit homogeneous transmission between each other. The effect of the combination of CMOS and the six filters results in a reduction in camera radiance, different per each wavelength. The camera specifications are defined in Table 1. The choice of the filter wavelengths (detailed in Table 2) was optimized for the evaluation of the particular behavior of the vegetation, avoiding areas of atmospheric absorption.
- A manned aerial platform supported by a powered paraglider (PPG) trike built by Airges. Its technical specifications are shown in Table 3. The Mini-MCA camera was loaded onto the PPG trike using an auto-stabilized mounting platform.

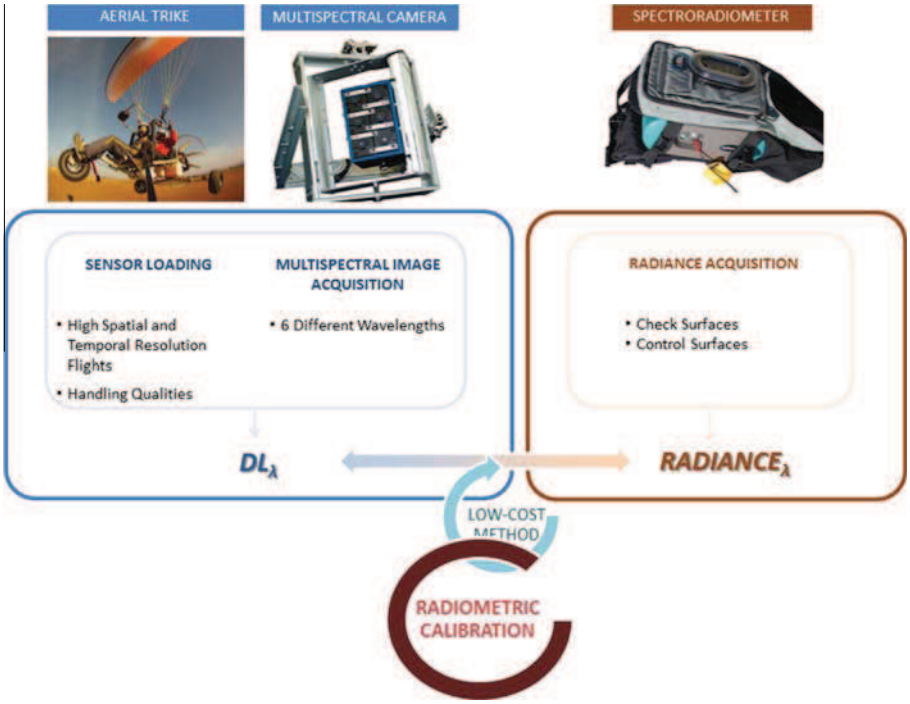

Fig. 1. Workflow of the vicarious radiometric calibration process.

Table 1
Technical specifications of the Mini-MCA multispectral camera.

Parameter	Value
Number of channels	6
Weight	700 g
Resolution	1.3 Mp per Channel
Image size	1280 × 1024 pixels
Radiometric resolution	8 bits
Capture speed	1.3 frames/s
Pixel size	5.2 μm
Focal length	9.6 mm

Table 2
Channel specifications of the Mini-MCA camera.

Channel	λmin (nm)	λmax (nm)	Exposure time (%)
0	740	820	100
1	510	550	130
2	650	690	125
3	660	740	100
4	720	760	100
5	760	840	100

Table 3
Technical specifications of the manned aerial platform, PPG trike.

Parameter	Value
Empty weight	110 kg
Maximum load	220 kg
Autonomy	3.5 h
Maximum speed	60 km/h
Motor	Rotax 503
Tandem paraglide	MACPARA Pasha 4
Emergency system	Ballistic parachutes GRS 350
Gimbal	Stabilized with 2 degrees of freedom
Minimum sink rate	1.1
Maximum glide	8.6
Plant surface	42.23 m^2
Projected area	37.8 m^2
Wingspan	15.03 m
Plant elongation	5.35
Central string	3.51 m
Boxes	54
Zoom factor	100%

- An aluminum multi-sensor gimbal (stabilized platform) where the multispectral camera is affixed. In particular, the gimbal includes two servomotors arranged on the *x* and *y* axes to maintain the vertical position of the camera along the flight path with precision. The servomotors are controlled by an Arduino board, which incorporates an IMU with 6 degrees of freedom: 3 accelerometers with a range of ±3.6 G m s^{-2}, a double-shaft gyroscope (for pitch and roll) and an additional gyroscope for yaw (both gyroscopes have a measurement range of ±300°/s). The software developed for the control of the device was based on Quadl_mini V 20 software, with DCM (Direction Cosine Matrix) as the management algorithm of the IMU (Premerlani and Bizard, 2013).
- A low-cost GNSS system based on a single-frequency receptor, with a signal reception of GPS constellation and SBAS (Satellite Based Augmentation System) (NavCen, 2008). The GNSS antenna is installed on the camera platform close to the optical center of the camera to minimize the baseline. In order to contrast the GNSS altitudinal accuracy that affects the final GSD, a DigiFly VL100 barometer was installed. Thus, horizontal positioning during flight was performed by the NMEA (National Marine Electronics Association) protocol of the GNSS system using RTKNAVI software (Takasu, 2009), with corrections from the ground from another similar board equipment, allowing DGPS accuracies better than 1.5 m in planimetry and 2 m in altimetry to be achieved in real time, and better than 0.5 m in 3 dimensions in postprocessing.
- A general purpose FieldSpec 3 ASD (Analytical Spectral Devices) spectroradiometer, used for the different targets (control and check) and specifically designed to acquire spectral measurements (radiance and irradiance) in the visible and near infrared ranges. The main technical specifications of the spectroradiometer are shown in Table 4.

Table 4
Technical specifications of the FieldSpec 3 ADS Spectroradiometer.

Parameter	Value
Spectral range	350–2500 nm
Shooting time	0.1 s
Spectral resolution	1 nm
Field of view	25°

3.2. Methods

3.2.1. Flight planning and execution

The study area was located in an experimental field of the ITAP (Provincial Agricultural Technical Institute) near Albacete (Castilla La Mancha, Spain), about 21 km from the capital. Data collection was performed on the 20th of June 2013 around a vineyard, grass and a *Papaver somniferum* crop of 5.4 ha.

Proper flight planning is important to ensure that the data captured will fit the theoretical parameters pursued; it also optimizes available resources and ensures a higher quality image, minimizing capture time.

First, the study area and subsequently the plot flight paths were defined. Then, the flight planning process defined the position and orientation of the camera, the design of different blocks of images, determination of the overlaps between different images, the necessary shot angles and guarantee of the scale through choice of the pixel size on the ground (GSD). A GSD of 0.08 m and 0.15 m was selected in this study.

The geomatic information required for the flight planning process can be obtained freely from the National Center of Geographic Information in Spain (CNIG), from its National Aerial Orthoimage Plan (PNOA, 2009) with a GSD of 0.25 m and a Digital Terrain Model (DTM) with a 5-m grid resolution.

Flight planning was performed by considering the relationship between flight altitude over the ground (H), the GSD, the focal length of the sensor (f) and pixel size, as described in Eq. (1).

$$\frac{f}{H} = \frac{pixel\,size}{GSD} \quad (1)$$

Considering Eq. (1), the characteristics of the camera (Table 1) and the required GSD of 0.08 m and 0.15 m, flight altitudes over the ground of 145 m and 245 m are obtained respectively. Also, additional restrictions, such as a minimum forward overlap of 60% and a minimum side overlap of 20% were established. The flight planning obtained is outlined in Fig. 2, where rectangles are the areas capture by each image shot in the point position.

3.2.2. Field data acquisition

In the study area, control and check targets were selected and positioned (Fig. 3) taking the GSD dimension into account.

The control and check targets used in the data collection are specified for both flights in Table 5.

In the radiometric campaign, calibration targets were characterized by the spectroradiometer as radiant flux detector. During data acquisition, the angle between the gun of the spectroradiometer and the targets measured was kept as orthogonal as possible, taking two measurements with an average of 30 spectral measurements per cover. In order to avoid the BRDF effects, the tarps have been characterized at field with enough number of samples to reject spectral reflectance anomalies.

Figs. 4 and 5 show the spectral signatures of the colored and grayscale tarps acquired in the radiometric campaign. The reflectance of these targets was obtained as the ratio of the reflected radiance of each cover and the irradiance provided by a reference target (Spectralon® 99%), both measured with the spectroradiometer.

At the same time, and in order to avoid significant atmospheric variations, a planned PPG trike flight was conducted over the study area with a 0.08 m GSD (at 145 m height) and 0.15 m GSD (at 245 m height), capturing multispectral images (Fig. 6) and finally choosing those in which the maximum number of control and check targets appeared.

3.3. Calibration methodology and fitting model

Measured radiance serves as ground truth, establishing a connection with the digital level of the corresponding wavelength. On one hand, radiance was measured in a spectral range of 350–2500 nm with a nanometer resolution. On the other, the Mini-MCA recorded digital levels in its 6 channels, characterized by the response of the filters and CMOS per wavelength. Thus, the radiometric measurements were resampled and standardized for the spectral resolution of the camera.

In addition, digital levels were corrected for vignetting and the systematic background noise produced by each lens (Kelcey and Lucieer, 2012). The vignetting study was performed at the laboratory with uniform lighting, capturing images of a white pattern with low specular reflection (Zheng et al., 2009). The systematic background noise was evaluated at the laboratory under the absence of lighting conditions and analyzing the average response of the camera per channel for its different exposure times.

Because there are several images involved in calibration adjustment, a homogenization factor of luminance between images was taken into account to neutralize the exposure differences. These differences are caused by changes in lighting between different image captures and the exposure time of each channel, according

Fig. 2. Flight planning of 0.15 m GSD (at 245 m height) (a) and 0.08 m GSD (at 145 m height) (b).

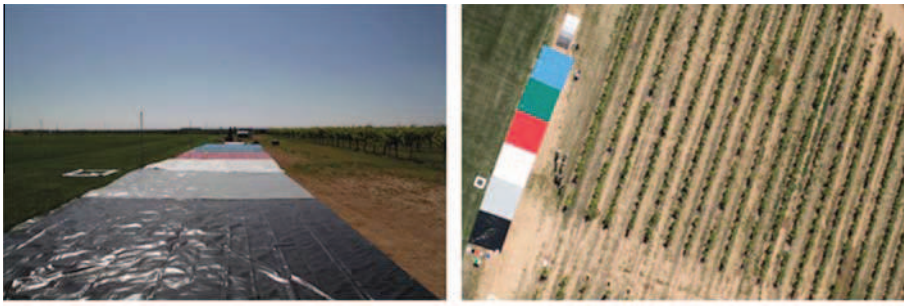

Fig. 3. Terrestrial image of the control targets for the radiometric calibration (a) aerial image of the calibration targets and study area (b).

Table 5
Description of the control and check PCV targets.

Control	Type	Material	Size	Color
Control targets	Artificial	PVC tarp	5 m × 1 m	Grayscale (5 steps)
		PVC tarp	5 m × 1 m	Black Gray White Red Green Blue
Check targets	Artificial	PVC surface	0.55 m × 0.35 m	Black Gray White Red Green Blue
		Brown wrapping paper Cork Cardboard Grass Ground		
	Natural	Grapevine *Papaver somniferum*		

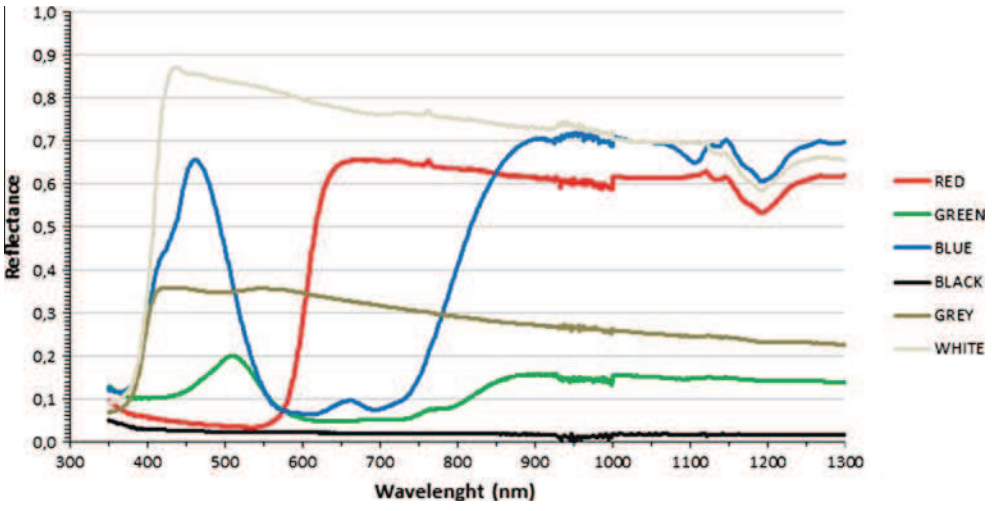

Fig. 4. Spectral signature from 350 nm to 1300 nm of the control targets (PVC tarps) obtained in the field with the spectroradiometer.

to the manufacturer. This factor corrects digital levels and depends on the channel and the image. Also, a common unknown per image and invariant for each channel was included in order to absorb possible discrepancies between the standard and real atmosphere for each image.

The mathematical model used is shown in the following figure (Fig. 7), where $\boldsymbol{X}$ is the vector of calibration coefficients (unknowns); $\mathbf{A}$ is the design matrix (corrected digital levels of control targets in the images) and $\boldsymbol{L}$ is the vector of independent terms (radiance measures of control targets).

Eq. (2) summarizes this model:

$$L = F_0 + F_1 \cdot DN_c, \tag{2}$$

where

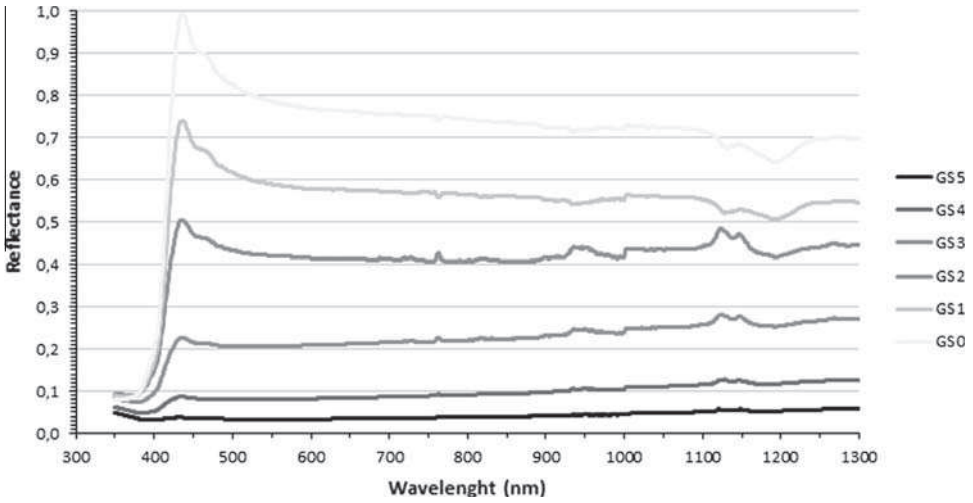

Fig. 5. Spectral signature from 350 nm to 1300 nm of the control targets (Grayscale tarp) obtained in the field with the spectroradiometer.

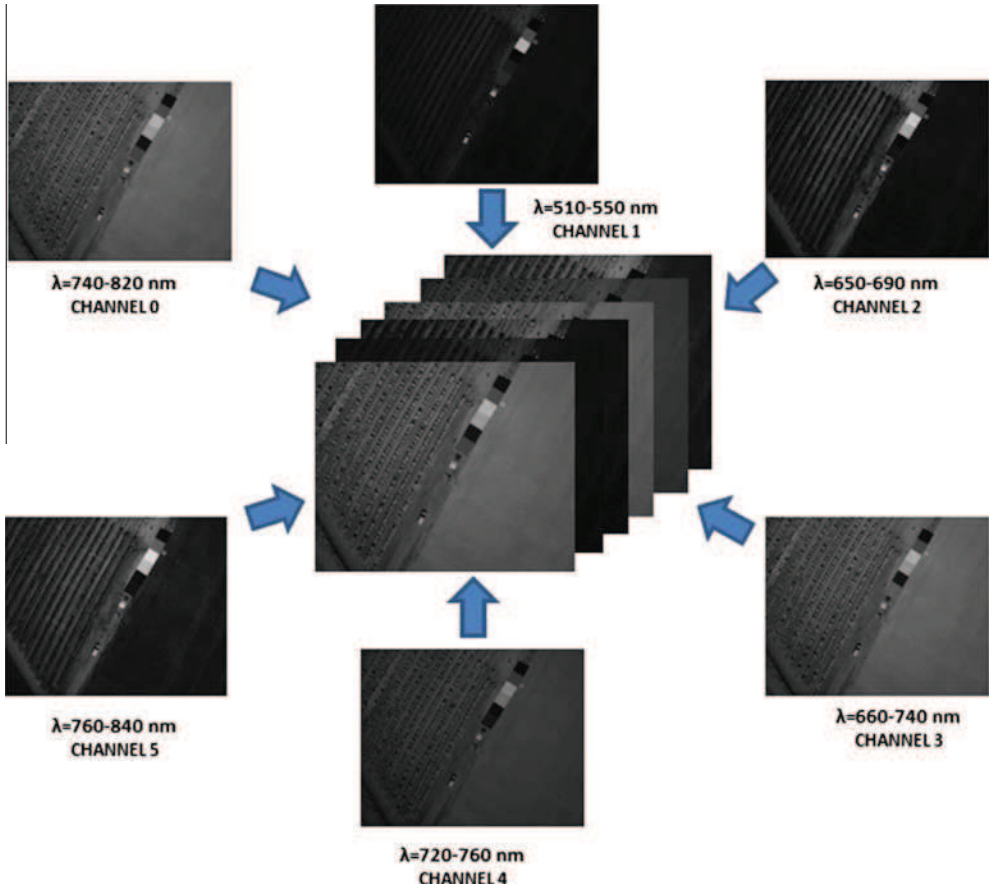

Fig. 6. Multispectral images used in the radiometric calibration process.

L is the measured radiance of each control target,
DN_c is the digital level of control targets corrected by luminance, vignetting and the systematic background noise,
F_0 is the offset calibration coefficient of each channel,
F_1 is the gain calibration coefficient of each channel.

The unknowns are obtained by solving the over-determined system without rank default, performing a robust estimation with the Danish Method (Krarup et al., 1980), which rejects the out-of-range observations (outliers), giving a series of weights based on the residual values obtained in the previous iteration.

3.4. Atmospheric correction

In aerial radiometry, the aim is to determine physical values at ground level. In this way, an atmospheric model must be applied to study the behavior of radiance propagation because of scattering and absorption processes (Hernández-López et al., 2011). In this study case, the 6S radiative transfer model (Vermote et al., 1997) was applied for the less favorable flight (0.15 m GSD flight at 245 m height).

With regard to atmospheric parameters, the values of aerosol optical depth (AOD) were taken from AERONET (aerosol robotic

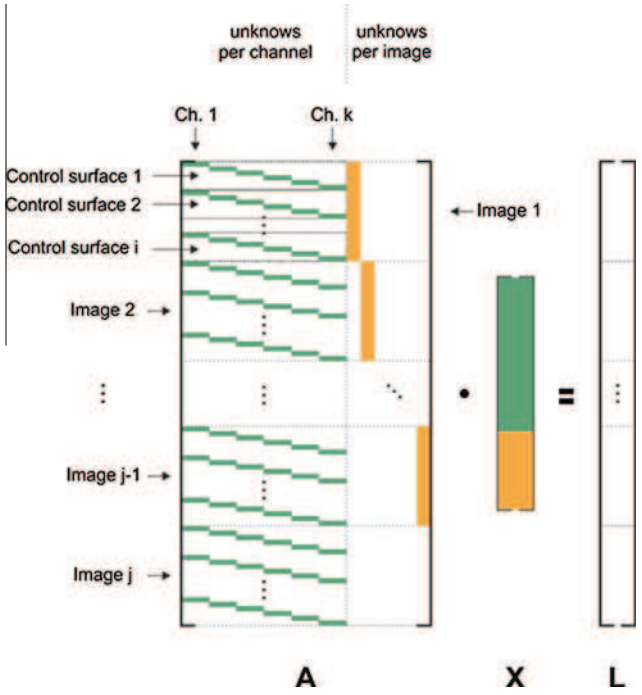

Fig. 7. Mathematical model of the radiometric calibration process.

network). Owing to the absence of closer stations, the AOD value was extracted as the average of the values of two closest stations, approximately 200 km from Albacete in the North-West and South-East directions (Madrid and Burjassot, respectively).

For each control target, sun direction was obtained at the moment of image acquisition, expressed by the geodetic azimuth and the zenith angle from the vertical. For this calculation, the Solar Position Algorithm (SPA) library (Reda and Andreas, 2004) was used. The input parameters were obtained from known flight data and GNSS measurements. Once solar direction had been calculated, the atmospheric parameters were obtained from the 6S Model, which creates an atmospheric profile on the control targets involved in the calibration process for each of the channels. Among the atmospheric parameters calculated, irradiance per image and channel and radiance and reflectance at ground and sensor per target and channel were included.

According to the data obtained, the relative influence of the atmosphere is minimal because the atmospheric column spanned by the radiation is unimportant and can be neglected in the calculations, demonstrating that sensor radiances at 1 m or 245 m height (using 6S model (Vermote et al., 1997)) were fairly similar to those measured at ground level with the spectroradiometer.

3.5. Derived geomatic products

Geomatic products are characterized by their spatial, spectral, radiometric and temporal resolution (Aber et al., 2010). In the present case, spatial resolution was limited by a GSD of 0.15 m, considered sufficient for this type of agricultural study. Temporal resolution was established considering the phenological aspects of the crop and environmental aspects. Regarding spectral resolution, this is limited to the band width of the six filters chosen to detect certain types of plant behavior in the most appropriate spectrum, avoiding areas of atmospheric absorption.

Advances in computer vision, photogrammetry and new low-cost GNSS and IMU systems make it possible to obtain orthoimages generated from images captured with a non-metric digital camera aboard a low-cost aerial platform (Aber et al., 2010).

Finally, images were georeferenced considering Coordinate Reference System (CRS) ETRS89 UTM 30 (EPSG code 25830), which is required by Spanish legislation in all geomatic products. In the navigation phase, which uses a GNNS, WGS84 CRS was employed (EPSG code 4326).

4. Experimental results and discussion

Below, the calibration parameters of the Mini-MCA camera are reported. F_0 is the offset coefficient and F_1 is the gain coefficient (Tables 6 and 7) obtained for each of the six channels achieved in the mathematical fitting of the two flights with different GSD. The *a posteriori* variance in unit weight shows a value of 0.0043 W m^{-2} sr^{-1} and a correlation coefficient of adjustment, R^2, of 0.9940.

In both flights, the detection of outliers was studied in order to avoid outliers. Standardized errors were calculated with the Pope Statistical Test (Pope, 1976), the maximum standardized residual of 2.800 remaining under the threshold of 3.916 established at the 95% of confidence level with a Tau distribution.

Together with the detection of outliers, internal fiability was tested by means of redundancy number analysis. As a result, all the equations contribute to approximately the same extent, without there being an increased presence of certain observations, due to the internal design of the proposed system, confirming the absence of outliers in the observations. The redundancy numbers of the adjustment entail a range between 0.9306 and 0.9995 for both flights.

A statistical analysis of the resulting coefficients for both flights was performed in order to assess their differences. The statistical parameter was defined as:

$$Z = \frac{\mu_1 - \mu_2}{\sqrt{\sigma_{\mu_1}^2 + \sigma_{\mu_2}^2}} \tag{3}$$

where $\sigma_{\mu 1}$ is the standard error of the mean value calculated as:

$$\sigma_{\mu_1} = \frac{\sigma}{\sqrt{n}} \tag{4}$$

The critical value for a two-tailed test at 5% of significance is ±1.96 using a normal distribution. According to the results shown in Table 8, the resulting coefficients of both flights show no significant differences, so the null hypothesis of both samples belonging to the same distribution can be accepted.

Table 6
Radiometric calibration coefficients of the multispectral camera for 0.08 m GSD flight (at 145 m height) in radiance units (W m^{-2} sr^{-1}).

Channel	F_0 value	F_1 value
0	−60.5584	2627.3057
1	19.2122	4002.9353
2	2.7057	3108.6876
3	−13.0825	2590.2099
4	−84.4579	4349.9835
5	−60.9567	2660.1684

Table 7
Radiometric calibration coefficients of the multispectral camera for 0.15 m GSD flight (at 245 m height) in radiance units (W m^{-2} sr^{-1}).

Channel	F_0 value	F_1 value
0	−77.1444	2548.2911
1	15.6807	3798.3712
2	−16.4305	2930.0517
3	−20.3672	2428.5566
4	−89.7453	4250.6229
5	−67.3736	2947.6022

Table 8
Statistical comparison of the radiometric calibration coefficients of both flights.

Channel	F_0		F_1	
	Z score	P value	Z score	P value
0	0.0143	0.9886	0.0399	0.9682
1	0.0033	0.9974	0.0979	0.9220
2	0.0167	0.9866	0.0922	0.9265
3	0.0066	0.9948	0.0886	0.9294
4	0.0046	0.9963	0.0406	0.9676
5	0.0055	0.9956	−0.1341	0.8933

To address statistical significance, two complementary hypotheses were established. In this case, H_0 establishes that residual values are distributed according to a normal distribution with mean zero, whereas H_a considers that the distribution mean is a nonzero value. The F_0 and F_1 parameters were studied in both flights, obtaining p-values greater than 0.279 and less than 0.001 respectively. Working with a 95% confidence interval, the F_0 coefficient may be negligible but not the F_1 coefficient. This is in agreement with the specifications of the manufacturer in that the offset parameter is negligible. To validate the results, the mean of the absolute values of the residuals per channel of the targets (control and check targets) between the measured and calculated radiance was used. This parameter was always below 0.01 W m^{-2} sr^{-1} (Table 9).

Because the residuals in the 0.08 m GSD flight were lower than in the 0.15 m GSD flight, the parameters at 0.08 m GSD flight were analyzed in order to be used in future studies. Fig. 8 shows a representation of the mean radiance errors of the different control targets per channel used in the calibration process.

Table 9
Mean of the absolute values of the residuals per channel in W cm^{-2} sr^{-1}.

Flight GSD(m)/height(m)	Ch. 0	Ch. 1	Ch. 2	Ch. 3	Ch. 4	Ch. 5
0.08/145	36.22	43.71	42.77	35.82	37.32	31.46
0.15/245	45.32	66.29	53.46	52.07	47.41	54.88

A statistical study was conducted to check the calibration process Table 10 shows the statistical parameters of errors (Eq. (5)) calculated as differences between ground radiance measurement with the spectroradiometer on check targets and radiance calculated by digital levels and the parameters resulting from the calibration process (Eq. (6)).

$$v = L_{measured} - L_{calculated} \tag{5}$$

$$L_{calculated} = F_0 + F_1 \cdot DNc \tag{6}$$

where

v: check target error,
$L_{measured}$: check target measured radiance,
$L_{calculated}$: check target calculated radiance,
DN_c: digital level corrected by variations in exposure time between channels, vignetting and systematic background noise,
F_0: offset calibration coefficient from each camera channel,
F_1: gain calibration coefficient from each camera channel.

The standard deviation (σ) (Eq. (7)), root mean square error ($rmse$) (Eq. (8)) and average error $|\vec{v}|$ in absolute values (Eq. (9)) are shown in Table 10, and are defined as follow:

$$\sigma = \sqrt{\frac{1}{n-1}\sum_{i=1}^{n}(v_i - \bar{v})^2} \tag{7}$$

$$rmse = \sqrt{\frac{1}{n}\sum_{i=1}^{n}(v_i)^2} \tag{8}$$

$$|\vec{v}| = \frac{\sum_{i=1}^{n}|v_i|}{n} \tag{9}$$

This shows that most of the check targets, assumed to be pseudo-invariant targets, are suitable for the validation of radiometric calibration. In general, artificially colored uniform surfaces, such as PVC targets, provided the best precision in the six channels

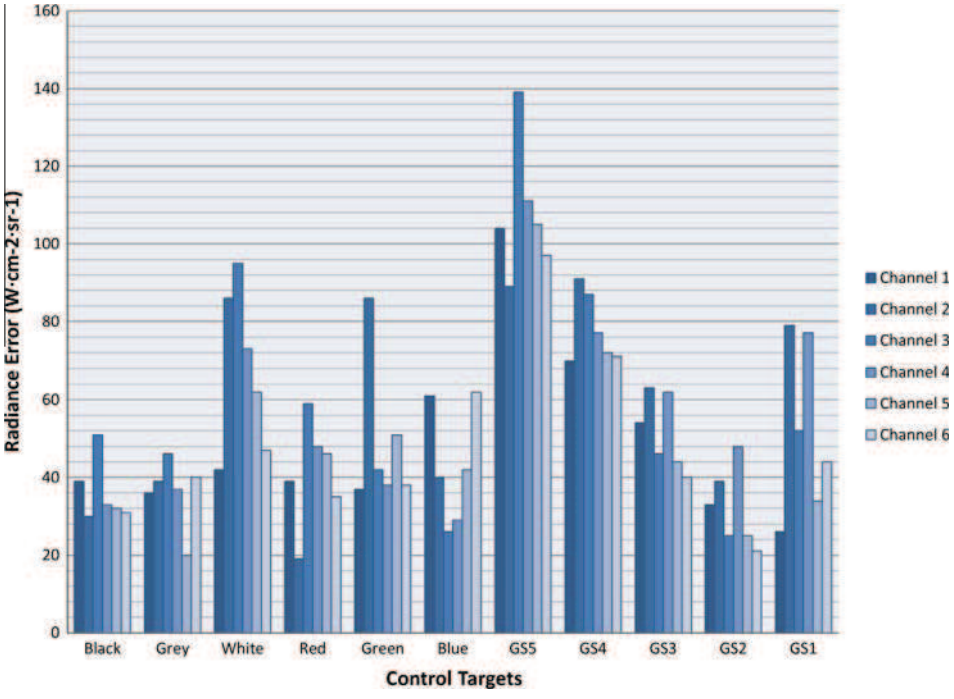

Fig. 8. Mean of the radiance errors of the different control targets (W m^{-2} sr^{-1}) per channel.

Table 10
Statistical values of errors in the vicarious calibration performed on different check targets expressed in radiances (W m^{-2} sr^{-1}), where σ is the standard deviation, *rmse* is the root mean square error, and $|\bar{v}|$ is the average absolute error value.

Target	Statistical parameter	Channel 0	Channel 1	Channel 2	Channel 3	Channel 4	Channel 5
Blue PVC	σ	61.33	54.88	17.00	33.03	44.62	63.75
	rmse	68.49	47.77	86.02	140.20	74.55	55.22
	$\|\bar{v}\|$	43.25	43.25	84.75	137.25	63.75	45.00
Gray PVC	σ	181.10	80.38	87.59	68.52	93.27	42.43
	rmse	158.47	417.84	272.76	140.18	104.63	37.41
	$\|\bar{v}\|$	124.25	412.00	262.00	127.00	103.00	33.00
Green PVC	σ	49.11	59.61	80.64	46.12	68.77	43.07
	rmse	151.11	189.90	137.55	140.78	151.22	177.71
	$\|\bar{v}\|$	145.00	182.75	118.50	135.00	139.00	173.75
Red PVC	σ	146.71	20.94	144.03	112.53	198.00	111.80
	rmse	270.67	42.56	588.37	352.01	350.12	225.13
	$\|\bar{v}\|$	239.00	38.50	575.00	338.25	305.25	203.25
Black PVC	σ	15.41	37.10	18.63	41.84	38.20	28.52
	rmse	167.51	222.40	211.18	186.09	180.31	157.67
	$\|\bar{v}\|$	167.50	222.38	211.18	186.05	180.28	157.65
White PVC	σ	214.36	133.39	195.42	209.22	230.73	167.65
	rmse	560.86	1492.48	1063.80	666.12	590.34	491.68
	$\|\bar{v}\|$	529.25	1488.00	1050.25	641.00	555.50	469.75
Ground	σ	9.90	11.31	7.07	24.75	28.99	12.02
	rmse	99.25	149.21	287.04	95.12	113.37	42.36
	$\|\bar{v}\|$	99.00	149.00	287.00	93.50	111.50	41.50
Brown Wrapping Paper	σ	58.94	84.68	81.93	103.23	111.70	101.10
	rmse	51.27	73.98	153.66	94.62	96.43	89.79
	$\|\bar{v}\|$	47.67	63.00	138.33	80.33	87.33	86.67
Cardboard	σ	57.14	52.00	73.60	138.30	88.06	93.22
	rmse	436.17	591.19	731.14	466.21	421.84	351.67
	$\|\bar{v}\|$	−433.67	−589.67	−728.67	−452.33	−415.67	−343.33
Grass	σ	141.20	69.85	48.06	54.24	100.34	112.49
	rmse	129.85	102.45	58.18	63.52	90.71	112.71
	$\|\bar{v}\|$	127.40	81.20	42.40	44.20	75.60	106.80
Grapevine	σ	–	–	–	–	–	–
	rmse	169.00	59.00	42.00	22.00	294.00	128.00
	$\|\bar{v}\|$	169.00	59.00	42.00	22.00	294.00	128.00
Cork	σ	14.14	26.16	72.12	65.05	91.22	29.70
	rmse	417.12	330.02	629.07	473.24	416.52	384.57
	$\|\bar{v}\|$	417.00	329.50	627.00	471.00	411.50	384.00
P. somniferum.	σ	–	–	–	–	–	–
	rmse	469.00	185.00	355.00	225.00	334.00	345.00
	$\|\bar{v}\|$	469.00	185.00	355.00	225.00	334.00	345.00

of the spectrum, while more heterogeneous surfaces such as the ground or vegetation afforded poorer results. These are anisotropic and less homogeneous surfaces than PVC, with higher variations in the radiance leaving the target and its reflectance. This produces a slight increase in its *rmse* and σ.

All these results confirm the feasibility of using tarps of different colors as a low-cost alternative to spectralon with certain limitations for vicarious radiometric calibration. As a result, several measurements can be obtained by increasing the number of targets and hence improving the quality of the mathematical fitting.

Although not aiming to investigate the performance of the different vegetation indices, an example of the product generated using the georeferenced multispectral reflectance images is provided in this work in order to highlight its potential in agricultural studies. Four multispectral vegetation indices were selected taking into account that they are widely applied in agronomy owing to their sensitivity to vegetation and their normalization of soil background brightness and color: NDVI, SAVI, MSAVI and GESAVI. The latter was parameterized for the soil characteristics in the study area.

These images were processed with algorithms defined in the 2nd and 5th channel of the multispectral sensor (670 and 800 nm) (Fig. 8) through an implemented code in GNU Octave software.

The reflectance of each pixel was obtained from the calculated radiance and irradiance per channel acquired previously with a calibrated PVC target that appeared on the image, according to Eq. (10) for each sensor channel [24], under the assumption of a Lambertian surface.

$$\rho = \frac{L_{calculated} \cdot \pi}{E} \tag{10}$$

where $L_{calculated}$ is the radiance calculated from each target and E is the irradiance per channel.

Although the indices addressed here do not have the same range of variation, all of them identify the plant trellis in the scene, as can be seen in Fig. 9. They enhance the photosynthetic activity in the scene, showing not only the presence of the vineyard plants but also other small plants between the rows. The darkest areas correspond to non-vegetated areas. These images can also be compared quantitatively to other flight dates allowing the vineyard to be monitored for the managing of nutrients, diseases or water supply within the plot.

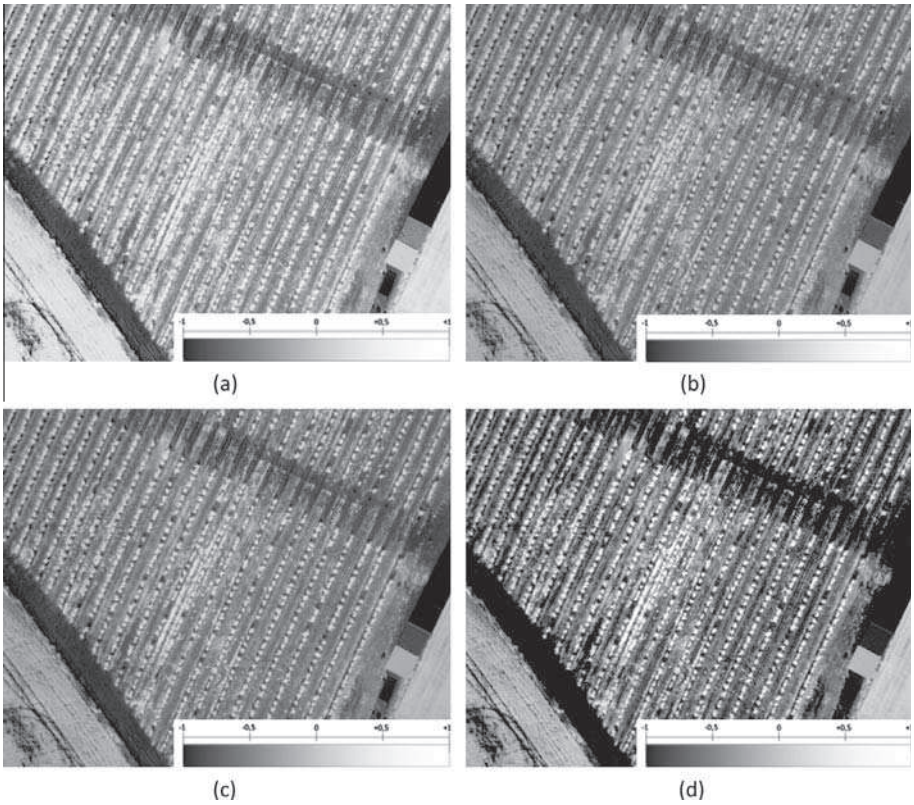

Fig. 9. Different plant indices in the vineyard area derived from the radiometric calibration: (a) NDVI Image, (b) SAVI Image, (c) MSAVI Image and (d) GESAVI Image.

5. Conclusions

This paper describes a successful methodology for radiometric calibration using the vicarious method of a multispectral Mini-MCA camera aboard a low-cost manned aerial platform and using low-cost targets of invariant reflectivity material. The statical analysis of the errors confirms the validity of the method. For this purpose, a flight at two different heights was carried out to test adjustment stability, the calibration coefficients being statistically consistent in both cases, demonstrating insignificant relative atmospheric effects occurring in flights below 300 m on a clear and sunny day. In fact, this is the maximum height at which these platforms are permitted to fly according to Spanish legal constraints. The results confirm a new trend for low-cost remote sensing, together with the use of the latest computer vision techniques and open-source geomatic tools. In this study case, the calibrated geomatic products can be used to successfully evaluate and classify large areas of different crops, allowing decisions to be made about irrigation, nutritional support and crop development through accurate georeferenced and calibrated multispectral images. Compared to classic aerial photogrammetric platforms (aircraft), the proposed methodology cuts costs. Regarding satellite systems, their temporal and spatial resolution generates a major limitation in applications to crops. The potential of this PPG trike system is evident, with the possibility of being able to load it with a large number of sensors that extend multispectral studies, affording the advantage of a flying height that minimizes the need for atmospheric corrections. Here, the potential of deriving quantitative magnitudes such as vegetation indices is also shown. Future works will address the assimilation of the calibrated images into agronomic models to evaluate their consistency with advanced biophysical variables.

References

Aber, J.S., Marzolff, I., Ries, J., 2010. Small-Format Aerial Photography: Principles, Techniques and Geoscience Applications. Elsevier Science, The Netherlands.
Baret, F., Guyot, G., 1991. Potentials and limits of vegetation indices for LAI and APAR assessment. Remote Sens. Environ. 35, 161–173.
Berni, J., Zarco-Tejada, P.J., Suarez, L., Fereres, E., 2009. Thermal and narrowband multispectral remote sensing for vegetation monitoring from an unmanned aerial vehicle. IEEE Trans. Geosci. Remote Sens. 47 (3), 722–738.
Biggar, S.F., Slater, P.N., Gellman, D.I., 1994. Uncertainties in the in-flight calibration of sensors with reference to measured ground sites in the 0.4–1.1 μm range. Remote Sens. Environ. 48 (2), 245–252.
Biggar, S.F., Thome, K.J., Wisniewski, W., 2003. Vicarious radiometric calibration of EO-1 sensors by reference to high-reflectance ground targets. Geosci. Remote Sens., IEEE Trans. 41 (6), 1174–1179.
Broge, N.H., Leblanc, E., 2001. Comparing prediction power and stability of broadband and hyperspectral vegetation indices for estimation of green leaf area index and canopy chlorophyll density. Remote Sens. Environ. 76 (2), 156–172.
Chen, X., Zhao, H., Li, P., Yin, Z., 2006. Remote sensing image-based analysis of the relationship between urban heat island and land use/cover changes. Remote Sens. Environ. 104 (2), 133–146.
Chuvieco, E., Huete, A., 2009. Fundamentals of Satellite Remote Sensing. CRC Press Inc.
Davranche, A., Lefebvre, G., Poulin, B., 2009. Radiometric normalization of SPOT-5 scenes: 6S atmospheric model versus pseudo-invariant features. Photogramm. Eng. Remote Sens. 75 (6).
Dinguirard, M., Slater, P.N., 1999. Calibration of space-multispectral imaging sensors: a review. Remote Sens. Environ. 68 (3), 194–205.
Esposito, F., Rufino, G., Moccia, A., 2007. 1st Mini-UAV Integrated Hyperspectral/Thermal Electro-Optical Payload for Forest Fire Risk Management. In: Proc. AIAA InfotechAerosp. Conf. pp. 653–665.
Gilabert, M.A., González-Piqueras, J., García-Haro, F.J., Meliá, J., 2002. A generalized soil-adjusted vegetation index. Remote Sens. Environ. 82, 303–310.
Gilabert, M.A., González-Piqueras, J., Martínez, B., 2011. Theory and application of vegetation indices. In: Maselli, F., Menentiand, M., Brivio, P.A. (Eds.), Optical Observation of Vegetation Properties and Characteristics. Research Signpost, Kerala, India, pp. 1–43.
http://www.gnu.org/software/octave (accessed 01.12.13).
Hailey, T.I., 2005. The powered parachute as an archaeological aerial reconnaissance vehicle. Archaeol. Prospection 12 (2), 69–78.

Hernández-López, D., Felipe-García, B., González-Piqueras, J., Alcázar, G.V., 2011. An approach to the radiometric aerotriangulation of photogrammetric images. ISPRS J. Photogramm. Remote Sens. 66 (6), 883–893.
Hernández-López, D., Felipe-García, B., Sánchez, N., González-Aguilera, D., Gomez-Lahoz, J., 2012. Testing the radiometric performance of digital photogrammetric images: vicarious vs. laboratory calibration on the Leica ADS40, a study in Spain. Photogramm. Fernerkundung Geoinform. 2012 (5), 557–571.
Hernandez-Lopez, D., Felipe-Garcia, B., Gonzalez-Aguilera, D., Arias-Perez, B., 2013. An automatic approach to UAV flight planning and control for photogrammetric applications: a test case in the asturias region (Spain). Photogramm. Eng. Remote Sens. 79 (1), 87–98.
Herwitz, S.R., Johnson, L.F., Dunagan, S.E., Higgins, R.G., Sullivan, D.V., Zheng, J., Lobitz, B.M., Leung, J.G., Gallmeyer, B.A., Aoyagi, M., Slye, R.E., Brass, J.A., 2004. Imaging from an unmanned aerial vehicle: agricultural surveillance and decision support. Comput. Electron. Agric. 44, 49–61.
Hiscocks, P.D., 2011. Measuring Luminance with a Digital Camera. <http://www.ee.ryerson.ca/~phiscock/astronomy/light-pollution/luminance-notes.pdf> (accessed 17. 07. 14).
Honkavaara, E., Arbiol, R., Markelin, L., Martinez, L., Cramer, M., Bovet, S., Chandelier, L., Ilves, R., Klonus, S., Marshal, P., Schläpfer, D., Tabor, M., Thom, C., Veje, N., 2009. Digital airborne photogrammetry—a new tool for quantitative remote sensing?—a state-of-the-art review on radiometric aspects of digital photogrammetric images. Remote Sens. 1 (3), 577–605.
Huete, A.R., 1988. A soil-adjusted vegetation index. Remote Sens. Environ. 25, 298–309.
Kelcey, J., Lucieer, A., 2012. Sensor correction of a 6-band multispectral imaging sensor for UAV remote sensing. Remote Sens. 4, 1462–1493.
Krarup, T., Juhl, J., Kubik, K., 1980. In: Götterdammerung Over Least Squares Adjustment, XIV Congress of International Society of Photogrammetry, Hamburg; Hamburg. pp. 369–378.
Lass, L.W., Callihan, R.H., 1997. The effect of phenological stage on detectability of yellow hawkweed (Hieraciumpratense) and oxeye daisy (Chrysanthemum leucanthemum) with remote multispectral digital imagery. Weed Technol. 11 (2), 248–256.
NavCen, 2008. Global Positioning System Standard Positioning Service Performance Standar, 4th ed. US Department of Defense: Position, Navigation, and Timing Executive Committee, Washington, DC.
Pope, A.J. 1976. The statistics of residuals and the detection of outliers. In: NOAA Technical Report NOS 65 NGS 1, National Ocean Service, National Geodetic Survey. US Department of Commerce, Rockville, MD, Washington, 133pp.
Premerlani, W., Bizard, P., 2013. Direction Cosine Matrix IMU: Theory. <http://gentlenav.googlecode.com/files/DCMDraft2.pdf> (accessed 01.12.13).
Qi, J., Chehbouni, A., Huete, A., Kerr, Y., Sorooshian, S., 1994. A modified soil adjusted vegetation index. Remote Sens. Environ. 48 (2), 119–126.
Reda, I., Andreas, A., 2004. Solar position algorithm for solar radiation applications. Sol. Energy 76 (5), 577–589.
Rouse, J.W., Haas, R.H., Schell, J.A., Deering, D.W., Harlan, J.C., 1974. Monitoring the vernal advancement of retrogradation of natural vegetation, NASA/GSFC, Type III. In: Final Report. Greenbelt, MD, p. 371.
Schmidt, K.S., Skidmore, A.K., 2003. Spectral discrimination of vegetation types in a coastal wetland. Remote Sens. Environ. 85 (1), 92–108.
Takasu, T., 2009. RTKLIB: Open Source Program Package for RTK-GPS. FOSS4G, Tokyo, Japan.
Turner, D., Lucieer, A., Watson, C., 2011. Development of an Unmanned Aerial Vehicle (UAV) for hyper resolution vineyard mapping based on visible, multispectral, and thermal imagery. In: Proceedings of 34th International Symposium on Remote Sensing of Environment. p. 4.
Vermote, E.F., Tanre, D., Deuze, J.L., Herman, M., Morcette, J.J., 1997. Second simulation of the satellite signal in the solar spectrum, 6S: an overview. IEEE Trans. Geosci. Remote Sens. 35 (3), 675–686.
Xiang, H., Tian, L., 2007. Autonomous Aerial Image Georeferencing for an UAV-Based Data Collection Platform Using Integrated Navigation System. ASABE Annual Meeting, Minneapolis, Minnesota.
Zarco-Tejada, P.J., Miller, J., Morales, A., Berjón, A., Agüera, J., 2004. Hyperspectral indices and model simulation for chlorophyll estimation in open-canopy tree crops. Remote Sens. Environ. 90 (4), 463–476.
Zhang, C., Kovacs, J., 2012. The application of small unmanned aerial systems for precision agriculture: a review. Precision Agric. 13 (6), 693–712.
Zhao, W.T., Peng, J.Y., 2006. VORONOI diagram-based path planning for UAVs. J. Syst. Simul. 18 (2), 159–162.
Zheng, Y., Lin, S., Kambhamettu, C., Jingyi, Y., Sing Bing, K., 2009. Single-image vignetting correction. IEEE Trans. Pattern Anal. Mach. Intell. 31, 2243–2256.

Computers and Electronics in Agriculture 110 (2015) 17–26

Contents lists available at ScienceDirect

Computers and Electronics in Agriculture

journal homepage: www.elsevier.com/locate/compag

Vineyard yield estimation by automatic 3D bunch modelling in field conditions

Mónica Herrero-Huerta [a,*], Diego González-Aguilera [a], Pablo Rodriguez-Gonzalvez [a], David Hernández-López [b]

[a] Department of Cartographic and Land Engineering, University of Salamanca, Higher Polytechnic School of Avila, Hornos Caleros 50, 05003 Avila, Spain
[b] Institute for Regional Development (IDR), University of Castilla La Mancha, 02071 Albacete, Spain

ARTICLE INFO

Article history:
Received 26 May 2014
Received in revised form 7 August 2014
Accepted 1 October 2014

Keywords:
Yield estimation
Photogrammetry
Computer vision
Vitis vinifera L.
Automation
Non-invasive technologies

ABSTRACT

This manuscript focuses on developing a workflow for determining the productivity of vineyards in a novel and innovative way, ensuring flexibility and simplicity in data acquisition, automation in the process and high-quality results, using low cost sensors. The non-invasive system proposed allows the determination of yield at cluster level by combining close-range photogrammetry and computer vision. Bunches are reconstructed in 3D from images processed with Photogrammetry Workbench software (PW) developed by the authors. Algorithms and techniques were combined to estimate the most relevant parameters in the productivity of a vineyard: volume, mass and number of berries per bunch. To validate the workflow proposed, a sample of laboratory tests based on dimensional analysis of the clusters together with the single count of berries, were analyzed to establish the groundtruth. The results achieved from the scaled models and different estimation parameters were contrasted. The results confirm the feasibility of the proposed methodology, providing scalability to a comprehensive analysis of the productivity of the vineyard and affording a constant operational improvement and proactive management.

1. Introduction

The development of innovative technologies in viticulture to monitor vineyards is encouraged because of their huge environmental and economic impact on society. Computer vision systems are highly suitable for this purpose because they are a non-contact and non-destructive technique (Chherawala et al., 2006). The application scenarios of digital image analysis cover yield estimation, quality evaluation, disease detection and grape phenology (Whalley and Shanmuganathan, 2013). One of the main concerns in the wine industry along history has been the accurate and objective estimation of the yield and the oenological potential of vineyards: *yield forecasting* or harvest forecasting. Currently, this is still an unresolved issue and is of great technical and economic importance (Wolpert and Vilas, 1992; Clingeleffer et al., 2001; Dunn and Martin, 2004). A precise vineyard yield estimation allows more efficient grapevines to be obtained, their qualitative potential to be established, and the production of higher-quality wines (Dunn and Martin, 2003). Roby et al. (2004) checked that berry size is a determining factor for winegrape quality where the berry small size is related to lack of water and the variation in berry size indicates an inhomogeneous maturation. Also, this estimation influences decision-making techniques, such as the execution of vineyard score sheets.

Currently, the methods applied at industrial scale to estimate the productivity of vineyards are destructive, labour- and time-demanding (Martin et al., 2003) and, therefore, economically non-viable. Furthermore, several methods are based mostly on a visual inspection of the vineyard so the final data cannot guarantee reliability and accuracy. In light of this, a specific software (Grape Forecaster) was developed (Martin et al., 2003) to calculate the final harvest, allowing only historical information on yield components and variations from year to year to be collected. Blom and Tarara (2009) proposed a method based on the tension of the wires of the conduction system, which is expensive. Grape yield assessment was studied from the point of view of water availability and its effects on yield and berry quality attributes (Serrano et al., 2012) by expensive measuring techniques. For these reasons, in recent years image analysis has begun to be applied in viticulture in attempts to assess the vegetative state or performance of vineyards in some countries such as Australia

* Corresponding author. Tel.: +34 920353500x3820.
E-mail address: monicaherrero@usal.es (M. Herrero-Huerta).

http://dx.doi.org/10.1016/j.compag.2014.10.003
0168-1699/

(Dunn and Martin, 2004) or the U.S. (Nuske et al., 2011). More concretely, Dunn and Martin (2004) captured in field images using a white screen behind the canopy and extracted the colour features to classify the berry clusters, using manual thresholds and tolerances for the segmentation. The work of Nuske et al. (2011) involves a visible light camera boarded in a small vehicle to survey the entire vineyard. The berries are detected based on a 2D radial symmetry transform to extract their center, and then are classified based on their colour and texture. Finally a clustering is applied to remove false positives. In a recent work (Nuske et al., 2012) the use of calibration data from prior harvest data enhanced the previous results. Moreover, 2D computer vision techniques have also been applied to individual strains for the identification of plant elements (Herrero Langreo et al., 2010) or counting individual berries using a flatbed scanner (Battany, 2008). A 2D grapevine yield and leaf area estimation was done by Diago et al. (2012), who used a visible light camera to capture images in-field using a white screen behind the canopy. Their approach involves the computation of Mahalanobis colour distance for a supervised classification application. Approaches to obtaining 3D models from photographs for plant analyses were carried out at a laboratory with individual tomato plants (Aguilar et al., 2008), but without effective automation and failing to translate this technology to field conditions. More recently, Djuricic et al. (2014) employed an active sensor, multi-echo laser scanner, for grape berries detection, through the laser intensity.

This paper aims to establish a method for estimating vine production in field conditions using low-cost, non-invasive methods based on computer vision (Sethian, 1999). Thus, 3D models of bunches were obtained and dimensional analyses were carried out to calculate the different yield components. The development of the proposed method had to face additional difficulties, such as the partial 3D models generated by *in-situ* bunch documentation (only the visible side of the bunch), or having to deal with the occlusions and geometrical complexities of the strain itself. Techniques and algorithms to estimate the components of vineyard yields were developed. The recovery of the non-visible side in the model was achieved using convex hull techniques (Barber et al., 1996). The main output of this workflow was an accurate and precise predictive method aimed at eliminating the subjectivity deriving from the spatial and temporal variability of grape production. This would allow vine growers to take decisions in advance.

2. Image-based modelling

For precision agriculture purposes, a combination of Photogrammetry quality and computer vision algorithms (flexibility, automation and efficiency) is required. An image-based modelling technique based on this combination allows 3D models to be obtained from 2D images via two main steps: first, the automatic determination of the view of each image taken at vineyards; second, the automatic computation of the 3D coordinates for the generation of a dense and scaled 3D model of the scene.

This is a non-destructive and non-invasive technology with low associated costs. The methodology allows data to be acquired remotely with great efficiency, affording the radiometric and geometric characteristics of objects with a high degree of accuracy and detail in complex scenarios. Moreover, photogrammetry has advantages over others sensors, such as expensive laser systems (Lumme et al., 2008) or gaming sensor technologies, which are subject to difficulties in external daylight scenarios (Lange et al., 2011) as well as having a reduced working range.

To develop the proposed method, several robust descriptors for feature extraction and matching were implemented and tested, the SIFT variation (ASIFT) being the one that provided the best results in this study, where variations in geometry and lighting were very common. Last, but not least, several camera calibration models, such as the Brown model or the Fraser model, were integrated to allow working with any type of camera, including low-cost smartphones and tablets (Akca and Gruen, 2007).

Fig. 1 schematizes the workflow of the PW software (González-Aguilera et al., 2013) based on image-based modelling.

2.1. Image acquisition protocol

The image acquisition protocol is the key to success of the developed process since these images represent the input data of the workflow, and thus their position (spatial and attitude) will affect the final accuracy (i.e. in terms of perspective ray intersection) and completeness (i.e. in terms of overlap between images) of the 3d model.

Prior to image acquisition, the scene must be analyzed, including the lighting conditions because these will influence the exposure values, and the aperture and shutter speeds of the sensor. To this end, images should be acquired without strong variations in illumination, avoiding overexposed areas and ensuring sharpness, together with an occlusion analysis due to the presence of obstacles that will affect the image acquisition protocol and the overlaps between adjacent images. The shortest available focal length of the camera should be chosen and must be held constant throughout the image acquisition process to keep the internal camera parameters stable.

Regarding the geometric conditions of the camera shots, the objective is to establish an image acquisition protocol to reconstruct the grapevine of interest, guaranteeing the completeness and best accuracy of the resulting 3D model to perform the dimensional analysis of each cluster. It should be remarked that finding an optimal image network can be complex, in particular in scenes with strong depth variations and occlusions. Therefore, the key at this point is to establish a guideline, based on simple geometric constraints, to perform image acquisition at vineyards (Fig. 2). For an extensive vineyard study, at least five images (one master and four slaves) must be taken of each grapevine. The master image should cover the study grapevine and represents the origin of the coordinate system. This image has to be taken in a frontal way and framing the principal part of the grapevine or, if possible, including all of it. The overlaps between the slaves and master image must be high (80–90%) and must always maintain a slight convergence (i.e. optical axis) (maximum 15°) so that image matching will be ensured during the orientation phase. Regarding depth, this should be chosen according to the image scale or the desired resolution. This image acquisition protocol ensures the completeness and quality of the final model.

The automatic scaling of the 3D point clouds is resolved by incorporating self-scaled algorithms based on the automatic recognition of targets of known dimension which should appear in the photograph.

2.2. Features extraction and matching

One of the most critical steps in this process is the extraction and matching of features (lines and points) with high accuracy and reliability. This constitutes the framework that supports the whole process by providing the necessary information to resolve the spatial and attitude positions of images (orientation), camera self-calibration and, finally, grapevine 3D reconstruction. In addition, agricultural scenes usually show variations in scale, perspective and illumination, so classical descriptors based on grey levels such as area-based matching (ABM) (Joglekar and Gedam, 2012) and least square matching (LSQ) (Gruen, 1985) are useless. To this end, more sophisticated and robust descriptors were tested: smallest univalue segment assimilating nucleus (SUSAN)

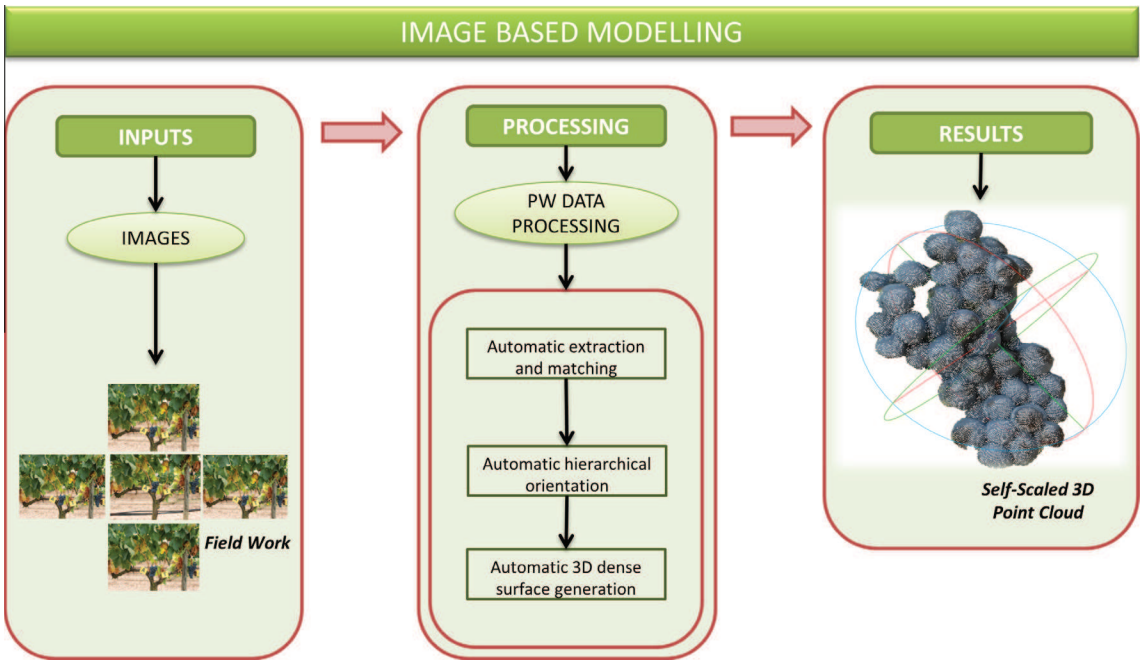

Fig. 1. Workflow of image-based modelling technique.

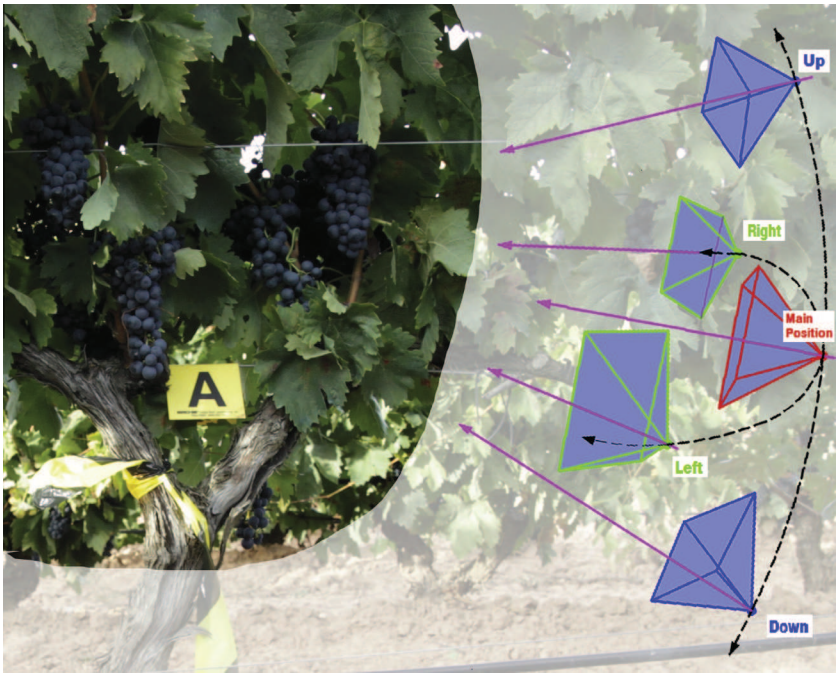

Fig. 2. Protocol of image acquisition of the study grapevines.

(Smith and Brady, 1997); scale invariant feature transform (SIFT) (Lowe, 2004); maximally stable extremal regions (MSER) (Matas et al., 2004) and speeded up robust features (SURF) (Bay et al., 2006). Unfortunately, all these algorithms become ineffective when there are considerable variations in perspective between images.

In this sense, a variation of the SIFT algorithm, called affine scale invariant feature transform (ASIFT) (Morel and Yu, 2009), has been incorporated to the PW software. It permits the consideration of two additional affinity parameters that control the perspective of the images. These are the angles corresponding to two perspective angles of the camera's optical axis, the ϖ angle (tilt) and the φ angle (axis) (Eq. (1)). In this way, the ASIFT algorithm allows one to cope with images that have a high degree of perspective, which is very common in vineyards. The result is an invariant descriptor that considers scale, rotation, movement and significant deformations due to the perspective between images. This result provides the next expression:

$$A = \begin{bmatrix} a & b \\ c & d \end{bmatrix} = H_{\lambda} R_1(\kappa) T_1 R_2(\varpi) = \lambda \begin{bmatrix} \cos\kappa & -\sin\kappa \\ \sin\kappa & \cos\kappa \end{bmatrix} \cdot \begin{bmatrix} t & 0 \\ 0 & 1 \end{bmatrix} \cdot \begin{bmatrix} \cos\varpi & -\sin\varpi \\ \sin\varpi & \cos\varpi \end{bmatrix} \quad (1)$$

where A is the affinity transformation that contains the scale (λ), rotation (κ) around the optical axis (swing) and perspective parameters corresponding to the inclination of the camera optical axis (φ (tilt)), the vertical angle between the optical axis and the line perpendicular to the image plane and the horizontal angle between the optical axis and the fixed vertical plane (ϖ(axis)).

The matching process is carried out by SIFT descriptors. These descriptors are first matched according to the Euclidean distance (Lowe, 1999), after which they are filtered by the optimized random sampling algorithm (ORSA) (Moisan and Stival, 2004; Moisan et al., 2012). This algorithm is a variant of random sample consensus (RANSAC) (Fischler and Bolles, 1981) with an adaptative criterion to filter outliers by epipolar geometry constraints.

2.3. Hierarchical image orientation

Computing the spatial and attitude position of images is not an easy mathematical task. Furthermore, image orientation is based on features related to extraction and matching, so the presence of outliers could be quite common. In this sense, the method proposes a hierarchical approach for obtaining an approximate and relative image orientation in an arbitrary coordinate system based on computer vision. It can be refined and improved in an absolute and scaled coordinate system for the set of images thanks to photogrammetry.

Firstly, a relative image orientation is achieved using independent models obtained from the fundamental matrix calculated with the Longuet–Higgins algorithm (Longuet-Higgins, 1987). One of the greatest advantages of the fundamental matrix is that it is independent of any scene, so no knowledge of the internal parameters or initial approaches of the camera is required.

Secondly, once the relative attitude and spatial position of images has been obtained, a global adjustment of all images (bundle-adjustment) is performed by an iterative and least-squares process based on the collinearity condition (Kraus, 1993). The coordinates of the ground control points are incorporated for absolute georeferencing (Eq. (2)). These ground coordinates are added to the orientation process as artificial targets located around the vineyard. In cases in which the internal calibration parameters of the camera are unknown (principal distance, principal point and lens distortion), this second step allows these parameters (self-calibration) to be incorporated into the equation as unknowns (Quan, 2010).

$$\begin{aligned}(x-x_0)+\Delta x &= -f\frac{r_{11}(X-S_X)+r_{21}(Y-S_Y)+r_{31}(Z-S_Z)}{r_{13}(X-S_X)+r_{23}(Y-S_Y)+r_{33}(Z-S_Z)}\\ (y-y_0)+\Delta y &= -f\frac{r_{12}(X-S_X)+r_{22}(Y-S_Y)+r_{32}(Z-S_Z)}{r_{13}(X-S_X)+r_{23}(Y-S_Y)+r_{33}(Z-S_Z)}\end{aligned} \quad (2)$$

where x, y are the image coordinates of a point of the scene; X, Y, Z are the coordinates of the scene point expressed in a local reference system; r_{ij} are the rotation matrix coordinates; S_X, S_Y, S_Z are the spatial coordinates of the camera point of view; f is the camera focal length; x_0, y_0 are the principal point coordinates of the image, and X, Y are the radial and tangential distortion parameters of the lens.

2.4. Automatic dense surface generation

Starting from the robust image orientation, a dense matching process was developed. It is based on the semi-global matching technique (SGM) (Hirschmuller, 2005; Deseilligny and Clery, 2011). Applying the projective equation (Hartley and Zisserman, 2003) (3), it permits the generation of a dense model resulting from the determination of a 3D coordinate per pixel.

$$x_k = \boldsymbol{C}(\boldsymbol{D}(\boldsymbol{R}_i(X_k - S_i))) \quad (3)$$

where X is the 3D point; x is the point corresponding to the image; $\boldsymbol{R}$ is the camera rotation matrix; S is the camera projection center; $\boldsymbol{C}$ is the internal calibration function; $\boldsymbol{D}$ is the lens distortion function, and the subscripts k and i are related to point and image, respectively.

The SGM process consists of minimizing an energy function (4) through the eight basic directions that a pixel can take. This function is composed of a cost function, $\boldsymbol{M}$, which reflects the degree of similarity of the pixels between two images, x and x', together with the incorporation of two restrictions, and P_1 and P_2, which show the possible presence of outliers in the SGM process.

$$E(D) = \sum_x \Big(M(x, D_x) + \sum_{x' \in N_x} P_1 T[|D_x - D_{x'}| = 1] + \sum_{x' \in N_x} P_2 T[|D_x - D_{x'}| > 1]\Big) \quad (4)$$

where $E(D)$ is the energy function to be minimized on the basis of the disparity between the homologous characteristics; the function C evaluates the level of similarity between the pixel p and its counterpart q through the disparity Dp, while the P_1 and P_2 terms correspond to two restrictions to avoid outliers in the dense matching process due to the disparity of one pixel or a higher number of them, respectively.

In addition, a third constraint was added to the SGM process. This consisted of epipolar geometry derived from photogrammetry (Hartley and Zisserman, 2003) and can enclose the search space per pixel in order to reduce the huge computational cost. In particular, based on the computed fundamental matrix, $\boldsymbol{F}$, the following search band is defined: $\boldsymbol{l}' = x\boldsymbol{F}$, which establishes that the corresponding point of x should be along the epipolar line $\boldsymbol{l}'$. In other words if two image points (x and x') correspond, then the epipolar line $\boldsymbol{l}'$ is defined $\boldsymbol{l}' = \boldsymbol{F}\boldsymbol{x}$. As a result, it will generate a dense model with multiple images, obtaining more optimal processing times.

3. Estimation of vineyard yields

The measurement of vineyard yields is accomplished with a set of production components, such as volume, mass and the number of berries per bunch (Greven, 2007). This study attempts to establish these components, demonstrating the feasibility of scaling the proposed methodology to the total yield estimation of the vineyard ($\mathrm{kg} * \mathrm{m}^{-2}$). The current method improves classic and alternative methods (Kurtural and ÓDaniel, 2007) and the empirical relations proposed by Greven (2007). Different algorithms were implemented to analyze clusters from the metric point cloud dimensionally, obtaining the volume and weight, as well as determining the number of berries, following two computational strategies, as shown in Fig. 3. The first one is automatic and relies on the point cloud generated. The second one is a semi-automatic process and requires computer-aided design (CAD) models from the point cloud.

Both strategies are fed by external variables, the average volume of the berries (Vm) and the average density of the bunches (Dm) calculated by averaging the data acquired in laboratory tests. These variables depend on the area and year of the crop.

$$Vm = \frac{\sum_{i=1}^{i=n}(V/B)i}{n} \quad (5)$$

$$Dm = \frac{\sum_{i=1}^{i=n}(W/V)i}{n} \quad (6)$$

where Vm is the average berry volume calculated by means of the real bunch volume (V), the number of bunches (n) and the real number of berries per bunch (B); Dm is the average density of the bunch, and W is the real weight of the bunch.

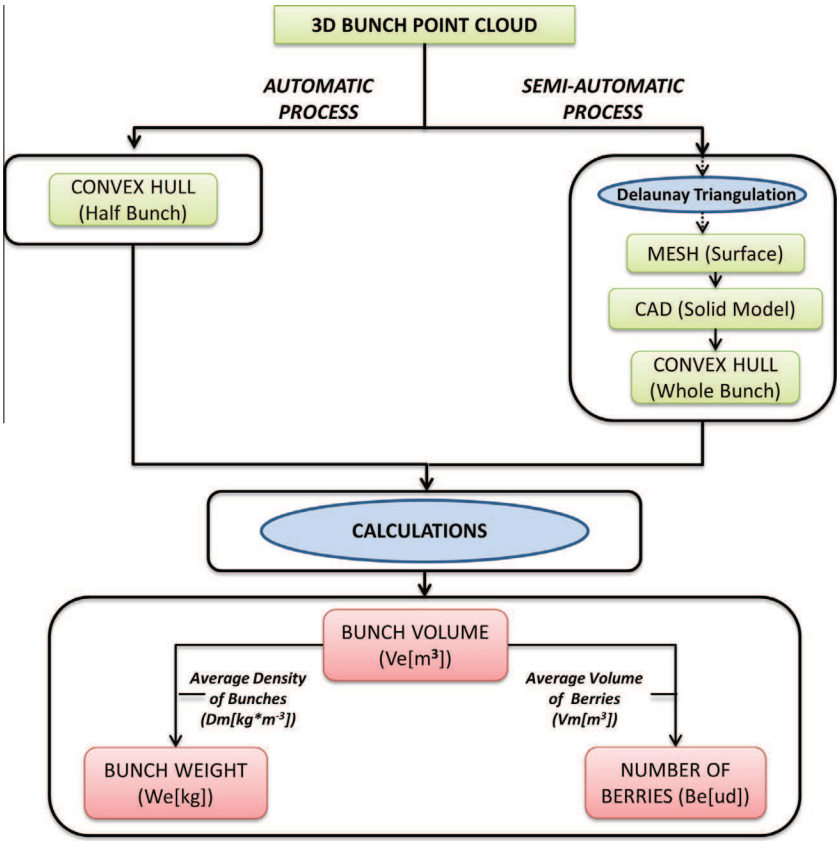

Fig. 3. Different computational strategies of vineyard production components from 3D bunch point cloud.

The two methods described are based on different modelling techniques of the 3D point cloud of the cluster. The first one is an automatic process supported by generating the convex hull (O'Rourke, 1994) of the 3D point cloud of the visible side of the cluster. This volume limited by the hull (*Vc*) collects half of the whole cluster due to the field of view of the camera and the limitations of the branches and leaves, closing the hidden side of the cluster by a flat surface. Because the convex hull includes empty spaces where there are no berries, as well as the exclusivity of the visible side of the bunch it is necessary to include an empirical correction factor (*K*) (Nuske et al., 2011; Nuske et al., 2012) that will refine the estimated volume (*Ve*).

The second strategy is based on a semi-automatic process supported by reverse engineering procedures that allows CAD models to be generated from 3D point clouds (DeLuca et al., 2006). It is noteworthy that there are still serious barriers in our knowledge of full automation in the conversion to CAD solid models, especially in the case of complex objects (Gonzalez-Aguilera et al., 2012). This approach requires the triangulation of the point cloud from the cluster to achieve the spatial topology required to model it. The meshing algorithm chosen was 3D Delaunay triangulation (Golias and Dutton, 1997) to obtain a TIN (Triangle Irregular Network). With this approach, the volume enclosed by the convex hull (*Vc*) of the whole cluster can be achieved, from modelling the individual berries of the visual side of the bunch and the subsequent symmetry. As in the automatic approach, an empirical correction factor (*K*) that refines the estimated volume (*Ve*) is required.

Fig. 4 shows both computational processes.

This second approach is more tedious. To obtain a CAD model close to reality, the mesh has to be repaired previously. This step uses the approximation of Attene (2010), which incorporates several automatic and sequential tasks:

- Filling of holes through algorithms of planar triangulations (Barequet and Sharir, 1995) or more complex approaches based on interpolators of radial basis function (Branch et al., 2006), the minimum distance (Dolenc and Makela, 1993) and the measurement of angles (Bøhn and Wozny, 1992; Varnuška et al., 2005).
- Repair of meshing gaps, based on minimum threshold distance algorithms (Rock and Wozny, 1992; Barequet and Kumar, 1997).
- Removal of topological noise, allowing the mesh to be re-triangulated locally (Guskov and Wood, 2001).
- Removal of geometric noise by algorithms that apply filters as anti-aliased Laplacians in general or specific zones (Fan et al., 2008).

After this reconstruction, the mesh has been modelled to obtain a solid CAD comprising two stages: segmentation and adjustment of basic primitives. As proposed by Wang et al. (2012), the segmentation process involves 3 steps:

- Plane segmentation using the region growing technique.
- Segmentation of quadric surfaces from knowledge of the vertex curvature obtained by fitting the local vicinity (Besl and Jain, 1988).
- Segmentation of free surfaces relying on the region growing technique to maximize the number of vertices connected topologically that can be generalized as a free surface of the B-spline type.

Once the geometry has been segmented, modelling continues with the setting of basic primitives. Thus, berries were approximated to spheres, extracted by an iterative adjustment of the minimization of the Euclidean distance from the mesh.

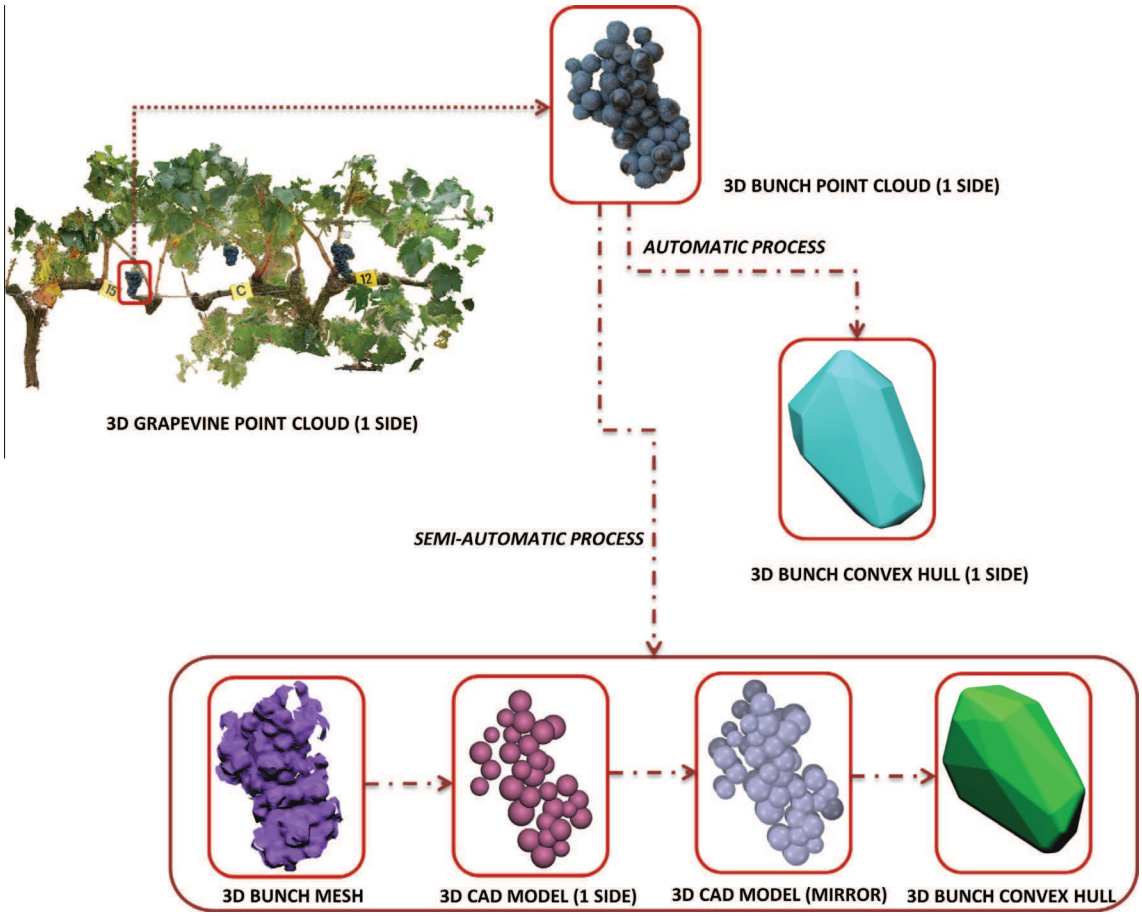

Fig. 4. Workflow of different computational processes to obtain the convex hull of the cluster.

The mathematical models implemented in both approaches are detailed below, where Eq. (7) shows the bunch volume estimated (*Ve*); bunch weight is estimated (*We*) in Eqs. (8) and (9) calculates the number of berries estimated per bunch (*Be*). *Vc* represents the volume limited by the convex hull and *K* is the empirical correction factor:

$$Ve = Vc * K \tag{7}$$

$$We = Vc * K * Dm \tag{8}$$

$$Be = Vc * K / Vm \tag{9}$$

Finally, a correlation between the calculated components and the groundtruth by a sampling of laboratory tests was established to analyze and validate the results acquired with both strategies.

4. Experimental results

Data collection was performed on the 20th of October 2013, on a day with bright and homogeneous lighting, at an experimental dry-farmed cv. Tempranillo (*Vitis vinifera* L.) vineyard of 1.05 ha, located 6 km from Logroño (lat. 42°26' N; long. 2°30' W; 455 m asl, La Rioja, Spain). Many studies have been conducted previously at this location (Romero et al., 2010; Vicente Renedo et al., 2007).

Tempranillo vines (clon RJ-26) were grafted onto Ritcher-110 rootstock and planted in 1995, following a between-row and within-row spacing of 2.90 m × 1.15 m respectively, with an East–West orientation. This corresponds to a density of 2998 vines/ha. The grapevines were spur-pruned on a bilateral cordon and trained to a VSP trellis system. The trellis featured a supporting wire at 0.70 m, two wires at 1.00 m above the ground for protection against wind damage, and a pair of movable shoot-positioned wires at 1.45 m.

Fig. 5. Image of trellis vineyards selected for this study.

Table 1
Technical specifications of the photographic sensor.

Canon EOS 500D	
Type	CMOS
Sensor size	22.3·14.9 mm
Total pixels	15.1 Mpíxels
Image size	4752·3168 pixels
Focal length	17 mm

Fig. 6. Example of matching points between images.

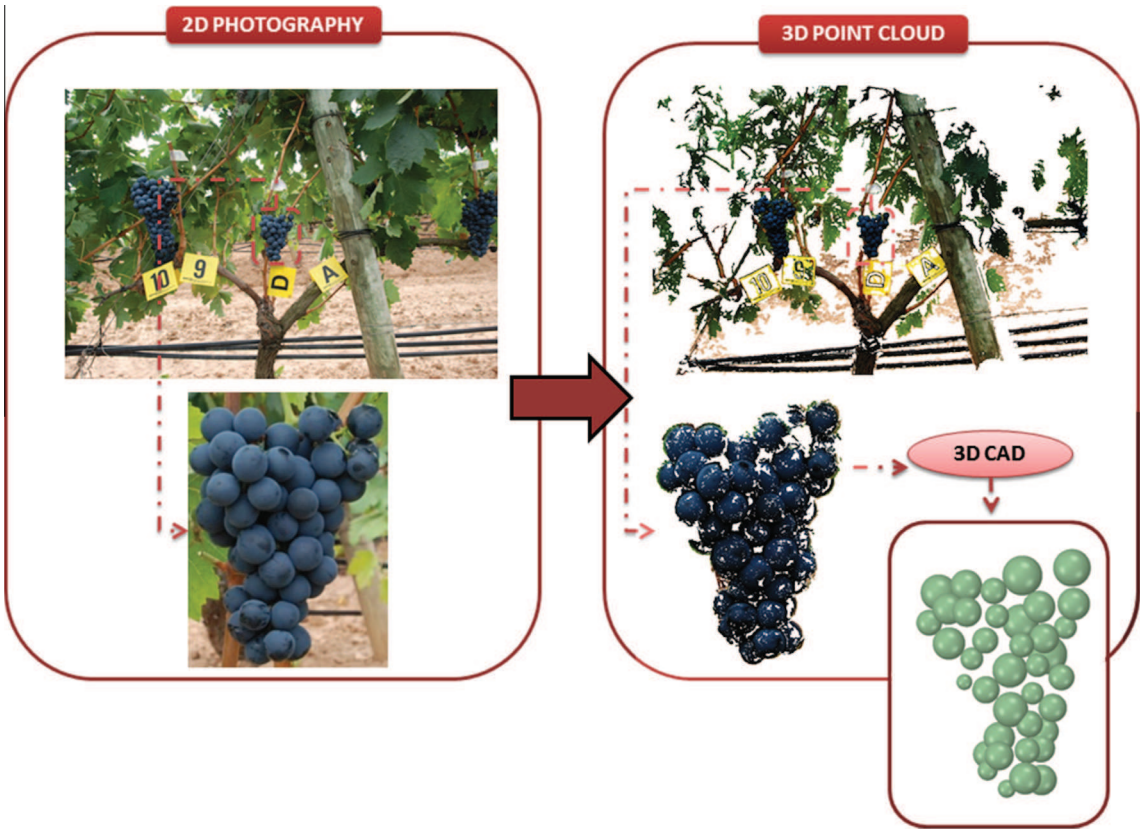

Fig. 7. 3D point cloud and CAD model of a cluster example from 2D images.

To validate the proposed method, 20 clusters from 14 trellis vines were chosen, taking photographs according to the protocol defined in Section 2.1. The selected strains were lightly defoliated to allow one side of the study clusters to be seen. Before taking the photographs, several artificial yellow targets were placed on the ground to allow the automatic scaling of point clouds (Fig. 5).

The main features of the camera used are shown in Table 1:

Images were taken using a fixed short focal length, with an of f/5.6 aperture, an exposure time faster than 1/160 s, ISO quality of 200 to decrease image noise, and without flash, owing to the shadow effects. The distance to the grapevine was approximately 2 m in order to maintain it inside the camera depth of field (DOF). The aperture was chosen to achieve an optimal compromise between exposure time, resolution and the DOF.

Photograph acquisition at such close distances requires the consideration of lens parameters, such as the Modulation Transfer Function (MTF), so the strains were centered in the image to achieve better resolution. Additionally, the MTF was taken into account for lens aperture selection (the lens "sweet" spot).

3D point cloud generation involves the identification and matching of homologous points between images, exemplified in Fig. 6 by straight white lines. The average number of homologous points between pairs of images was 580, obtained automatically through Micmac algorithm (Deseilligny and Clery, 2011). One of the keys to success in the matching process passes through acquiring pair of images with small baseline and thus guarantying high overlap between images. Moreover, the ORSA algorithm used in the matching process consists in introducing an *a contrario* (Desolneux et al., 2000) criterion to avoid the hard thresholds for inlier/outlier discrimination. Thus, the ORSA algorithm finds the right balance between the critical parameter σ and number of inliers by controlling the number of false alarms (Moisan et al., 2012).

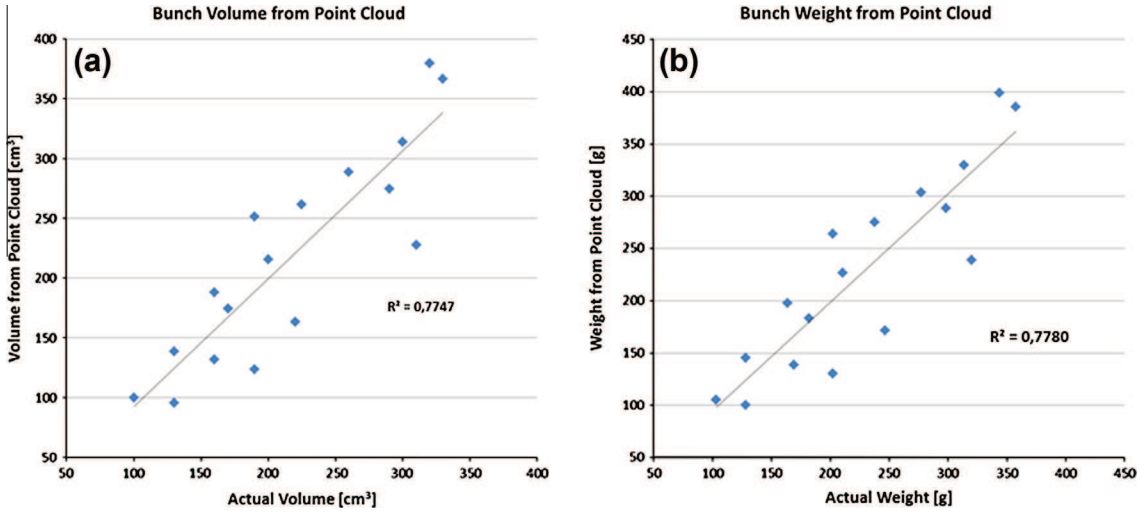

Fig. 8. Bunch volume (a) and weight (b) obtained automatically from point cloud.

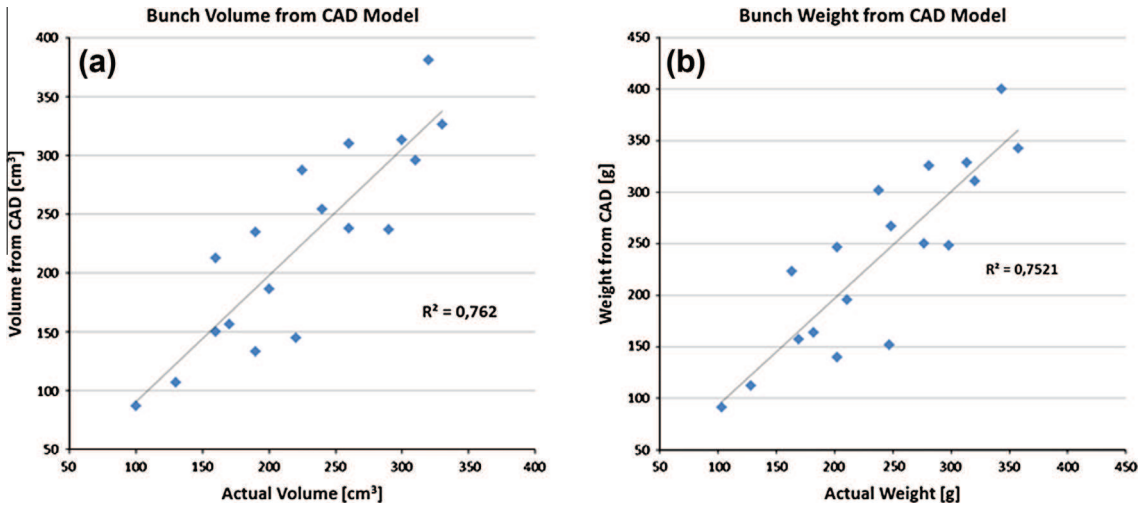

Fig. 9. Bunch volume (a) and weight (b) obtained semi-automatically from CAD model.

The dense point clouds generated have 4,276,000 points per vineyard, while the clusters alone have 96,460 points (as mean value). These points are utilizated to create the bunch mesh, having 90,779 points with a ground sample distance of 0.3 mm and a size of 8.3 kB (as mean value).

Fig. 7 shows scaled 3D models of a cluster example and CAD solids through 2D images, which were the inputs of the method proposed to estimate the vineyard yield.

The actual yield components were established by a laboratory test: volume calculation (immersion), weighing, and individual counting of berries per cluster. These laboratory tests which perform as a groundtruth were contrasted with estimated parameters, providing the error of each estimation. Owing to the nature of point clouds, the robust statistical parameter for defining the adjustment is MAD (median absolute deviation) (Mosteller and Tukey, 1977; Sachs, 1984) with respect to the median of the estimated values. Additionally, the Pope test (Pope, 1976) was applied for the detection and removal of the outliers. The final results are shown in Figs. 8–10.

- A coefficient of determination of 0.77 was achieved by comparing the actual volume of the cluster versus the volume estimated from the point cloud (Fig. 8a). The MAD had a value of 34 cm^3 when the median of the estimated volumes was 216 cm^3. In the case of bunch weight, an average coefficient of determination of 0.78 g was obtained (Fig. 8b), with a MAD of 35 g when the median was 227 g.
- On comparing the actual volume of the bunch with the estimated volume from CAD modelling, a coefficient of determination of 0.76 was obtained (Fig. 9a). The MAD was 33 cm^3, the median taking a value of 236 cm^3. When bunch weight was analyzed, a coefficient of determination of 0.75 was obtained (Fig. 9b), the MAD 35 g being when the median was 248 g.
- On testing the actual number of berries and the number of berries estimated by the point cloud, a determination value of 0.80 was obtained (Fig. 10a). The MAD of this fitting was 15 units, the median being 98 units. When this estimation was performed with CAD modelling, a coefficient of determination of 0.78 was obtained (Fig. 10b). In this case the MAD was 15 units when the median was 114 units.

From this analysis, it is possible to conclude that the semi-automatic process does not provide significant improvements, in contrast to the automatic one, which also has the advantage of a

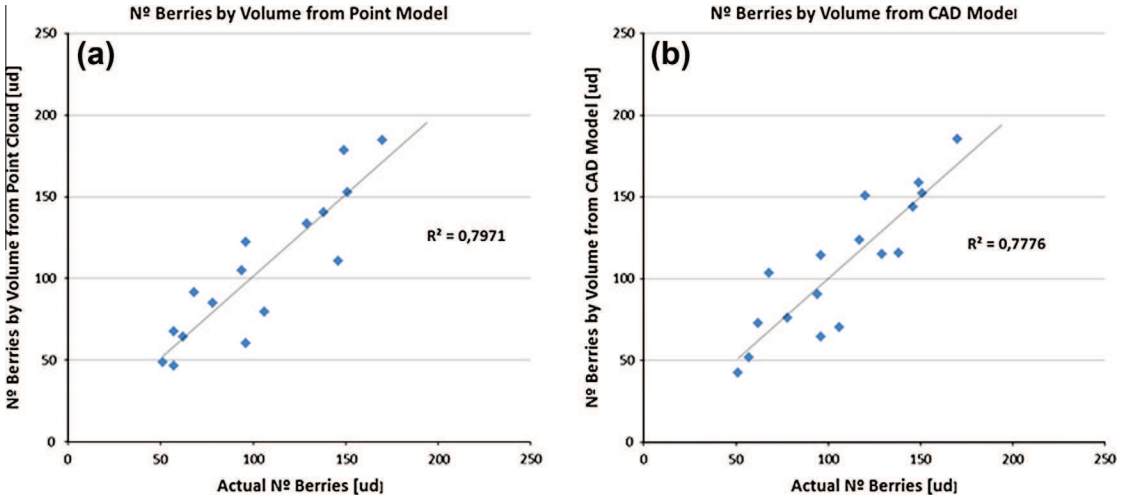

Fig. 10. Number of berries obtained automatically from point cloud (a) and number of berries obtained semi-automatically from CAD model (b).

reduced processing time and does not require human interaction. It significantly decreases subjective variability as well as featuring reduced associated costs and time saving. Furthermore, comparing the coefficients obtained with other yield estimation studies, this method can be cataloged as a great accurate one. Related to this assertion, Diago et al. (2012) achieved a R^2 of 0.73 between the observed and predicted yield values. Dunn and Martin (2004) succeeded a R^2 of 0.85 between grape weight and the ratio of grape pixels to total image pixel. Both cases used approaches based on supervised classification methodologies and an limited 2D analysis of bunch morphology. Additionally, both approaches required the employment of white screen to avoid the background influence which limits their effectiveness and automation in field.

5. Conclusions

This research presents a non-invasive low-cost method with application to precision viticulture that consists of vineyard yield estimation. The method is fast, reliable, robust and objective, and could serve to take decisions in advance regarding actions to be taken in vineyards, predicting the results and planning the vintage optimally. The method developed relies on the adaptation of the PW software tool, which allows the metric reconstruction and dimensional analysis of bunches from grapevine images taken in field conditions. The groundtruth established in laboratory tests ensures that the method is precise in complex agronomic scenarios and in trellis vine configurations, which are more complex to photograph than classic pruned configurations. The advantages of PW include process automation, sufficient quality to generate dense resolution models equivalent to the pixel size of the image, and low cost and ease of use.

Regarding the two processes developed to estimate vineyard production parameters (point cloud-automatic and CAD-semiautomatic), the results show that there is no significant improvement in CAD berry modelling. This is why the automatic methodology using integrated algorithms in PW software was selected for the present work. In addition, working only on one side of the cluster, the visible side, is feasible for approximating the whole bunch with an accurate and precise fit.

This methodology can be extrapolated to the whole of the vineyard, measuring its yield. Because this method is based on non-invasive technologies through a passive sensor, the constraints mainly depend on weather conditions, such as homogeneous lighting and the absence of rain and strong winds. By using artificial light and simple screens to diffuse light, several restrictions can be overcome. Since future prospects will address cluster compactness and its relationship to volumes, another action to be developed in the future will be to design and build a platform that supports the configuration of the image acquisition protocol described in Section 2.1 and that can be loaded on a mobile platform such as a quad. This would also allow the optimal distances between sensors to be determined and calibrated and hence the possibility of scaling models without targets, significantly optimizing the time devoted to field work and data processing.

Acknowledgments

Authors would like to thank the Instituto de Ciencias de la Vid y el Vino (ICVV) from the CSIC, the University of La Rioja and the Department of Agriculture of the Government of La Rioja, for allowing us to use their facilities and their collaboration during the experimental phase of this research. Special thanks to Javier Tardáguila, Mª Paz Diago, Borja Millán and Rubén Urraca.

References

Aguilar, M.A., Pozo, J.L., Aguilar, F.J., Sanchez-Hermosilla, J., Páez, F.C., Negreiros, J., 2008. 3D surface modelling of tomato plants using close-range photogrammetry. Int. Archives Photogr., Remote Sens. Spatial Informat. Sci., 330.

Akca, D., Gruen, A., 2007. Generalized Least Squares Multiple 3D Surface Matching. Institute of Geodesy and Photogrammetry, ETH Zurich.

Attene, M., 2010. A lightweight approach to repairing digitized polygon meshes. Visual Comput. 26 (11), 1393–1406.

Barber, C.B., Dobkin, D.P., Huhdanpaa, H., 1996. The quickhull algorithm for convex hulls. ACM Transact. Math. Software (TOMS) 22 (4), 469–483.

Barequet, G., Kumar, S., 1997. Repairing CAD models. In: Visualization'97, Proceedings, IEEE, pp. 363–370.

Barequet, G., Sharir, M., 1995. Filling gaps in the boundary of a polyhedron. Comput. Aided Geom. Des. 12 (2), 207–229.

Battany, M., 2008. A practical method for counting berries based on image analysis. In: 2nd Annual National Viticulture Research Conference, University of California, Davis, USA, 4–5, July 9–11.

Bay, H., Tuytelaars, T., Van Gool, L., 2006. Surf: speeded up robust features. In: Computer Vision–ECCV 200. Springer, Berlin Heidelberg, pp. 404–417.

Besl, P.J., Jain, R.C., 1988. Segmentation through variable-order surface fitting. Pattern Anal. Machine Intell., IEEE Trans. on 10 (2), 167–192.

Blom, P.E., Tarara, J.M., 2009. Trellis tension monitoring improves yield estimation in vineyards. HortScience 44 (3), 678–685.

Bøhn, J.H., Wozny, M.J., 1992. Automatic CAD-model repair: shell-closure. In: Proc. Symp. on Solid Freeform Fabrication, pp. 86–94.

Branch, D., Dang, L.C., Hall, N., Ketchum, W., Melakayil, M., Parrent, J., Baron, E., 2006. Comparative direct analysis of type Ia supernova spectra. II. Maximum light. Publ. Astron. Soc. Pac. 118 (842), 560–571.

Chherawala, Y., Lepage, R., Doyon, G., 2006. In food grading/sorting based on color appearance trough machine vision: the case of fresh cranberries. Informat. Commun. Technol., 1540–1545, ICTTA '06. 2nd, 0–0 0.

Clingeleffer, P.R., Martin, S., Krstic, M., Dunn, G.M., 2001. Crop development, crop estimation and crop control to secure quality and production of major wine grape varieties: a national approach: final report to grape and wine research development corporation. Grape and Wine Research & Development Corporation.

DeLuca, J.G., Gall, W.E., Ciferri, C., Cimini, D., Musacchio, A., Salmon, E., 2006. Kinetochore microtubule dynamics and attachment stability are regulated by Hec1. Cell 127 (5), 969–982.

Deseilligny, M.P., Clery, I., 2011. Apero, an open source bundle adjustment software for automatic calibration and orientation of set of images. In: Proceedings of the ISPRS Symposium, 3DARCH11, pp. 269–277.

Desolneux, A., Moisan, L., Morel, J.M., 2000. Meaningful alignments. Int. J. Comput. Vision 40 (1), 7–23.

Diago, M.-P., Correa, C., Millán, B., Barreiro, P., Valero, C., Tardaguila, J., 2012. Grapevine yield and leaf area estimation using supervised classification methodology on RGB images taken under field conditions. Sensors 12, 16988–17006.

Djuricic, A., Weinmann, M., Jutzi, B., 2014. Potentials of small, lightweight and low cost multi-echo laser scanners for detecting grape berries. The International Archives of the Photogrammetry, Remote Sensing and Spatial Information Sciences, vol. XL-5, 2014. In: ISPRS Technical Commission V Symposium, 23–25 June 2014, Riva del Garda, Italy.

Dolenc, A., Makela, I., 1993. Some efficient procedures for correcting triangulated models. In: Proceedings of Solid Freeform Fabrication Symposium, pp. 126–134.

Dunn, G.M., Martin, S.R., 2003. The current status of crop forecasting in the Australian wine industry. ASVO Seminar Series: Grapegrowing at the Edge, 24.

Dunn, G.M., Martin, S.R., 2004. Yield prediction from digital image analysis: a technique with potential for vineyard assessments prior to harvest. Aust. J. Grape Wine Res. 10 (3), 196–198.

Fan, Y.Z., Tam, B.S., Zhou, J., 2008. Maximizing spectral radius of unoriented Laplacian matrix over bicyclic graphs of a given order. Linear and Multilinear Algebra 56 (4), 381–397.

Fischler, M.A., Bolles, R.C., 1981. Random sample consensus: a paradigm for model fitting with applications to image analysis and automated cartography. Commun. ACM 24 (6), 381–395.

Golias, N.A., Dutton, R.W., 1997. Delaunay triangulation and 3D adaptive mesh generation. Finite elements Anal. Des. 25 (3), 331–341.

Gonzalez-Aguilera, D., Del Pozo, S., Lopez, G., Rodriguez-Gonzalvez, P., 2012. From point cloud to CAD models: Laser and optics geotechnology for the design of electrical substations. Opt. Laser Technol. 44 (5), 1384–1392.

González-Aguilera, D., Guerrero, D., Hernández-López, D., Rodríguez-Gonzálvez, P., Pierrot, M., Fernández-Hernández, J., 2013. PW, Photogrammetry Workbench. <http://www.isprs.org/catcon/catcon6.aspx> (accessed 30.04.14).

Greven, M., 2007. Manual for yield forecasting in Sauvignon Blanc grapes. Marlborough Wine Research Centre.

Gruen, A., 1985. Adaptive least squares correlation: a powerful image matching technique. South African J. Photogr., Remote Sens. Cartogr. 14 (3), 175–187.

Guskov, I., Wood, Z.J., 2001. Topological noise removal. In: 2001 Graphics Interface Proceedings. Ottawa, Canada, 19.

Hartley, R., Zisserman, A., 2003. Multiple View Geometry in Computer Vision. Cambridge University Press.

Herrero Langreo, A., Barreiro Elorza, P., Santamaria, D., Paz, M., Baluja, J., Ochagavia, H., 2010. Pixel classification through mahalanobis distance for identification of grapevine canopy elements on rgb images.

Hirschmuller, H., 2005. Accurate and efficient stereo processing by semi-global matching and mutual information. In: Computer Vision and Pattern Recognition. CVPR 2005. In: IEEE Computer Society Conference on, vol. 2, pp. 807–814.

Joglekar, J., Gedam, S.S., 2012. Area based image matching methods—a survey. Int. J. Emerg. Technol. Adv. Eng. 2, 130–136.

Kraus, K., 1993. Photogr. Fundamentals Standard Processes, vol. 1. DummlersVerlag, Bonn, Germany, ISBN 3-427-78684-6.

Kurtural, K., ÓDaniel, B., 2007. Crop estimation in vineyards. UK Cooperat. Extens. Service Univ. Kentucky-College Agric., 45.

Lange, B., Chang, C., Suma, E., Newman, B., Rizzo, A.S., Bolas, M., 2011. Development and evaluation of low cost game-based balance rehabilitation tool using the microsoftkinect sensor. Engineering in Medicine and Biology Society, EMBC, In: 2011 Annual International Conference of the IEEE, pp. 1831–1834.

Longuet-Higgins, H.C., 1987. A computer algorithm for reconstructing a scene from two projections. In: Fischler, M.A., Firschein, O. (Eds.), Readings in Computer Vision: Issues, Problems, Principles, and Paradigms, pp. 61–62.

Lowe, D., 1999. Object recognition from local scale-invariant features. In: International Conference on Computer Vision, Corfu, Greece.

Lowe, D.G., 2004. Distinctive image features from scale-invariant keypoints. Int. J. Comput. Vision 60 (2), 91–110.

Lumme, J., Karjalainen, M., Kaartinen, H., Kukko, A., Hyyppä, J., Hyyppä, H., et al., 2008. Terrestrial laser scanning of agricultural crops. Int. Archives Photogr., Remote Sens. Spatial Informat. Sci. 37, 563–566.

Martin, S., Dunstone, R., Dunn, G., 2003. How to Forecast Wine Grape Deliveries Using Grape Forecaster Excel Workbook Version 7. GWRDC, Adelaide, Australia, p. 100.

Matas, J., Chum, O., Urban, M., Pajdla, T., 2004. Robust wide-baseline stereo from maximally stable extremal regions. Image Vis. Comput. 22 (10), 761–767.

Moisan, L., Stival, B., 2004. A probabilistic criterion to detect rigid point matches between two images and estimate the fundamental matrix. Int. J. Comput. Vision 57 (3), 201–218.

Moisan, L., Moulon, P., Monasse, P., 2012. Automatic homographic registration of a pair of images, with a contrario elimination of outliers. Image Processing On Line, 10.

Morel, J.M., Yu, G., 2009. ASIFT: a new framework for fully affine invariant image comparison. SIAM J. Imag. Sci. 2 (2), 438–469.

Mosteller, F., Tukey, J., 1977. Data Analysis and Regression. Addison-Wesley, Upper Saddle River, NJ.

Nuske, S., Achar, S., Bates, T., Narasimhan, S., Singh, S., 2011. Yield estimation in vineyards by visual grape detection. Intelligent Robots and Systems (IROS). In: 2011 IEEE/RSJ International Conference on, pp. 2352–2358.

Nuske, S., Gupta, K., Narasimhan, S., Singh, S., 2012. Modeling and Calibrating Visual Yield Estimates in Vineyards. In: Yoshida, K., Tadokoro, S. (Eds.), Field and Service Robotics, vol. 92. Springer, Berlin Heidelberg, pp. 343–356.

O'Rourke, J., 1994. Computational Geometry. C. Press Syndicate of the University of Cambridge, p. 118.

Pope, A.J., 1976. The statistics of residuals and the detection of outliers.

Quan, L., 2010. Image-Based Modeling. Springer, New York.

Roby, G., Harbertson, J.F., Adams, D.A., Matthews, M.A., 2004. Berry size and vine water deficits as factors in winegrape composition: anthocyanins and tannins. Aust. J. Grape Wine Res. 10 (2), 100–107.

Rock, S.J., Wozny, M.J., 1992. Generating topological information from a bucket of facets. In: Solid Freeform Fabrication Symposium Proceedings. The University of Texas at Austin, Austin, pp. 251–259.

Romero, I., García-Escudero, E., Martín, I., 2010. Effects of leaf position on blade and petiole mineral nutrient concentration of Tempranillo grapevine (*Vitis vinifera* L.). Am. J. Enol. Viticulture 61 (4), 544–550.

Sachs, L., 1984. Applied Statistics: A Handbook of Techniques. Springer-Verlag, New York, p. 253.

Serrano, L., González-Flor, C., Gorchs, G., 2012. Assessment of grape yield and composition using the reflectance based water index in Mediterranean rained vineyards. Remote Sens. Environ. 118, 249–258.

Sethian, J.A., 1999. Level Set Methods and Fast Marching Methods: Evolving Interfaces in Computational Geometry, Fluid Mechanics, Computer Vision, and Materials Science, vol. 3. Cambridge University Press.

Smith, S.M., Brady, J.M., 1997. SUSAN—a new approach to low level image processing. Int. J. Comput. Vision 23 (1), 45–78.

Varnuška, M., Parus, J., Kolingerová, I., 2005. Simple holes triangulation in surface reconstruction. In: Proceedings of ALGORITMY, pp. 280–289.

Vicente Renedo, T., Martínez García, J., Chavarri, J.B., Marín, M., González Marcano, S., Domínguez Miguel, N., Villar Capellán, R., 2007. Preservation of genetic heritage of authorized vinifera grapes and rootstocks in Rioja DOC [Designation of Origin]. In: Foro Mundial del Vino, 5, Logroño (España), 28–30 Mar 2006. GLR, CAGDR.

Wang, J., Gu, D., Yu, Z., Tan, C., Zhou, L., 2012. A framework for 3D model reconstruction in reverse engineering. Comput. Ind. Eng. 63 (4), 1189–1200.

Whalley, J., Shanmuganathan, S., 2013. In Applications of image processing in viticulture: A review. In: 20th International Congress on Modelling and Simulation, Adelaide, Australia, pp. 531–537.

Wolpert, J., Vilas, E., 1992. Estimating vineyard yields: introduction to a simple, two-step method. Am. J. Enol. Viticul. 43 (4), 384–388.

Trees
DOI 10.1007/s00468-016-1366-9

ORIGINAL ARTICLE

Dense Canopy Height Model from a low-cost photogrammetric platform and LiDAR data

Mónica Herrero-Huerta[1] · Beatriz Felipe-García[2] · Soledad Belmar-Lizarán[3] · David Hernández-López[3] · Pablo Rodríguez-Gonzálvez[1] · Diego González-Aguilera[1]

Received: 5 January 2015 / Accepted: 15 February 2016

Abstract
Key message **Low-cost methodology to obtain CHMs integrating terrain data from LiDAR into photogrammetric point clouds with greater spatial, radiometric and temporal resolution due to a correction model.**
Abstract This study focuses on developing a methodology to generate a Dense Canopy Height Model based on the registration of point clouds from LiDAR open data and the photogrammetric output from a low-cost flight. To minimise georeferencing errors from dataset registration, terrain data from LiDAR were refined to be included in the photogrammetric point cloud through a correction model supported by a statistical analysis of heights. As a result, a fusion point cloud was obtained, which applies LiDAR to characterize the terrain in areas with high vegetation and utilizes the greater spatial, radiometric and temporal resolution of photogrammetry. The obtained results have been successfully validated: the accuracy of the fusion cloud is statistically consistent with the accuracies of both clouds based on the principles of classical photogrammetry and LiDAR processing. The resulting point cloud, through a radiometric and geometric segmentation process, allows a Dense Canopy Height Model to be obtained.

Keywords Dense Canopy Height Model · Photogrammetry · LiDAR · Data fusion · Low-cost platform · Radiometric segmentation

Communicated by E. Priesack.

✉ Mónica Herrero-Huerta
monicaherrero@usal.es

[1] Department of Cartographic and Land Engineering, Higher Polytechnic School of Avila, University of Salamanca, Hornos Caleros 50, 05003 Ávila, Spain

[2] Forestry and Natural Spaces Service, Agriculture, Environment and Rural Development Department, Castilla-La Mancha Regional Government, C/Mayor 46, 02001 Albacete, Spain

[3] Institute for Regional Development (IDR), University of Castilla La Mancha, 02071 Albacete, Spain

Introduction

The estimation of dasometric variables of interest for forest management (diameter, height, basal area, volume of growing stock, biomass, species, etc.) has traditionally been done via pilot samplings of field inventories. The advent of new remote sensing technologies and photogrammetry has opened up a new field of possibilities for carrying out such work, and such methods are advantageous in the economic costs involved, the time invested and estimation errors.

The application of active high-resolution remote sensors affords high accuracy in height measurements and a good prediction of dasometric variables (Popescu et al. 2002). In particular, the capacity of active light detection and ranging (LiDAR) sensors to penetrate and acquire three-dimensional measurements of the canopy at different heights (Wulder et al. 2013) allows improved estimation of variables such as biomass, volume and basal area over that of other sensors that gather two-dimensional data, such as photographic or radiometric systems. Since the late 1980s, studies have been published based on profiles acquired using airborne laser systems (ALS—airborne laser scanner) for the estimation of biomass and volumes (Nelson et al. 1988) as well as simple and multiple linear models (Nelson et al. 1997; Means et al. 2000) to analyse the effect of the lag transformation of the forest variable. Later studies

Published online: 25 February 2016

(Naesset 1997; Nelson et al. 2003) have improved upon studies of forest inventories by further exploiting instrumentation, capture methodology and information processing. Of interest are the studies of Lim and Treitz (2004) and Naesset (2004), in which the authors applied rodal[1] methods to generate inventories, as well as individual tree methods,[2] in which methodological compendia are described with the algorithms used in each estimation. Comparisons of different LiDAR inventories (Naesset et al. 2005) and of photointerpretation and LiDAR (Eid et al. 2004) have been published.

In recent years, many studies and methodological review articles have been published describing the operating capacity and definitive implementation of LiDAR technology in the context of the extraction of forest variables (Hyyppä et al. 2008; Wulder et al. 2012; Kankare et al. 2013). Benko and Balenovic (2011) reported new experiences in inventory tasks and forest management in different environments, with an analysis of the accuracies achieved. Richardson and Moskal (2011) established classifications of vegetation via tree height and density. Another interesting case is the guide produced by the Canadian Forest Service as a current reference document based on all previously published studies. The guide provides a series of recommendations for inventorying forest applications based on rodal methods using LiDAR data (White et al. 2013a). Gleason and Im (2012) applied different automated learning approaches to estimate biomass in forests from aerial LiDAR data. The FullWave airborne LiDAR systems provide large bodies of information about the overall plant and forest structure in great detail (Weinacker et al. 2004; Mallet and Bretar 2009). However, the complex and tedious processing involved and the costs of such technology are definite drawbacks (Chauve et al. 2007; Gupta et al. 2010).

Magnussen et al. (2007) used Landsat satellite images to create inventories according to the spatial resolution factor. Similarly, LiDAR techniques have been applied to images captured by different remote sensing systems (Magnussen et al. 2000; Wulder et al. 2008a, b; Willers et al. 2012; Mora et al. 2013) and by traditional photogrammetry (Magnusson et al. 2007).

Within the framework of the National Aerial Orthoimage Plan, low-density (0.5 points/m^2) LiDAR sensor flights have been performed since 2008 throughout the Spanish territory. Thus, in recent years, different forest research teams have tested different applications using data from this source (Estornell et al. 2012; González-Ferreiro et al. 2014; Gonzalez et al. 2012; Navarro-Cerrillo et al. 2014). The problem with these mass data acquisitions is that they are very costly, their resolution is low, and they are implemented individually at a given moment in time.

Currently, conventional photogrammetry is a complementary alternative to custom LiDAR flights to obtain 3D-point clouds and digital surface models (DSMs) because the associated costs are lower (Järnstedt et al. 2012); the accuracy is greater; and the spatial, radiometric and temporal resolution is greater (Bohlin et al. 2012). The complementary nature of the two techniques can be seen in the greater planimetric accuracy of photogrammetry than LiDAR and the greater altimetric accuracy of the latter than of the former. Nevertheless, photogrammetry is incapable of generating a Digital Terrain Model (DTM) in zones covered by vegetation, and LiDAR information must be used to generate reference surfaces for the collection of vegetation heights (Järnstedt et al. 2012). As an advantage of the photogrammetric point cloud, White et al. (2013b) cite the ability to interpret species composition as well as the maturity and health of vegetation.

With the development of manned and unmanned low-cost aerial platforms (RPAS—Remotely Piloted Aircraft Systems), conventional photogrammetric data collection and analysis can still be performed. Tao et al. (2011) used dense photogrammetric point clouds obtained with RPAS over forested areas and obtained information about the tree density, its composition and changes in the forest canopy. Other authors (Jaakkola et al. 2010; Wallace et al. 2012) have combined cameras and light LiDAR systems on RPAS, thus allowing both sensors to be used at the same time. Finally, special attention should be paid to the study of Lisein et al. (2013), in which the authors generated a Canopy Height Model (CHM) of a hybrid nature, combining the DSM obtained by correlating images from a non-metric camera and an RPAS with a DTM obtained from ALS data to estimate different forest parameters.

The aim of the present work was to develop a low-cost, efficient and precise methodology to obtain CHMs destined for forest inventories such a stratification of forest masses or a stock calculation and for fire studies obtaining combustible models. This was achieved by integrating LiDAR terrain data with minor temporal variability, which are freely available from the National Geographic Institute of Spain, into photogrammetric point clouds obtained using a low-cost platform, for a desired area and time. Thus, we combined LiDAR's terrain-sensing capacity in densely vegetated zones with the greater spatial, radiometric and temporal resolution offered by low-cost photogrammetry in plant cover zones. A correction model was constructed for the two data sources to minimise the georeferencing errors produced by the low-cost photogrammetric process, thereby obtaining a registration accuracy in agreement with the accuracies of

[1] Rodal method: methods applied to a surface with similar arboreal characteristics.

[2] Individual-tree methods: methods applied differentially to each tree.

the point clouds generated by the two techniques. During data analysis, following the recommendations of Wang et al. (2007), we also incorporated a supervised classification of the vegetation based on image colour that allows morphological classification types to be improved. The low-cost photogrammetric platform we used was a powered paraglider trike, designed and developed by the Institute for Regional Development of the University of Castilla-La Mancha. The greatest advantage offered by this type of manned platform is its flexibility of flight, autonomy and payload capacity, allowing data acquisition over an extensive area using multiple sensors to be integrated without constraints on time, weight or volume.

Materials and methods

The proposed methodology uses LiDAR open data freely available from the National Geographic Institute of Spain (IGN 2015) with a spatial resolution of 0.5 points/m^2. The aerial LiDAR data were revised by visual inspection and later by manual refinement, correcting errors in the initial automatic classification and thus obtaining well-coded terrain points. To assess the quality of the classification, the initial and filtered data were contrasted by means of a confusion matrix (Kohavi and Provost 1998).

According to the technical specifications of the National Aerial Orthoimage Plan (CNIG 2009), based on the type of terrain and the vegetation, an altimetric accuracy of 0.40 m was established.

Equipment

The following equipment was employed for photogrammetric data acquisition:

- A Leica System 1200 GNSS-RTK device was used for surveying control and check points, with a relative and absolute precision better than 0.03 and 0.05 m, respectively.
- A compact Olympus EP-1 camera, the first camera which meets the design standards of the micro four thirds (MFT) system. Its main features are shown in Table 1.
- A manned aerial platform supported by a powered paraglider (PPG) trike built by Airges (Fig. 1) was used (Ortega-Terol et al. 2014). Its technical specifications are shown in Table 2. The Olympus EP-1 camera was installed aboard the PPG trike using an auto-stabilised mounting platform. The potential benefits of this low-cost system are evident: a payload capacity that allows the system to be loaded with a large number of sensors that could be used for multispectral studies; the

Table 1 Technical specifications of the photographic sensor

Olympus EP1	
Type	CMOS
Sensor size (max. resolution)	4032 × 3024 pixels
Sensor size	17.3 × 13 mm
Pixel size (sensor geometric resolution)	0.0043 mm
Focal length	17 mm
Total pixels	12.3 MPixel
Aperture	*f*/2.8

Fig. 1 Aerial photogrammetric platform (PPG trike) with the gimbal shown (*white rectangle*)

Table 2 Technical specifications of the manned aerial platform: PPG trike

Parameter	Value
Empty weight	110 kg
Maximum load	220 kg
Autonomy	3.5 h
Maximum speed	60 km/h
Motor	Rotax 503
Tandem paraglide	MACPARA Pasha 4
Emergency system	Ballistic Parachutes GRS 350
Gimbal	Stabilized with 2 degrees of freedom
Minimum sink rate	1.1
Maximum glide	8.6
Plant surface	42.23 m^2
Projected area	37.8 m^2
Wingspan	15.03 m
Plant elongation	5.35
Central string	3.51 m
Boxes	54
Zoom factor	100 %

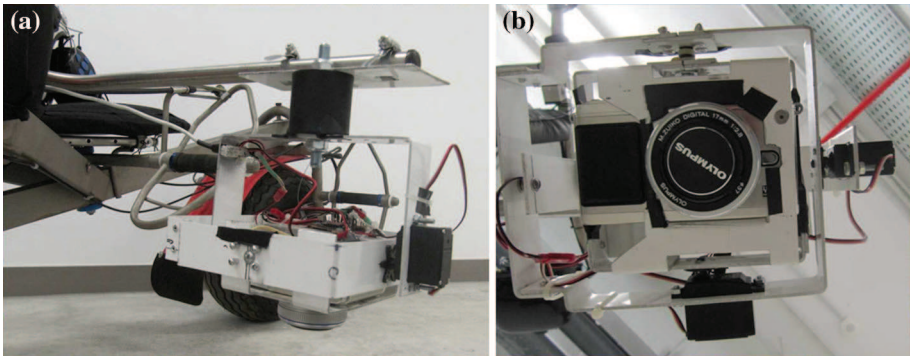

Fig. 2 Gimbal platform (auto-stabilised mounting platform). **a** Elevation view and **b** plan view

flexibility and autonomy of flying that offers the data acquisition over extensive areas.

- The PPG was equipped with a low-cost multi-sensor gimbal (stabilised platform), supporting the digital camera. The gimbal includes two servomotors oriented on the *x* and *y* axes to accurately maintain the camera's vertical position along the flight paths. The servomotors are controlled by an Arduino board, which incorporates an IMU with 6 degrees of freedom: three accelerometers with a range of ± 3.6 G m/s^2, a double-shaft gyroscope (for pitch and roll) and an additional gyroscope for yaw (both gyroscopes have a measurement range of $\pm 300°$/s). The software developed to control the device is based on Quadl_mini V 20 software, with DCM (Direction Cosine Matrix) as the IMU management algorithm (Premerlani and Bizard 2014). Figure 2 shows the gimbal platform.
- The system included a low-cost GNSS system based on a single-frequency receptor, receiving signals from a GPS constellation and Satellite Based Augmentation System (SBAS) (NavCen 2008). The GNSS antenna is installed on the camera platform close to the optical centre of the camera to minimise the baseline. To improve the GNSS altitudinal accuracy, which affects the final GSD, a DigiFly VL100 barometer was installed. Thus, horizontal positioning during flight was performed using the GNSS system's National Marine Electronics Association (NMEA) protocol using RTKNAVI software (Takasu 2009), with corrections from the ground from similar equipment, allowing DGPS accuracies higher than 1.50 m in planimetry and 2 m in altimetry to be achieved in real time as well as accuracies higher than 0.50 m in three dimensions in post-processing.

Flight planning and execution

Proper flight planning is important to ensure that the captured photogrammetric data will fit the desired theoretical parameters; planning also optimises available resources and ensures higher quality images, minimising capture time. Flight planning was conducted with software developed by the IDR (Institute of Regional Development of Castilla-La Mancha, Spain), called PFlip, utilising fundamentals of photogrammetry, the sensor configuration, and the Digital Terrain Model (Hernández-López et al. 2013).

First, the study area was defined, followed by the flight strips. Furthermore, additional constraints such as a minimum forward overlap of 70 % and a minimum side overlap of 30 % were established to ensure automatic detection of tie points (Järnstedt et al. 2012). Then, the flight planning process defined the position and orientation of the camera, the design of different blocks of images, the overlaps between different images, the necessary shot angles and the scale, as defined by the choice of pixel size on the ground (GSD).

The geomatic information required for the flight planning process was obtained at no cost from the National Center of Geographic Information in Spain (CNIG 2015), from its National Aerial Orthoimage Plan, with a GSD of 0.25 m and a Digital Terrain Model with a 5-m grid resolution.

Flight planning was performed by considering the relationship among the flight height over the ground (H), the GSD, the focal length of the sensor (f) and the pixel size, as described in Eq. (1).

$$\frac{f}{H} = \frac{\text{pixel size}}{\text{GSD}} \tag{1}$$

Considering Eq. (1), the characteristics of the camera (Table 1) and the required GSD of 0.08 m, a flight height over the ground of 316 m was obtained. Based on the technical specifications of the National Aerial Orthoimage Plan (CNIG 2009), an 'a priori' altimetric accuracy of 0.10 m was estimated for the photogrammetric cloud.

The parameters that define image capture are determined during flight execution depending on the light conditions, the camera quality and flight speed. Thus, the camera configuration was established with a camera-

shooting interval of 4 s and a maximum flight speed of 14 m/s, which guaranteed a forward overlap of 70 %. A shutter speed of 1/1000 s was adequate for this speed because the equivalent terrain displacement would be 0.01 m, which was lower than 1/5 pixel, an insignificant value for study purposes. An ISO of 125 was used with a fixed focal length at infinity.

A topographic survey campaign was established to obtain absolute georeferencing and a model scaled through artificial accuracy targets. Targets were distributed along the study area so that they remained visible through vegetation for photogrammetric capture. Moreover, these targets were marked and their size confirmed to rule out effects from neighbouring pixels (35 cm diameter).

Photogrammetric processing

Low-cost photogrammetric workflow

Once the aerial imagery had been acquired, conventional photogrammetric processing began, relying on an image-based modelling technique. In an attempt to guarantee automation and quality, a combination of photogrammetric and computer vision algorithms was required. This approach allows data to be acquired remotely with great efficiency and accuracy, affording radiometric characteristics to the point cloud. Photogrammetry Workbench software (PW) developed by the authors (González-Aguilera et al. 2013) was used for three steps. First, the images were matched by the SIFT algorithm (Lowe 2004), which allowed the detection of the scene's points of interest. Second, the camera orientations were computed using the tie-points calculated in the previous step and the coordinates of the artificial ground targets located in the flight area (Pierrot-Deseilligny and Clery 2011). In this process, the external camera parameters (position and orientation) and the internal camera parameters were solved by self-calibration. Finally, a textured point cloud was obtained by means of ray intersection (Kraus 2007). To solve this process, an semi-global matching (SGM) technique (Pierrot-Deseilligny and Clery 2011) was applied.

Photogrammetric point cloud processing

Owing to the massive and automated nature of the photogrammetric point cloud, it was necessary to treat the cloud to remove outliers and encode the information. More precisely, a clean-up and classification process was used; this approach is schematised in Fig. 3. After removing the outliers produced by matching, the vegetation was distinguished via radiometric segmentation. Following this step, we established geometric classification of the "non-vegetation" class to differentiate it from "ground", refining the results via a second iteration. Once the uncertain points in the "ground" class and the isolated terrain points had been removed, we classified the other points into different semantic categories using the Axelsson algorithm (1999): "ground", "low vegetation", "medium vegetation", "high vegetation", "building" and "noise", according to the American Society for Photogrammetry and Remote Sensing (ASPRS Foundation 2012). During this process, special emphasis was placed on the classification of the "ground" class so that it would act as a common reference point for later collection of LiDAR and photogrammetric data. Additionally, it is crucial to achieve a correct DTM to obtain an accurate CHM.

Radiometric classification takes advantage of the RGB values of the photogrammetric point cloud. This step was carried out using in-house "Vegetation classification by radiometry" software. The analysis is based on the percentage differences between the digital levels of two channel pairs (R-G and R-B). Points were classified automatically according to a threshold defined by the difference from a green reference value. However, the values of green hues depend on many factors, such as the sensor employed, the conditions and date of flight, the type of species, the phenological state of the vegetation, etc. Accordingly, it is necessary to establish a threshold value from vegetation samples in the photogrammetric model.

Once the LiDAR information was corrected and the photogrammetric point cloud had been classified and refined, the point clouds were fused as described in the following section.

Fusion of point clouds

Before registering the point clouds, the ground photogrammetric points were filtered by cross-analysis with the LiDAR data to address errors caused in the classification process. To do so, we obtained a map of altimetric differences in ground-class zones shared between the two clouds. The photogrammetric points with large differences in height were reclassified as vegetation. We then generated a mask of the ground-class photogrammetric points to remove clusters of isolated points ($S < 2$ m^2) and the points contained within polygons with a high mean altimetric difference ($h > 1$ m). This filtering process allowed us to refine the terrain's photogrammetric data. Figure 4 shows the process used.

Low-cost photogrammetry includes georeferencing errors produced by the use of inertial sensors and low-accuracy GNSS and non-metric cameras. Accordingly, we designed a *correction model* to integrate the collected LiDAR data into the refined photogrammetric cloud, achieving a registration accuracy that was statistically compatible with the accuracy of both techniques. To

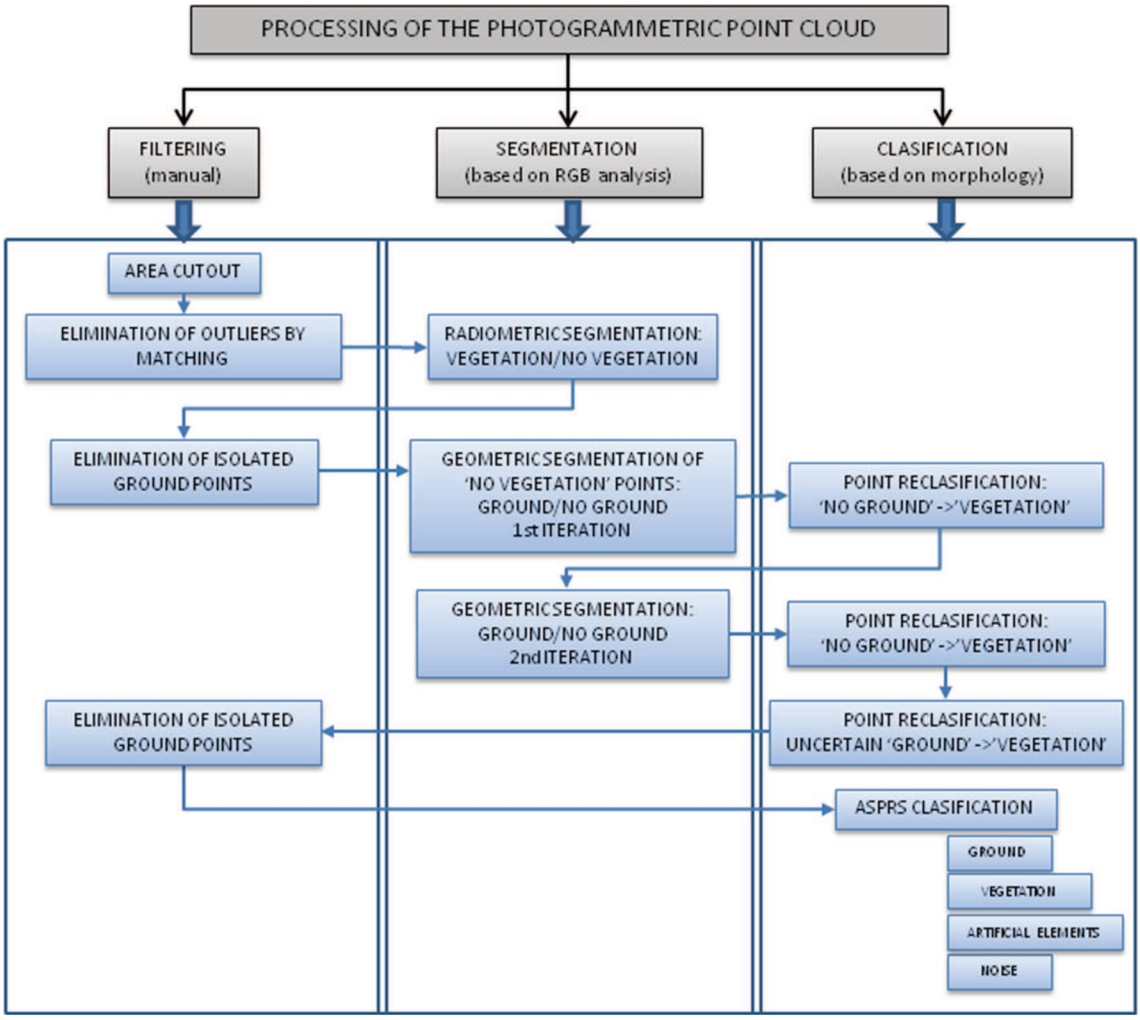

Fig. 3 Workflow for the processing and classification of the photogrammetric point cloud

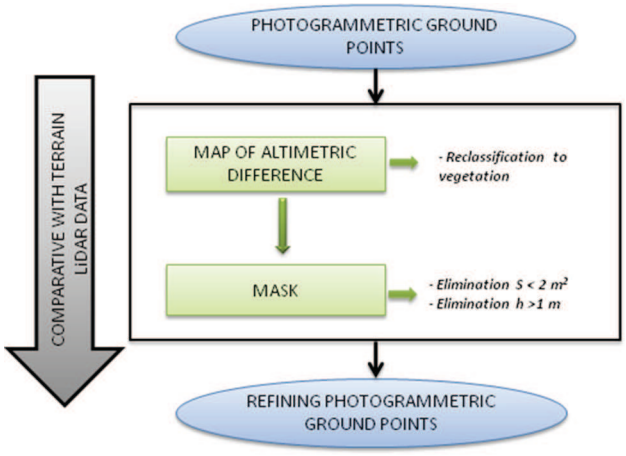

Fig. 4 Refining of the photogrammetric ground points through LiDAR data

analyse this compatibility, the 'a priori' (σ) and 'a posteriori' ($\hat{\sigma}$) altimetric accuracies were compared. This model was derived from the altimetric differences in the terrain between both datasets. To reject outliers from the corrected model, we eliminated the points whose altimetric difference fell outside the 95 % confidence interval (St-Onge et al. 2008).

DTM, DSM and CHM generation

After the registration of both datasets, the different digital models relating to terrain (DTM), surface (DSM) and canopy (CHM) were obtained by surface generation in the form of triangular meshes from the resulting classified cloud. These meshes had to be filtered and refined to remove the errors generated during the automated process.

This step used the approximation of Attene (2010), which incorporates several automated and sequential tasks:

- Filling of holes through algorithms of planar triangulations (Barequet and Sharir 1995) or more complex approaches based on interpolation of the radial basis function (Branch et al. 2006), the minimum distance (Dolenc and Makela 1993) and the measurement of angles (Bøhn and Wozny 1992; Varnuška et al. 2005).
- Repair of meshing gaps, based on minimum threshold distance algorithms (Rock and Wozny 1992; Barequet and Kumar 1997).
- Removal of topological noise, allowing the mesh to be re-triangulated locally (Guskov and Wood 2001).
- Removal of geometric noise by algorithms that apply filters as anti-aliased Laplacians in general or specific zones (Fan et al. 2008).

Finally, the CHM was obtained from the difference between the photogrammetrical DSM and the DTM resulting from the fusion of the point clouds (Järnstedt et al. 2012). The CHM represents the normalised heights of the vegetation with respect to the surface of the terrain, with a planimetric resolution of 1 m (D'Oliveira et al. 2012).

Experimental results

This study was conducted in an area of public land in the municipality of Bienservida in the province of Albacete (Spain). In particular, the study zone is located on land identified in the Public Usefulness Catalogue as No. 26. Figure 5a shows a map with the location of the study zone outlined in white. The scrubland area covers 1100 Ha. This is of great interest from a forestry perspective because the densely forested zone hosts a forest mass composed of *Pinus nigra* with different fractions of coverage according to the National Forest Inventory of Spain. The area also has a steep topography, and thus photogrammetric surveys are more appropriate from a practical point of view than classic forestry methods. The choice of this zone was also based on the availability of a pre-existing work plan that included the selected land and incorporated a classic forestry inventory. Thus, we established a zone of 2.00 km^2 (Fig. 5b) as the study area where we could apply the proposed methodology.

Regarding the LiDAR dataset, despite its official source, it was necessary to validate the data in advance by visual checking and manual refining. As a result, some outliers such as 'vegetation' or 'noise' were classified as 'ground', whereas some buildings were classified as 'vegetation'. To contrast changes in the LiDAR cloud with the initial classification, a confusion matrix was developed. A total of 4,822,511 points were classified correctly, obtaining a global accuracy of 99.98 %. An analysis of the confusion matrix, including the errors of commission and omission as well as producer and user accuracy can be seen in Table 3. These results show the insignificance of the incorrectly classified points in relation to the entirety of the cloud. A 1 % error was only exceeded by the 'others' class due to the presence of incorrect ground and vegetation points.

To perform photogrammetric data acquisition, the flight over the study area was planned with a height of 300 m, corresponding to a 7.50-cm GSD. The camera shooting interval was configured according to the minimum forward overlap and flight speed to meet the flight planning requirements and avoid image blurring, respectively (see "Flight planning and execution" section for more details). The obtained flight plan is outlined in Fig. 6, in which the rectangles represent the footprint of each image (area covered on the ground) resulting from each camera position (circles) along the flight strips. These footprints were

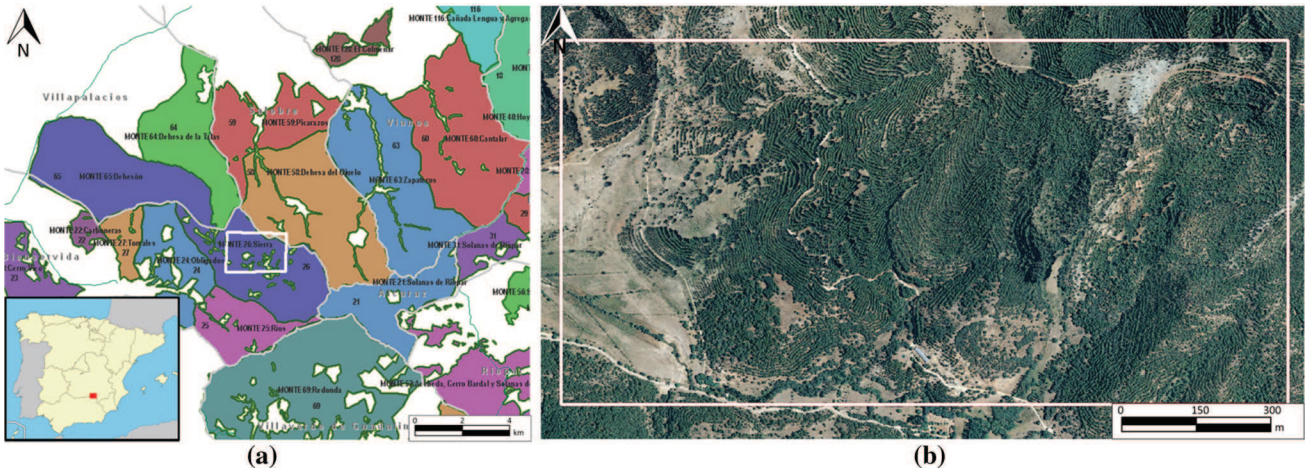

Fig. 5 **a** Location map with a box around the study area (*white rectangle*) and **b** orthophoto of the study area (EPSG code 25830)

Table 3 (a) Confusion matrix from the LiDAR data considering 'ground' and 'vegetation' classes and (b) errors of commission and omission and user and producer accuracy

	Refined LiDAR Data			
	Vegetation	Ground	Others	
(a)				
Initial LiDAR data				
Vegetation	3,674,535	0	325	3,674,860
Ground	517	1,145,807	20	1,146,344
Others	0	0	2169	2169
	3,675,052	1,145,807	2514	4,823,373
	Commission %	Omission %	Producer accuracy	User accuracy
(b)				
Vegetation	0.009	0.014	99.991	99.986
Ground	0.047	0.000	99.953	100.000
Others	0.000	13.723	100.000	86.277
	Global accuracy: 99.982 %			

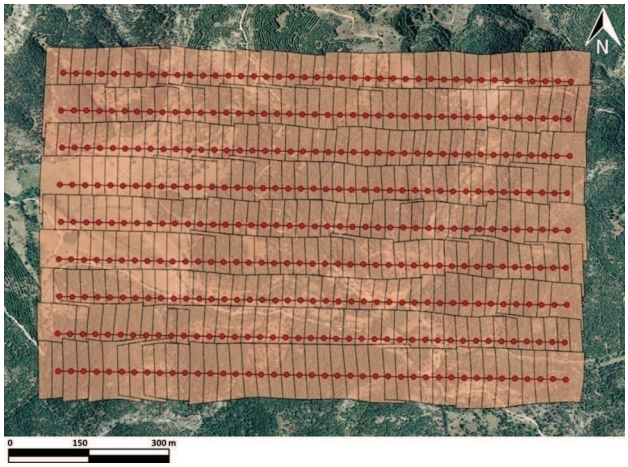

Fig. 6 Flight planning, 0.08 m GSD: *rectangles* represent the footprint of each image, and circles are the camera positions along the flight strips (EPSG code 25830)

projected based on the DTM ground relief to verify compliance with the flight parameter requirements.

The flight was carried out on 5 December 2013, covering a greater area than proposed to ensure total coverage of the study area. The flight run followed the established plan. Finally, images were georeferenced according to ETRS89 UTM 30 North (Coordinate Reference System, CRS EPSG code 25830), which is required by Spanish legislation for all geomatic products. The Albacete station was taken as a reference from the ERGNSS network (network of permanent geodetic GNSS stations of the National Geographic Institute of Spain) and used to correct the position of the RTK solution. In the navigation phase, which used a GNSS, WGS84 CRS was employed (EPSG code 4326). This georeferencing served as a preliminary photogrammetric adjustment and helped the process of computational matching.

Before the flight, 29 artificial ground points were placed in the zone to be measured by GNSS; these acted as control and check points. A georeferencing precision of 0.05 m was obtained in GNSS measurement post-processing.

In the conventional photogrammetric processing method carried out according to "Low-cost photogrammetric workflow" section, a total of 12,732,877 matching points were obtained, detecting 2,399,164 outliers through a robust estimation of the fundamental matrix (Barazzetti et al. 2010). The generated 3D dense model (Fig. 7) was composed of 290 million points after the processing of 1001 images, which is a density of 145 points/m^2. The model was georeferenced using 17 ground control points, obtaining an absolute georeferencing error of 1.21 m from the check points.

Once the photogrammetric point cloud had been generated, it was necessary to classify the points according to two classes: ground and vegetation. To distinguish the vegetation, radiometric segmentation was carried out, taking advantage of the visible spectrum of the photogrammetric point cloud. Figure 8 shows an example of the results of this processing.

Next, geometric segmentation was performed, working with the non-vegetation class, which was re-labelled 'ground'. The resulting photogrammetric point cloud classification is outlined in Table 4.

To analyse the statistical compatibility of both data sources (LiDAR and photogrammetry), the accuracies of both sets of registrations were compared. The 'a priori' accuracy was $\sigma = 0.41$ m (Eq. 2) while the 'a posteriori' accuracy obtained was $\hat{\sigma} = 0.47$ m, being the mean altimetric accuracy 0.17 m, confirming the validity of the results. These values were acquired in areas sharing common ground points between the LiDAR and refined photogrammetric point clouds, thus generating an altimetric difference map.

$$\sigma_{\text{fusion}} = \sqrt{(\sigma^2_{\text{photogrammetry}} + \sigma^2_{\text{LiDAR}})}$$

$$\sigma_{\text{fusion}} = \sqrt{(0.10^2 + 0.40^2)} = 0.41\,\text{m} \quad (2)$$

On the map of altimetric differences, we removed the values that fell outside a 95 % confidence interval, and the remaining differences were interpolated to obtain values at points lacking photogrammetric terrain data. Figure 9 shows a Q–Q plot of the map's height differences compared with standard normal quantiles, demonstrating a non-Gaussian distribution of the errors (absence of

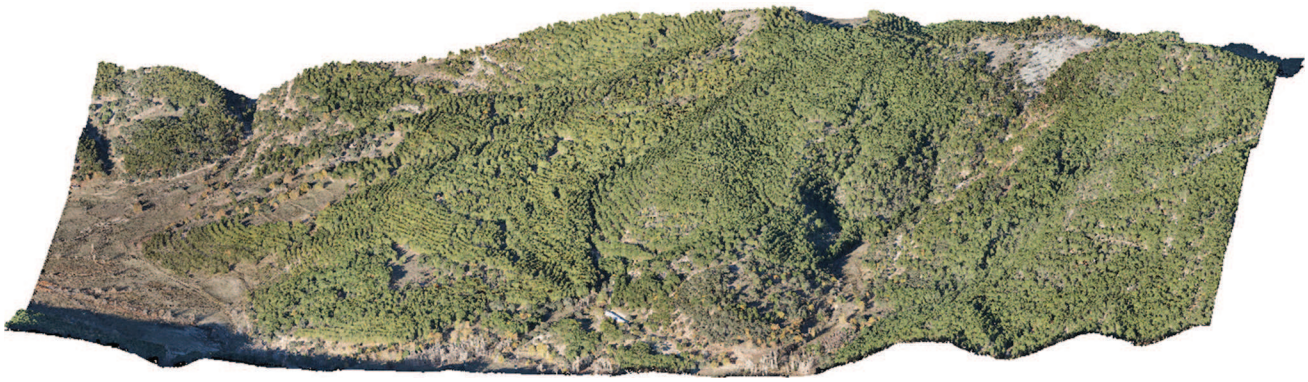

Fig. 7 Photogrammetric dense point cloud of the study area (145 points/m^2)

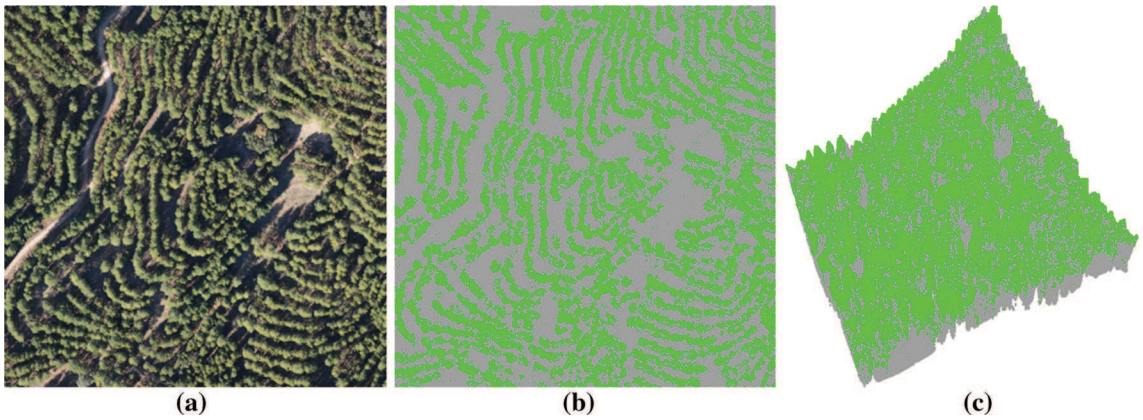

Fig. 8 Examples of radiometric segmentation of the photogrammetric point cloud. **a** Photogrammetric point cloud, **b** classified vegetation (*green*), **c** 3D classification view

Table 4 Classification of the photogrammetric cloud

Classification	No. points	%
Ground	29,281,752	17.70
Vegetation	135,562,812	81.92
Noise	528,961	0.32
Building	86,378	0.05
Wire conductor	12,668	0.01
Tower	2479	0.00

systematism), with some values that exceed the estimated accuracy. This is because the georeferencing of the LiDAR and photogrammetric data was not very rigorous owing to the scant topographic support of the LiDAR data, the automated matching processes, the use of low-accuracy inertial sensors and GNSS, and the use of non-metric cameras for the low-cost photogrammetry. Owing to this distribution, upon applying a solid-rigid transformation whose principal component is translation on the z axis, the error committed at certain points would be increased. Table 5 shows the map's statistical parameters and values.

In light of the above, we designed a discrete *correction model* (section "Fusion of point clouds") that improved the accuracy of the registration based on the altimetric differences map. The model was applied to LiDAR terrain data at points lacking photogrammetric information by means of a computer application designed for this end, as shown in Fig. 10. These corrected points were included in the photogrammetric point cloud, thus obtaining the fused point cloud.

Once both datasets had been fused, the properties of the final point cloud were analysed, checking for the absence of vegetation points with negative height. Table 6 shows the number of points belonging to each class together with the range of elevations and height normalised with respect to the ground class. Figure 11 shows the final point cloud for vegetation, ground and building classifications, seen in plan view.

As final results, Figs. 12, 13 and 14 show the Digital Terrain, Surface and Canopy Models obtained from the hybrid cloud, rasterised with a mesh size of 1 m.

After analysis of the CHM, we observed that there were very few cases in which the vegetation surpassed a height of 20 m. The *P. nigra* specimens in the zone were between 20 and 23 m in height. There was one case in which a

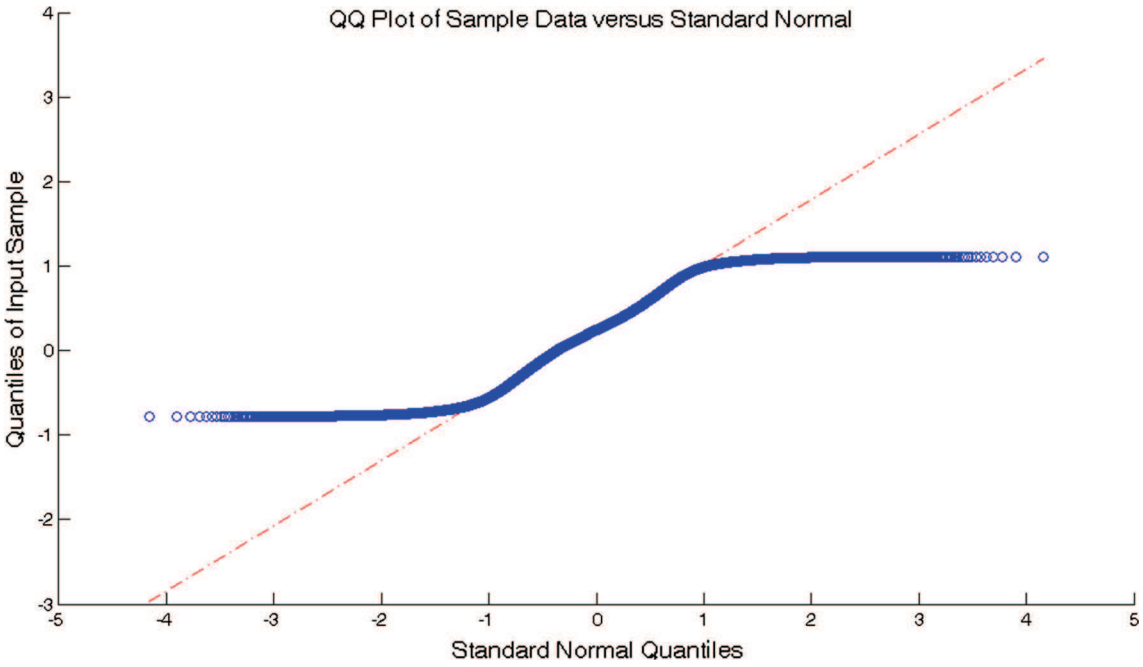

Fig. 9 Q–Q plot of the altimetric difference map versus standard normal quantiles

Table 5 Statistical data of the altimetric differences map

Maximum (m)	1.090
Mean (m)	0.226
Minimum (m)	−0.760
Std. deviation (m)	0.364

height of 27.7 m was attained, but this specimen was not a pine and was deciduous; it was probably a poplar, whose heights can reach 35 m.

The results allowed us to explore the development of forest growth in the area. To accomplish this, we analysed

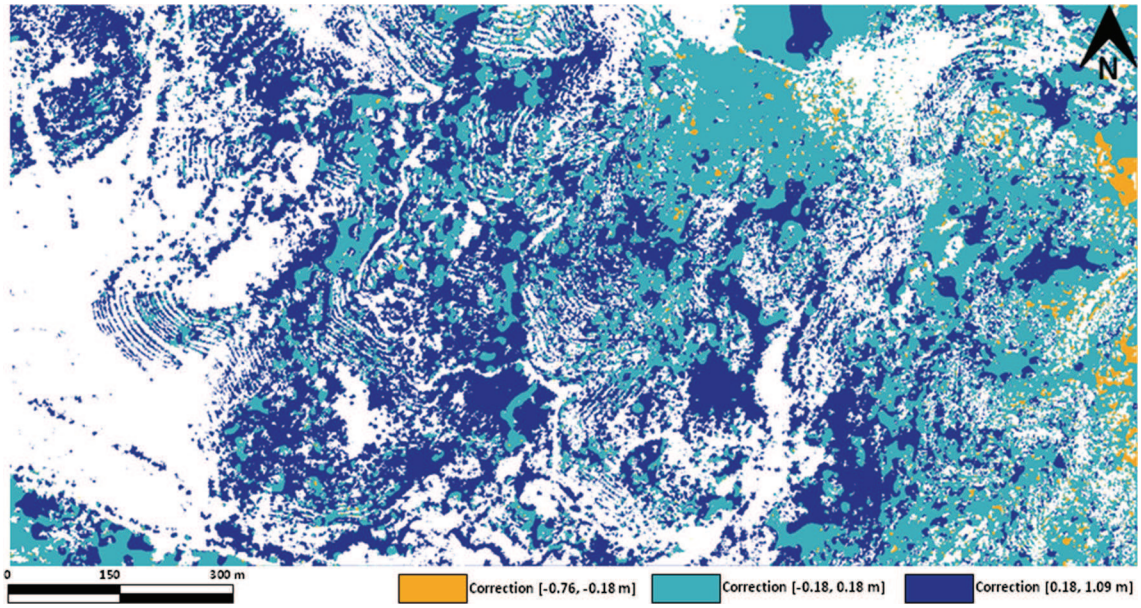

Fig. 10 Correction model coded by colour (EPSG code 25830)

Table 6 Classification of the final fusion cloud

Classification	No. points	%	Z_Min (m)	Z_Max (m)	Height (m)
Ground	29,220,875	17.78	1111.24	1406.59	0
Low vegetation	22,638,874	13.78	1111.50	1407.50	(0–1]
Medium vegetation	17,920,617	10.91	1112.68	1409.46	[1–3]
High vegetation	93,514,449	56.93	1113.50	1412.49	[3–27.67]
Building	86,378	0.05	1119.99	1184.34	–
Others	911,914	0.55	–	–	–

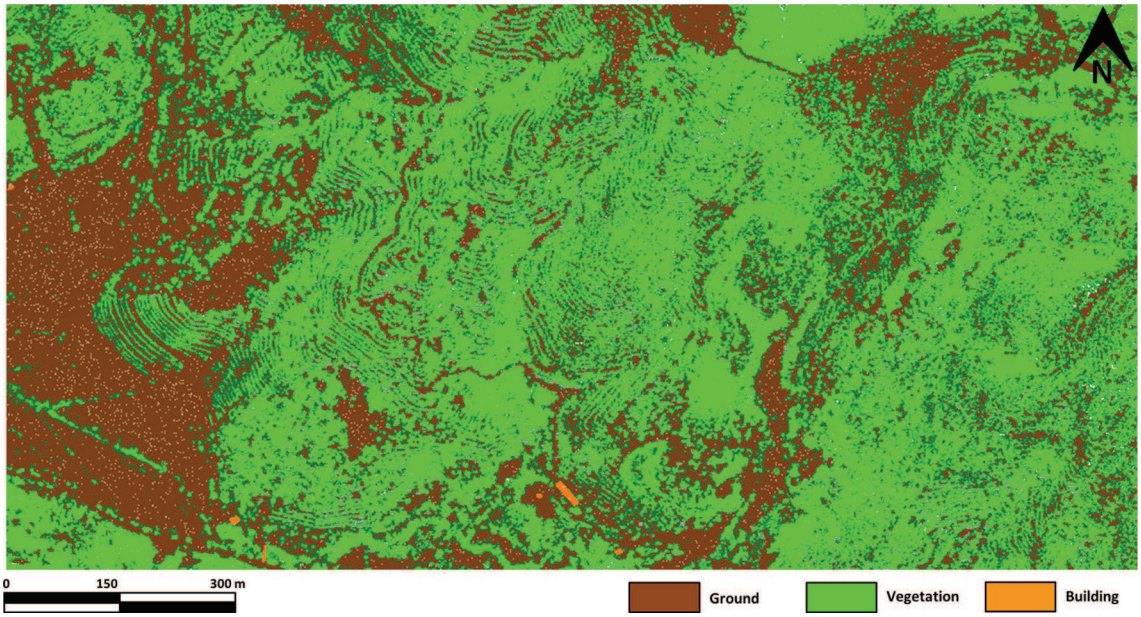

Fig. 11 Plan view of the final classified fusion cloud

Fig. 12 Digital terrain model

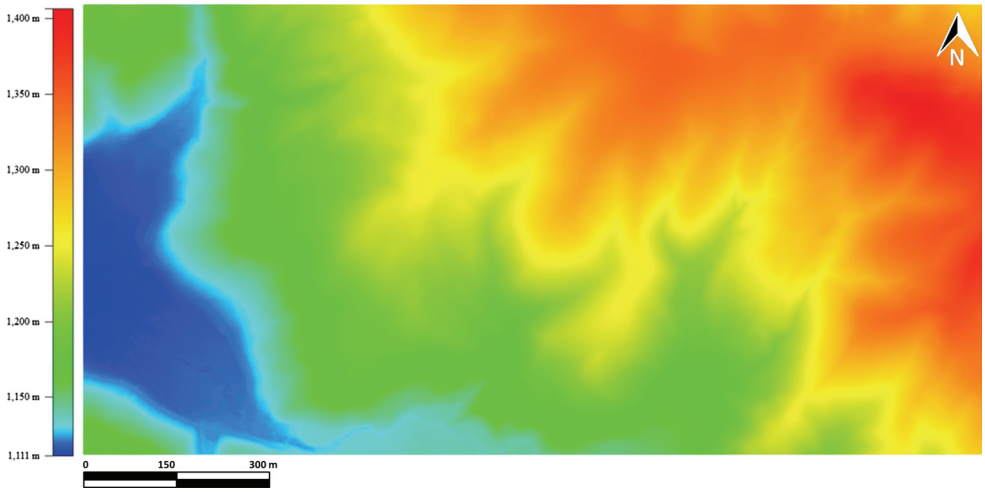

the distribution of the differences in plant volume between the CHM from the LiDAR data taken in 2009 and that generated from the hybrid point cloud in late 2013, both with respect to their respective DTMs. The increase in biomass volume that occurred during the interim was 3,318,501 m^3 in the 2.00 km^2 study area. This was due to the protectionist legislation enacted in the zone during those years (Cerro and Borja 2007).

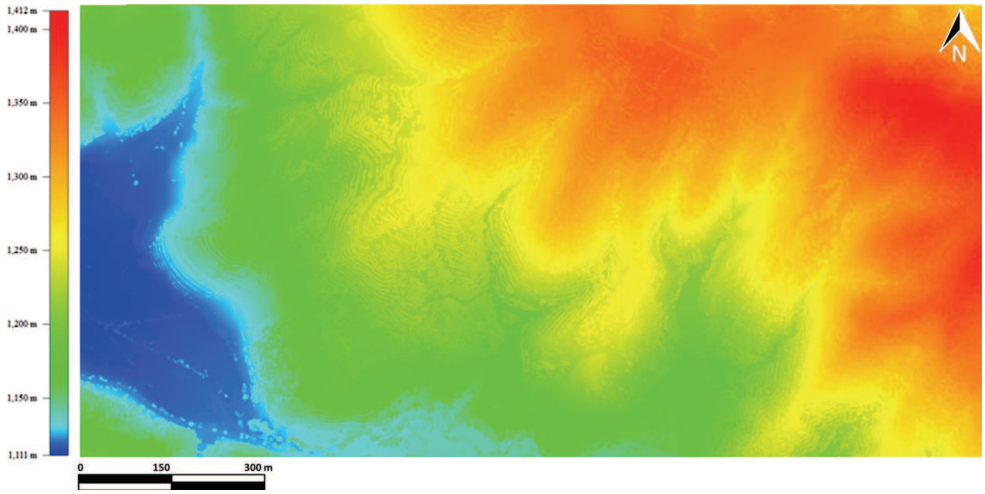

Fig. 13 Digital surface model

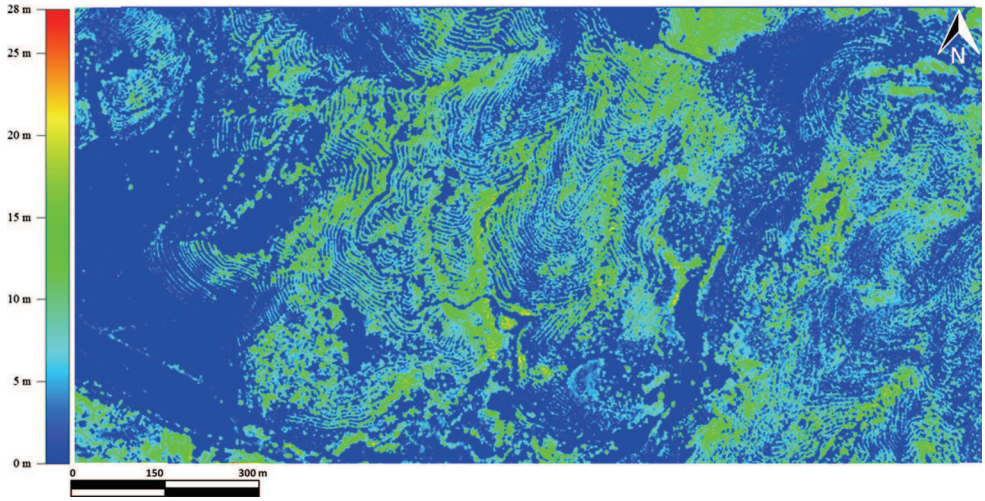

Fig. 14 Canopy height model

Conclusions

This paper describes a successful methodology that generates a Canopy Height Model for conducting forest inventories such a stratification of forest masses to forest management unit applications or a stock calculation and for fire studies obtaining combustible models. This CHM permits a better understanding of the forest structure in detail, allowing to know the relationships between the flora, the fauna and the soil over large extensions. The combined use of low-cost photogrammetry based on the use of economical, conventional, non-metric digital cameras and aerial LiDAR open data, together with the use of the latest computational vision techniques and geomatic tools, provides useful information for forestry applications.

In particular, by integrating the terrain data in the photogrammetric cloud, it is possible to incorporate LiDAR's capacity for terrain detection in zones of dense vegetation with the greater spatial, radiometric and temporal resolution of low-cost photogrammetry from alternative platforms such as the aerial trike or RPAS. Moreover, these platforms allow the loading of sensors suitable for vegetation analysis, depending on their payload capacity. Thus, it is possible to carry out a radiometric classification of the vegetation that improves upon current morphological methods. In this sense, we define a correction model that allows LiDAR data to be adjusted to the photogrammetric point cloud, obtaining an altimetric accuracy of 0.47 m for the registration data.

The advantage offered by this methodology is that it allows a CHM to be obtained with adequate phenological detail due to the combination of LiDAR flights performed at low temporal resolution and low-cost photogrammetric flights performed with the required periodicity. This also allows a reduction in the errors that arise in dasometric assessments upon incorporating models for the prediction of vegetation growth.

It is worth noting that the statistical compatibility of both sources of data could be improved in the data acquisition phase with appropriate field topographic support.

That is, photogrammetric point cloud georeferencing can be improved by designing pre-signalling targets of suitable colour for forestry applications and for later measurement in the images collected. It might even be possible to improve the targets' design to facilitate their detection and the automated extraction of the centroid. Another proposal would involve the incorporation of metric cameras, although in the case of RPAS this depends on the platform's payload capacity. This would increase both the associated cost and the accuracy.

The proposed methodology reduces the time required for acquisition and processing compared with that of traditional techniques of forest inventorying, with the added advantage that it provides vectorial information in the form of classified point clouds. This implies an increase in final accuracy at the rodal level and simplified integration and management of forestry information in Geographic Information Systems. At the same time, the subjectivity associated with operator-generated uncertainty is removed. Needless to say that the complementary of both techniques would offer to reach better results, taking advantages of the spatial continuity of the remote sensing in order to extrapolate the manual measurements of the trees.

In future work, we shall address the forestry variables in the obtained dense cloud and perform a comparative study with the variables obtained from the LiDAR information, applying rodal, individual-tree or even a combination of both methods to benefit from the high resolution of the initial data. To date, from the obtained CHM, essential tree parameters such as diameter at breast height (DBH) or distinguishing between species are not reliably derived yet. Another line of enquiry will be to contrast the variables obtained from the dense cloud with other data from a classic inventory of the study zone, i.e., the National Forest Inventory of Spain and the inventory drafted by the Public Land and Natural Spaces Service of the Agricultural Commission of the Regional Government of Castilla-La Mancha, Spain.

Author contribution statement B.F.-G., D.H.-L. and D.G.-A. planned the experiment and supervised processing, M.H.-H., B.F.-G. and S.B.-L. performed the study, analysed data and prepared the manuscript and P.R.-G. contributed to data interpretation. All authors wrote the manuscript.

Acknowledgments This research arose as a pilot project in collaboration with the Public Land and Natural Spaces Service, belonging to the Peripheral Services of the Agricultural Commission of the Regional Government of Castilla-La Mancha; the Institute for Development of the University of Castilla-La Mancha; the Forestry and Natural Spaces Service; the Agriculture, Environment and Rural Development Department of the Castilla-La Mancha Regional Government; and the USAL research group Geomatic Technologies for the 3D digitalisation and modelling of complex objects (TIDOP).

Compliance with ethical standards

Conflict of interest The authors declare that they have no conflict of interest.

References

ASPRS Foundation (2012) LASer (LAS) file format exchange activities. http://www.asprs.org/Committee-General/LASer-LAS-File-Format-Exchange-Activities.html. Accessed 01 Nov 2014

Attene M (2010) A lightweight approach to repairing digitized polygon meshes. Vis Comput 26(11):1393–1406

Axelsson P (1999) Processing of laser scanner data—algorithms and applications. ISPRS J Photogramm Remote Sens 54(2):138–147

Barazzetti L, Remondino F, Scaioni M, Brumana R (2010) Fully automatic UAV image-based sensor orientation. In: Proceedings of the 2010 Canadian geomatics conference and symposium of commission I

Barequet G, Kumar S (1997) Repairing CAD models. In: Visualization'97, proceedings, pp 363–370. IEEE

Barequet G, Sharir M (1995) Filling gaps in the boundary of a polyhedron. Comput Aided Geom Des 12(2):207–229

Benko M, Balenovic I (2011) Past, present and future of application of remote sensing methods in croatian forest inventory. Sumarski List 135:272–281

Bohlin J, Wallerman J, Fransson JES (2012) Forest variable estimation using photogrammetric matching of digital aerial images in combination with a high-resolution DEM. Scand J For Res 27(7):692–699

Bøhn JH, Wozny MJ (1992) Automatic CAD-model repair: shell-closure. In: Proceedings of symposium on solid freeform fabrication, pp 86–94

Branch D, Dang LC, Hall N, Ketchum W, Melakayil M, Parrent J, Baron E (2006) Comparative direct analysis of type Ia supernova spectra. II. Maximum light. Publ Astron Soc Pac 118(842):560–571

Cerro A, Borja MEL (2007) El "Pinus nigra arn." en la Serranía de Cuenca: estudio sobre su regeneración natural y bases para su gestión. Junta de Comunidades de Castilla-La Mancha, Dirección General del Medio Ambiente

Chauve A, Mallet C, Bretar F, Durrieu S, Deseilligny MP, Puech W (2007) Processing full-waveform lidar data: modelling raw signals. In: International archives of photogrammetry, remote sensing and spatial information sciences, pp 102–107

CNIG (National Center of Geographic Information in Spain) (2009) Technical specifications for the National Plan of Aerial Orthophotography (PNOA). ftp://pnoa.ign.es. Accessed 01 Nov 2014

CNIG (National Center of Geographic Information in Spain) (2015). http://centrodedescargas.cnig.es/CentroDescargas/. Accessed 16 July 2015

Dolenc A, Makela I (1993) Some efficient procedures for correcting triangulated models. In: Proceedings of solid freeform fabrication symposium, pp 126–134

D'Oliveira MV, Reutebuch SE, McGaughey RJ, Andersen HE (2012) Estimating forest biomass and identifying low-intensity logging areas using airborne scanning lidar in Antimary State Forest, Acre State, Western Brazilian Amazon. Remote Sens Environ 124:479–491

Eid T, Gobakken T, Naesset E (2004) Comparing stand inventories for large areas based on photo-interpretation and laser scanning by means of cost-plus-loss analyses. Scand J For Res 19(6):512–523

Estornell J, Ruiz LA, Velazquez-Marti B, Hermosilla T (2012) Assessment of factors affecting shrub volume estimations using airborne discrete-return LiDAR data in Mediterranean areas. J Appl Remote Sens 6(1):063544

Fan YZ, Tam BS, Zhou J (2008) Maximizing spectral radius of unoriented Laplacian matrix over bicyclic graphs of a given order. Linear Multilinear Algebra 56(4):381–397

Gleason CJ, Im J (2012) Forest biomass estimation from airborne LiDAR data using machine learning approaches. Remote Sens Environ 125:80–91

Gonzalez E, Dieguez U, Miranda D (2012) Estimation of stand variables in Pinus radiata D. Don plantations using different LiDAR pulse densities. Forestry 85(2):281–292

González-Aguilera D, Guerrero D, Hernández-López D, Rodríguez-Gonzálvez P, Pierrot M, Fernández-Hernández J (2013) PW, photogrammetry workbench

González-Ferreiro E, Diéguez-Aranda U, Crecente-Campo F, Barreiro-Fernández L, Miranda D, Castedo-Dorado F (2014) Modelling canopy fuel variables for Pinus radiata D. Don in NW Spain with low-density LiDAR data. Int J Wildl Fire 23(3):350–362

Gupta S, Weinacker H, Koch B (2010) Comparative analysis of clustering-based approaches for 3-D single tree detection using airborne fullwave lidar data. Remote Sens 2(4):968–989

Guskov I, Wood ZJ (2001) Topological noise removal. In: 2001 graphics interface proceedings, Ottawa, Canada, 19

Hernández-Lopez D, Felipe B, González D, Arias B (2013) An automatic approach to UAV flight planning and control for photogrammetric applications: a test case in the Asturias Region (Spain). Photogramm Eng Remote Sens 79(1):87–98

Hyyppä J, Hyyppä H, Leckie D, Gougeon F, Yu X, Maltamo M (2008) Review of methods of small-footprint airborne laser scanning for extracting forest inventory data in boreal forests. Int J Remote Sens 29(5):1339–1366

IGN (2015) http://pnoa.ign.es/presentacion. Accessed 16 July 2015

Jaakkola A, Hyyppä J, Kukko A, Yu X, Kaartinen H, Lehtomäki M, Lin Y (2010) A low-cost multi-sensoral mobile mapping system and its feasibility for tree measurements. ISPRS J Photogramm Remote Sens 65:514–522

Järnstedt J, Pekkarinen A, Tuominen S, Ginzler C, Holopainen M, Viitala R (2012) Forest variable estimation using a high-resolution digital surface model. ISPRS J Photogramm Remote Sens 74:78–84

Kankare V, Vastaranta M, Holopainen M, Räty M, Yu X, Hyyppä J, Viitala R (2013) Retrieval of forest aboveground biomass and stem volume with airborne scanning LiDAR. Remote Sens 5(5):2257–2274

Kohavi R, Provost F (1998) Glossary of terms. Mach Learn 30(2–3):271–274

Kraus K (2007) Photogrammetry, 2007. Geometry from images and laser scans. Walter de Gruyter

Lim KS, Treitz PM (2004) Estimation of above ground forest biomass from airborne discrete return laser scanner data using canopy-based quantile estimators. Scand J For Res 19(6):558–570

Lisein J, Pierrot M, Bonnet S, Lejeune P (2013) A photogrammetric workflow for the creation of a forest canopy height model from small unmanned aerial system imagery. Forests 4(4):922–944

Lowe DG (2004) Distinctive image features from scale-invariant keypoints. Int J Comput Vis 60:91–110

Magnussen S, Boudewyn P, Wulder MA, Seemann D (2000) Predictions of forest inventory cover type proportions using landsat TM. Silva Fennica 34(4):351–370

Magnussen S, Naesset E, Wulder MA (2007) Efficient multiresolution spatial predictions for large data arrays. Remote Sens Environ 109(4):451–463

Magnusson M, Fransson JES, Olsson H (2007) Aerial photo-interpretation using Z/I DMC images for estimation of forest variables. Scand J For Res 22(3):254–266

Mallet C, Bretar F (2009) Full-waveform topographic lidar: state-of-the-art. ISPRS J Photogramm Remote Sens 64(1):1–16

Means JE, Acker SA, Fitt BJ, Renslow M, Emerson L, Hendrix CJ (2000) Predicting forest stand characteristics with airborne scanning lidar. Photogramm Eng Remote Sens 66(11):1367–1372

Mora B, Wulder MA, Hobart GW, White JC, Bater CW, Gougeon FA, Coops NC (2013) Forest inventory stand height estimates from very high spatial resolution satellite imagery calibrated with lidar plots. Int J Remote Sens 34(12):4406–4424

Naesset E (1997) Estimating timber volume of forest stands using airborne laser scanner data. Remote Sens Environ 61(2):246–253

Naesset E (2004) Practical large-scale forest stand inventory using a small-footprint airborne scanning laser. Scand J For Res 19(2):164–179

Naesset E, Bollandsas OM, Gobakken T (2005) Comparing regression methods in estimation of biophysical properties of forest stands from two different inventories using laser scanner data. Remote Sens Environ 94(4):541–553

Navarro-Cerrillo RM, del Campo AD, Ceacero CJ, Quero JL, Hermoso de Mena J (2014) On the importance of topography, site quality, stock quality and planting date in a semiarid plantation: feasibility of using low-density LiDAR. Ecol Eng 67:25–38

NavCen (2008) Global positioning system standard positioning service performance standar, 4th edn. US Department of Defense: Position, Navigation and Timing Executive Committee, Washington

Nelson R, Krabill W, Tonelli J (1988) Estimating forest biomass and volume using airborne laser data. Remote Sens Environ 24(2):247–267

Nelson R, Oderwald R, Gregoire TG (1997) Separating the ground and airborne laser sampling phases to estimate tropical forest basal area, volume, and biomass. Remote Sens Environ 60(3):311–326

Nelson R, Parker G, Hom M (2003) A portable airborne laser system for forest inventory. Photogramm Eng Remote Sens 69(3):267–273

Ortega-Terol D, Moreno MA, Hernández-López D, Rodríguez-Gonzálvez P (2014) Survey and classification of large woody debris (LWD) in streams using generated low-cost geomatic products. Remote Sens 6:11770–11790

Pierrot-Deseilligny M, Clery I (2011) An open source bundle adjustment software for automatic calibration and orientation of set of images. In: Apero, ISPRS symposium, 3DARCH11, Trento, Italy, March 2–4, pp 269–276

Popescu SC, Wynne RH, Nelson RF (2002) Estimating plot-level tree heights with lidar: local filtering with a canopy-height based variable window size. Comput Electron Agric 37(1):71–95

Premerlani W, Bizard P (2014) Direction cosine matrix IMU: theory. http://gentlenav.googlecode.com/files/DCMDraft2.pdf. Accessed 20 Dec 2014

Richardson JJ, Moskal LM (2011) Strengths and limitations of assessing forest density and spatial configuration with aerial LiDAR. Remote Sens Environ 115(10):2640–2651

Rock SJ, Wozny MJ (1992) Generating topological information from a bucket of facets. In: Solid freeform fabrication symposium proceedings, pp 251–259. The University of Texas at Austin, Austin

St-Onge B, Vega C, Fournier RA, Hu Y (2008) Mapping canopy height using a combination of digital stereo-photogrammetry and lidar. Int J Remote Sens 29(11):3343–3364

Takasu T (2009) RTKLIB: open source program package for RTK-GPS. FOSS4G, Tokyo, Japan

Tao W, Lei Y, Mooney P (2011) Dense point cloud extraction from UAV captured images in forest area. In: Proceedings of the 2011 IEEE international conference on spatial data mining and geographical knowledge services (ICSDM), pp 389–392

Varnuška M, Parus J, Kolingerová I (2005) Simple holes triangulation in surface reconstruction. In: Proceedings of ALGORITMY, pp 280–289

Wallace L, Lucieer A, Watson C, Turner D (2012) Development of a UAV-LiDAR system with application to forest inventory. Remote Sens 4:1519–1543

Wang Z, Boesch R, Ginzler C (2007) Color and lidar data fusion: application to automatic forest boundary delineation in aerial images. Int Arch Photogramm Remote Sens Spat Inf Sci [CD] 36(1):W51

Weinacker H, Koch B, Heyder U, Weinacker R (2004) Development of filtering, segmentation and modelling modules for lidar and multispectral data as a fundament of an automatic forest inventory system. Int Arch Photogramm Remote Sens Spat Inf Sci 36(Part 8):50–55

White JC, Wulder MA, Varhola A, Vastaranta M, Coops NC, Cook BD, Woods M (2013a) A best practices guide for generating forest inventory attributes from airborne laser scanning data using an area-based approach. For Chron 89(6):722–723

White JC, Wulder MA, Vastaranta M, Coops NC, Pitt D, Woods M (2013b) The utility of image-based point clouds for forest inventory: a comparison with airborne laser scanning. Forests 4(3):518–536

Willers JL, Wu J, O'Hara C, Jenkins JN (2012) A categorical, improper probability method for combining NDVI and LiDAR elevation information for potential cotton precision agricultural applications. Comput Electron Agric 82:15–22

Wulder MA, White JC, Fournier RA, Luther JE, Magnussen S (2008a) Spatially explicit large area biomass estimation: three approaches using forest inventory and remotely sensed imagery in a GIS. Sensors 8(1):529–560

Wulder MA, White JC, Hay GJ, Castilla G (2008b) Towards automated segmentation of forest inventory polygons on high spatial resolution satellite imagery. For Chron 84(2):221–230

Wulder MA, White JC, Nelson RF, Næsset E, Ørka HO, Coops NC, Gobakken T (2012) Lidar sampling for large-area forest characterization: a review. Remote Sens Environ 121:196–209

Wulder MA, Coops NC, Hudak AT, Morsdorf F, Nelson R, Newnham G, Vastaranta M (2013) Status and prospects for LiDAR remote sensing of forested ecosystems. Can J Remote Sens 39(-sup1):S1–S5

IV. Conclusions and Future Works

4. CONCLUSIONS AND FUTURE WORKS

In this Doctoral Thesis, contributions in the research lines are made which advance in the direction of the application of low cost and close-range photogrammetry to Agroforestry Engineering. This is a non-destructive and non-invasive technique suitable to inspect and monitor crops and forest land, through an optimal modeling of biophysical parameters and extracting georeferenced information with metric rigor.

This Doctoral Thesis is the result of a compendium of three scientific papers published in specialized index journals. Below, a summary of the contributions including most relevant results and the directions for future works related to the articles, are discussed.

The **first paper** describes a successful methodology for radiometric calibration using the vicarious method of a multispectral MiniMCA camera aboard a low-cost manned aerial platform and using low-cost targets of invariant reflectivity material. The potential of this PPG trike system is evident, with the possibility of being able to load it with a large number of sensors that extend multispectral studies, affording the advantage of a flying height that minimizes the need for atmospheric corrections. The results confirm a new trend for low-cost remote sensing, together with the use of the latest computer vision techniques and open-source geomatic tools. In this study case, the calibrated geomatic products can be used to successfully evaluate and classify large areas of different crops, allowing decisions to be made about irrigation, nutritional support and crop development through accurate georeferenced and calibrated multispectral images. Here, the potential of deriving quantitative magnitudes such as vegetation indices is also shown. Future works will address the assimilation of the calibrated images into agronomic models to evaluate their consistency with advanced biophysical variables.

In the **second paper**, a non-invasive low-cost method with application to precision viticulture is presented that consists of vineyard yield estimation. The method is fast, reliable, robust and objective, and could serve to take decisions in advance regarding actions to be taken in vineyards, predicting the results and planning the vintage optimally.

The method developed relies on the adaptation of the PW software tool, which allows the metric reconstruction and dimensional analysis of bunches from grapevine images taken in field conditions. The advantages of PW include process automation, sufficient quality to generate dense resolution models equivalent to the pixel size of the image, and low cost and ease of use. Since future prospects will address cluster compactness and its relationship to volumes, another action to be developed in the future will be to design and build a platform that supports the configuration of the image acquisition protocol and that can be loaded on a mobile platform such as a quad.

The **third paper** develops a successful methodology that generates a Canopy Height Model for conducting forest inventories. In particular, by integrating the terrain data in the photogrammetric cloud, it is possible to incorporate LiDAR's capacity for terrain detection in zones of dense vegetation with the greater spatial, radiometric and temporal resolution of low-cost photogrammetry from alternative platforms such as the aerial trike or RPAS. The advantage offered by this methodology is that it allows a CHM to be obtained with adequate phenological detail due to the combination of LiDAR flights performed at low temporal resolution and low-cost photogrammetric flights performed with the required periodicity. In future work, we shall address the forestry variables in the obtained dense cloud and perform a comparative study with the variables obtained from the LiDAR information, applying rodal, individual-tree or even a combination of both methods to benefit from the high resolution of the initial data. Another line of enquiry will be to contrast the variables obtained from the dense cloud with other data from a classic inventory of the study zone.

Generally concluding this research, we can verify that low cost and close-range photogrammetry applied to Agroforestry Engineering provides valid information for optimal management, reducing field time and associated cost, as well as it improves accuracy, quality and quantity of the obtained results.

Appendix I

Congress publications, ISPRS 2015

APPENDIX A. CONGRESS PUBLICATIONS, ISPRS 2015

- Herrero-Huerta, Mónica and Lindenbergh, R. C. "Automatic Tree Breast Height Diameter Estimation from Laser Mobile Mapping Data in an Urban Context". In *International Archives of the Photogrammetry, Remote Sensing and Spatial Information Sciences, Volume XL-3/W3, 2015. ISPRS Geospatial Week 2015, La Grande Motte, France, 28 September-3 October 2015*. ISPRS.

- Lindenbergh, R. C., Berthold, D., Sirmacek, B., Herrero-Huerta, M., Wang, J., & Ebersbach, D. "Automated large scale parameter extraction of road-side trees sampled by a laser mobile mapping system". In *International Archives of the Photogrammetry, Remote Sensing and Spatial Information Sciences, Volume XL-3/W3, 2015. ISPRS Geospatial Week 2015, La Grande Motte, France, 28 September-3 October 2015*. ISPRS.

Automatic Tree Breast Height Diameter Estimation from Laser Mobile Mapping Data in an Urban Context

Mónica Herrero-Huerta[1] and Roderik Lindenbergh[2]

[1]*Department of Cartographic and Land Engineering, University of Salamanca, Higher Polytechnic School of Avila, Hornos Caleros 50, 05003, Avila, Spain. Phone number: 0034-920353500-3820, monicaherrero@usal.es*
[2] *Department of Geoscience and Remote Sensing, Delft University of Technology, 2628 CN Delft, The Netherlands.*

Highlights: This study focuses on developing an innovative methodology to automatically estimate the diameter at breast height (DBH) of urban trees sampled by a Laser Mobile Mapping System (LMMS). The high-quality results confirm the feasibility of the proposed methodology, providing scalability to a comprehensive analysis of urban trees.

Keywords*: breast height diameter, LiDAR, urban trees, laser mobile mapping system, estimation.*

Introduction

Accurate measures of structural parameters of urban trees and monitoring their changes over time are essential to inventory of urban trees and growth models, modelling of carbon cycle and management systems of urban trees [1]. The estimation of these variables has traditionally been done with field inventories via pilot samplings. The advent of recent remote sensing technologies has opened up a new field of possibilities for carrying out such work through non-destructive methods, providing advantages regarding the economic costs involved, the time invested and estimation errors.

Among the various urban tree measurements, DBH (stem diameter at 1.3 m height) is an important tree inventory attribute because it serves as a fundamental parameter in tree allometry and estimation of basal area, thus providing valuable information about individual trees and tree stand structure. Many countries store the DBH of urban trees in cadaster databases for monitoring purposes .

The application of LMMS (Laser Mobile Mapping System) enables to fast and accurately capture 3D data of individual urban trees along the road. However, no research has been done on retrieving DBH using this technology. LMMS operates at the suitable work scale between manual and airborne LiDAR measurements. The latter fails to capture the complete vertical distribution of the canopy [2]. Terrestrial Laser Scanning has been used for estimating tree parameters[3], but being time-consuming compared with LMMS in an urban context. However, the method proposed has to face additional difficulties due to the specific acquisition geometry of the technology mentioned, such as the partial 3D data (only one side view), or having to deal with occluding vegetation, leading to underestimations compared to manually collected field data [4].

The aim of the present work is to develop an efficient and precise methodology in a novel way, to obtain DBH of urban trees destined for inventories based on point clouds coming from LMMS. Additionally, the influence of the density of points on the accuracy of deriving DBH estimations were investigated.

Materials and Methods

Laser Mobile Mapping System

For this work, data acquired by Fugro Drivemap is considered. This LMMS is composed of two high performance laser scanners type Riegl VQ250, a four-wheeled all-terrain vehicle and a navigation unit. The Global Positioning System has 10 Hz of positioning rate and the laser pulse rate is 1.333·106 pulses/s, being the maximum density 115000 points/m^2, the field of view 360^{o}x 26.8^o, the ranging accuracy less than 2cm and the maximum range 30 m.

Ground Inventory Data

The ground truth of the DBH was established using a measurement tape by a qualified operator at 5 centimeter precision. It should be remarked that the studied trees are less than 10 meters from de road.

DBH tree extraction Methodology

Before estimating the DBH, the extraction of individual trees of the point cloud is necessary through an automated workflow by voxel analysis (not the aim of this study). For the DBH tree extraction methodology the following steps are performed for each tree (Figure 1):

1). Outliers removal.

A statistical analysis on each point's neighbourhood is performed by assuming a Gaussian distribution. All points whose mean distance is outside an interval defined by the global mean distance and standard deviation are considered as outliers and removed from the dataset.

2). Extraction of trunk data.

The limit between the trunk and canopy is calculated by the curvature change of the histogram that represents the number of filled voxels of 0.25 cm^3 size as a function of height.

If the histogram shows there are ramifications in the trunk, k-means is used to assign a cluster (k clusters) to each data point ($\mathbf{x}_i$,i=1...n). K-means is a clustering method that aims to find the positions μ_i,i=1...k of the clusters that minimize the Euclidean distance from the data points to the cluster (Equation 1):

$$\arg min_c \sum_{i=1}^{k} \sum_{x \in c_i} d(x, \mu_i) = \arg min_c \sum_{i=1}^{k} \sum_{x \in c_i} ||x - \mu_i||_2^2 \quad (1)$$

where $\mathbf{c}_i$ is the set of points that belong to cluster i.

3). Determining the orientation of each trunk by Principal Component Analysis (PCA) and projecting the trunk points into a plane orthogonal to the axis corresponding to the principal direction.

A classical approach consists in performing a PCA of the 3D coordinates of the point cloud of the trunk. This statistical analysis uses the first and second moments of the point cloud, and results in three orthogonal vectors centered on the centroid of the point cloud. The PCA synthesizes the distribution of points along the three dimensions, and thus models the principal directions and magnitudes of variation of the point distribution around the center of gravity [6].

4). Fitting a circle to the projected trunk points by using RANSAC (RANdom SAmple Consensus) to mitigate the influence of outliers [7].

DBH was retrieved from laser datasets by circle fitting at different height bins. This can be done because of the assumption that the diameter is not significantly varying along a short length of the stem for mature trees.

Points that deviated most from a fitted circle were considered noise and removed for DBH estimations through the RANSAC method.

5). Quality control by obtaining the RMSE of the DBH estimated and measured at different height bin sizes.

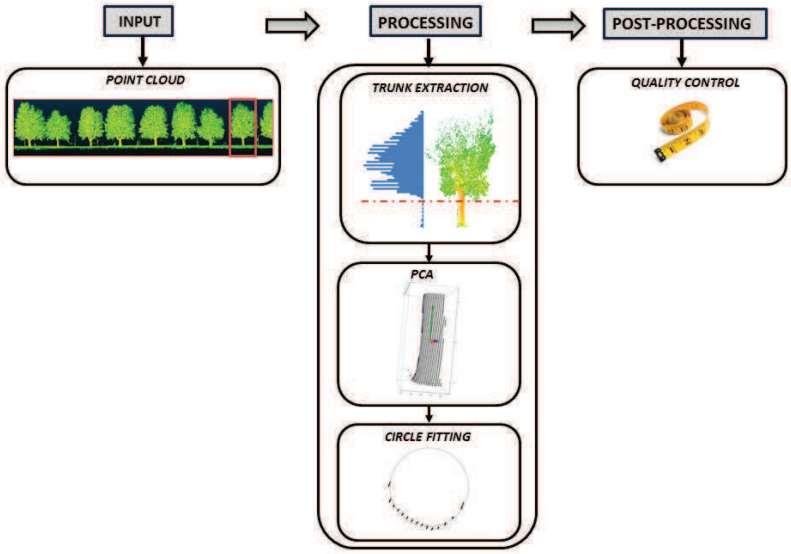

Figure 1. Workflow of the DBH Methodology

Experimental Results

The study area is located at the Delft University of Technology campus (lat. 52º00´ N; long. 4º22´ E; 1 m asl, The Netherlands) and tree species include Plantanus and Quercus. Data collection was performed on the 4th of November 2014 covering an area of approximately 750 x 1200 m on a day without wind. The dataset consists of 53,958,666 points, with the x, y and z coordinates and intensity. A pre-processing step of this dataset was carried

out in order to obtain the individual trees of the zone of interest. After that, the point cloud has 1,860,156 points with no intensity. There are 29 trees in total, 14 Platanus and 15 Quercus. The diameters of the first one are bigger than the others.

The accuracy of DBH estimation is influenced by several factors. Different height bins for determining the number of points to fit the circle, were tested to derive reliably DBH estimations. In addition, DBH estimation errors were confronted with the number of points to fit the circle but a relation was not seen.

Table 1 collects the robust statistical parameters of the linear regression stablished between the actual and the estimated DBH at different height bin sizes. The probability of success to achieve a right DBH defined by this parameters, is also included. From this analysis, it is possible to conclude that 20 cm height bin provides better results, from 1.20 m to 1.40 m height of each individual tree.

Table 1. Correlation coefficients and probability of success at different bin sizes

Circle Fitting Height Bin (m)	R^2	RMSE (cm)	Probability of Success (%)
1,25-1,35	0,792	5,67	62,1
1,20-1,40	0,837	4,35	79,3
1,10-1,50	0,688	6,45	75,9
1,00-1,60	0,600	12,12	86,2

Conclusions

This research presents a non-invasive method with application to urban tree inventory that consists of DBH estimation. The method is fast, reliable, robust and objective, and could serve to take decisions in advance regarding actions to be taken in urban trees and planning the management and maintenance optimally. This study also discussed the influence of the number of points to fit the circle and circle fitting height bin size on the influence of DBH estimation accuracy, validated against field measurements. Regarding these variables, the results show that there is no significant relation between the number of points and the DBH estimation errors. A 20 cm height bin provides better results, reaching a R^2 value of 0.84 and a RMSE of 4.35 cm with a probability of success of 79.3%. In addition, the results show that working only on one side of the tree, the visible side from the road, is still feasible for approximating the DBH with an accurate and precise fit.

This methodology can be extrapolated to a comprehensive study of urban trees.

It should be mentioned that the proposed methodology is part of a robust and efficient workflow which considers the automated, large scale extraction of tree sizes and locations sampled by a laser mobile mapping system. It includes tree location, level height and crown width throw a sensitivity analysis.

Acknowledgements

Authors would like to thank FUGRO GeoServices B.V. for providing the dataset. The result is partly funded by the IQmulus project (FP7-ICT-2011-318787).

References

[1] Næsset, Erik. "Practical large-scale forest stand inventory using a small-footprint airborne scanning laser." Scandinavian Journal of Forest Research 19.2 (2004): 164-179.

[2] Lim, K., Treitz, P., Wulder, M., St-Onge, B., & Flood, M. (2003). LiDAR remote sensing of forest structure. Progress in physical geography, 27(1), 88-106.

[3] Srinivasan, Shruthi, et al. "Terrestrial Laser Scanning as an Effective Tool to Retrieve Tree Level Height, Crown Width, and Stem Diameter." Remote Sensing 7.2 (2015): 1877-1896.

[4] Moskal, L. M., & Zheng, G. (2011). Retrieving forest inventory variables with terrestrial laser scanning (TLS) in urban heterogeneous forest. Remote Sensing, 4(1), 1-20.

[5] Hartigan, J. A., & Wong, M. A. (1979). Algorithm AS 136: A k-means clustering algorithm. Applied statistics, 100-108.

[6] Van Goor, B., Lindenbergh, R. C., & Soudarissanane, S. S. (2011, August). Identifying corresponding segments from repeated scan data. In ISPRS Workshop Laser Scanning 2011, Calgary, Canada, 29-31 August 2011; IAPRS, XXXVIII (5/W12), 2011. International Society for Photogrammetry and Remote Sensing (ISPRS).

[7] Schnabel, Ruwen, Roland Wahl, and Reinhard Klein. "Efficient RANSAC for Point Cloud Shape Detection." Computer graphics forum. Vol. 26. No. 2. Blackwell Publishing Ltd, 2007.

AUTOMATED LARGE SCALE PARAMETER EXTRACTION OF ROAD-SIDE TREES SAMPLED BY A LASER MOBILE MAPPING SYSTEM

R.C. Lindenbergh[a,*], D. Berthold [b], B. Sirmacek[a], M. Herrero-Huerta [a], J. Wang [a], D. Ebersbach [b]

[a] Dept. of Geoscience & Remote Sensing, Delft University of Technology, Delft, The Netherlands
(r.c.lindenbergh, b.sirmacek, m.herrerohuerta, jinhu.wang)@tudelft.nl
[b] LEHMANN + PARTNER GmbH, Schwerborner Straße 1, D-99086 Erfurt - (Berthold,Ebersbach)@lehmann-partner.de

Commission III, WG III/5

KEY WORDS: big data, laser mobile mapping, tree parameters, urban, voxels

ABSTRACT:

In urbanized Western Europe trees are considered an important component of the built-up environment. This also means that there is an increasing demand for tree inventories. Laser mobile mapping systems provide an efficient and accurate way to sample the 3D road surrounding including notable roadside trees. Indeed, at, say, 50 km/h such systems collect point clouds consisting of half a million points per 100m. Method exists that extract tree parameters from relatively small patches of such data, but a remaining challenge is to operationally extract roadside tree parameters at regional level. For this purpose a workflow is presented as follows: The input point clouds are consecutively downsampled, retiled, classified, segmented into individual trees and upsampled to enable automated extraction of tree location, tree height, canopy diameter and trunk diameter at breast height (DBH). The workflow is implemented to work on a laser mobile mapping data set sampling 100 km of road in Sachsen, Germany and is tested on a stretch of road of 7km long. Along this road, the method detected 315 trees that were considered well detected and 56 clusters of tree points were no individual trees could be identified. Using voxels, the data volume could be reduced by about 97 % in a default scenario. Processing the results of this scenario took ˜2500 seconds, corresponding to about 10 km/h, which is getting close to but is still below the acquisition rate which is estimated at 50 km/h.

1. INTRODUCTION

Recent years saw a rapid development of sensor systems that efficiently sample our 3D environment at high detail, (Vosselman and Maas, 2010). Mobile mapping systems implemented in helicopters and cars obtain point clouds consisting of millions to billions of points at a daily basis, (Haala et al., 2008, Puente et al., 2013). In addition, methods from e.g. computer vision and computational geometry became available over the last years that are able to extract useful information from such 3D point clouds by estimating locations and sizes of the different objects sampled by the point clouds, (Puttonen et al., 2011, Rutzinger et al., 2010). Such methods are typically demonstrated in the scientific community at case study scale however. Examples are given of the extraction of geometric parameters from one facade, one or a few trees or 300 m of road furniture, (Monnier et al., 2012). So far, the number of publications that specifically addresses the difficulties of processing large urban point clouds is limited, (Weinmann et al., 2015).

Unfortunately it turns out far from trivial to efficiently exploit the possibilities of combining large 3D point clouds and 3D geometry extraction methods, (Krämer and Senner, 2015). Computers have limited memory capacity, which means that input data needs to be (re)divided into manageable chunks. At the same time an automated division strategy will often affect the objects of interest, as data division will take place before object extraction. Another problem is that the results of geometry extraction algorithms often depend on parameters. For an individual case study such parameters can easily be tuned. When automatically processing an unseen, large data set with a variety of different realizations of the same object type, parameter tuning should be either unnecessary or automated. Another challenge is to make algorithms responsible for the compatibility between consecutive steps: the output of step $(k-1)$ is the input of step k. Even powerful geometry extraction methods may fail when sampling is locally hampered by unfavorable acquisition conditions. Therefore it is important that a human operator responsible for quality control is automatically guided to such locations.

For the workflow presented in this paper the strategy to mitigate the negative effects of large point clouds on computational feasibility, is to process as much as possible at voxel level, rather then at the individual point level. That is, the original point cloud is subdivided into small cubic cells, the voxels, and consecutive information extraction takes place by analyzing local voxel configurations. Switching to voxels has some advantages. Data volume and therefore memory usage is reduced, as many points in one voxel are simply replaced by one single voxel value (Either voxel center, or center of gravity of the points in the voxel); The effect of varying point densities in scan data is largely resolved and irregular points are replaced by regular voxels cells, which makes spatial indexing more efficient; Smaller gaps in data coverage caused by occlusions in the scanning play a smaller role because of the lower resolution of the voxels. Voxels are the most simple way to subdivide a 3D domain. More sophisticated and more scalable is to organize a point cloud in a so-called kd-tree, which allows to prune the point cloud to a certain level, (Triebel et al., 2006), or in an octree.

Even when voxels are processed instead of the original points, files consisting of these voxels can grow arbitrary large if simply merged without strategy. Therefore some additional tiling and stitching strategy is needed that chops data in manageable chunks, either for single node processing or for parallel execution, (Yang and Zhang, 2015). If one such chunk can be processed in a reasonable time, the method would not change if you process 1km, 10km, or 10 000 km of data along urban streets, which is

*Corresponding author

exactly what is required in practical applications. Here 'reasonable time' is often defined such that processing the data does not take more time then acquiring the data. So, the only remaining requirement is that it should be demonstrated that processing a chunk doesn't take more time then acquiring it.

The above mentioned advantages of using voxels, kd-trees and octrees and octrees are reasons that several voxel based methods have been designed for natural tree related processing of point clouds. (Popescu and Zhao, 2008) divide their airborne point clouds of trees in voxels to determine the transition between trunk and canopy. (Bucksch et al., 2010) organize notably panoramic scanner point clouds sampling trees in voxels to reconstruct the branch structure of trees; (Wu et al., 2013) organize laser mobile mapping data in voxels to divide tree points over individual trees. (Cabo et al., 2014) detect pole like objects in mobile mapping scan points using voxels, which allowed to work on 20-30 % of the original data volume. (Lim and Suter, 2009) use initial individual point features to group points in so-called super voxels, which are used in consecutively obtaining point cloud classification results of a panoramic scanner point cloud.

This short literature review indicates that in principle methods exist that satisfy the needs of the workflow presented in this paper. Still it was chosen to use methods that were implemented from scratch for the following reasons. Available methods typically solve a problem at hand in an approximate way, in the sense that they may estimate related parameters, but not exactly the parameters required by a particular application. In addition, available methods were often developed while solving a problem within the particular context of a specific data set. Applying the method on different data often gives incorrect results. Note that this problem is partly solved by data processing contests, e.g. (Vallet et al., 2015), which compare methods in a more uniform way. Another issue is that within a workflow back-to-back processing is required: the output of the previous module is the input of the next module. A condition which is typically not fulfilled without extra work when relying on available methods. Finally that a method is published doesn't mean that an implementation is available, nor that input and output formats, programming language and targeted operating system match. For the combination of these reasons it was decided to implement the workflow from scratch using relatively light but flexible methodology.

2. METHODOLOGY

In this work we will present a processing chain aiming at the robust and efficient large scale extraction of tree sizes and locations.

2.1 Data description

The processing chain is initially tested on 7 km of laser mobile mapping data, sampling a test route in Saxony, Germany. The laser mobile mapping system contains a clearance profile scanner from Fraunhofer IPM, collecting up to 2 million points per second. The relative precision of each single laser point is 4 mm. The absolute geographic precision of the point cloud is about 15 cm, ensured by a 2 antenna GPS/GNSS positioning system supported by a 200 Hz IMU from APPLANIX and differential GPS corrections applied in postprocessing.

The mobile mapping system originally records the laser scanner data on the road in a binary format until 1 GByte is reached per file (and then the next 1 GB container will be filled etc.). These binary data containers were converted to xyzi-format and separated into 10 meter chunks. These 10 meter chunks are the starting point of the processing chain described in this work. The test road is represented by 830 xyzi files (the 10 meter chunks) of in total 17 GByte. In single cases, the car had to stop because of traffic which lead to larger files. Together, these 830 files contain 427 186 054 points. The processing chain below doesn't use the intensity data, only the xyz information. In its final form the processing chain will be used to extract tree locations and sizes for 100 km of laser mobile mapping data. For this area, ground truth tree locations obtained by a human operator are available.

2.2 Processing chain

The processing chain consist of the steps listed below. Each step corresponds to an algorithm which allows the user to specify up to two parameters as indicated. Some more details are given below.

Downsampling and retiling, with two parameters: voxel size, and maximum number of points per tile.

Tree point classification, with two parameters: grid size and minimum tree height:

Tree segmentation, with two parameters, minimum canopy diameter and voxel size

Tree parameters, rough, no parameters

Upsampling per tree, no parameters

Tree parameters, fine, no parameters

What follows is a short description of the described methodology.

The input data is provided in chunks that in principal correspond to 10m of road. It is assumed that these chunks are ordered according to the order in which they were sampled A main step to make the processing feasible is actually the first step, the downsampling and retiling step. In this step, input data chunks are read and uniformly downsampled. This means that a fixed voxel size is set by the user, e.g. 30 cm, which defines a 3D grid over the scene sampled by the chunk. Consecutively all original points in a given voxel cell are replaced by the center of gravity of those points. Downsampled points are collected in order until a preset number of points is reached. These, for example 200 000 points are written to a file. Therefore this step will result in files containing at most 200 000 points at a resolution of 30 cm.

These retiled files are the input for the classification step, (Sirmacek and Lindenbergh, 2015). The aim of this step is to divide the 3D points in two classes, tree and non-tree points. In this step a 2D grid is defined over the data of a given grid size, e.g. 20 cm. For each grid cell, the number of 3D points are counted whose xy location belong to the grid cell. Local maxima in the resulting counts are assumed to correspond to tree locations. 3D points above the ground and close to these tree locations will be assigned to the tree class, the other points to the non-tree class. To distinguish trees from shrubs, a minimal tree height can be defined by the user, for example 2 m. A disadvantage of the current algorithm is that it sometimes generates false positives at street poles. This step is also illustrated in Figure 1. In the left image, points colored gray are non-tree points, while the dark green points are classified as trees.

The classified points proceed to the tree segmentation step. Goal of this step is to segment the tree points into individual trees. To do so, tree points are again distributed over a 3D voxel structure. First local maxima are detected. If a local maximum is sufficiently prominent, according to the minimum canopy width

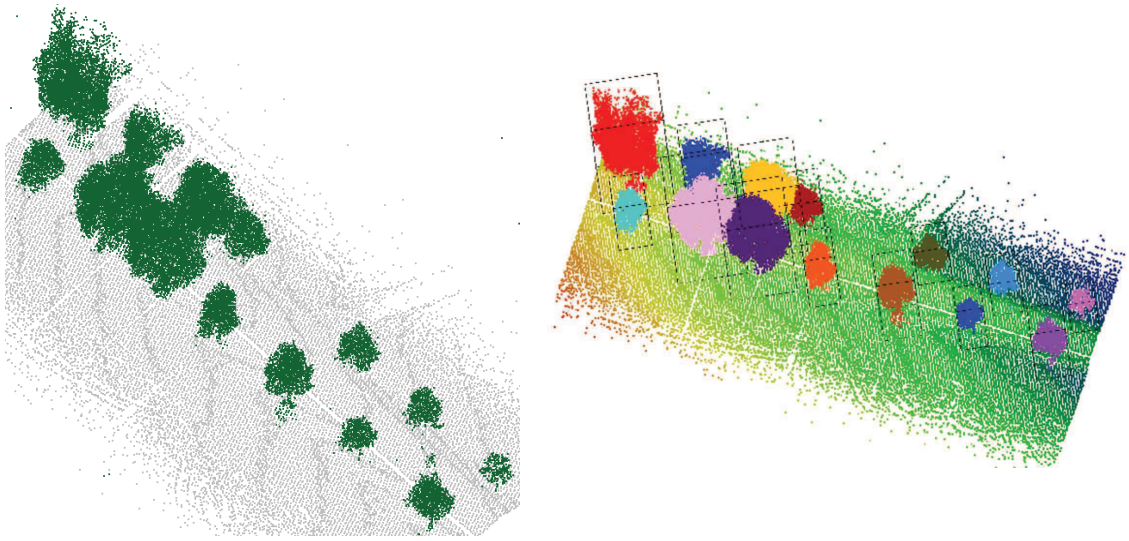

Figure 1: **Left** Points classified as trees (green points) and other (gray points). **Right** Identified individual trees (solid colors) in their bounding box.

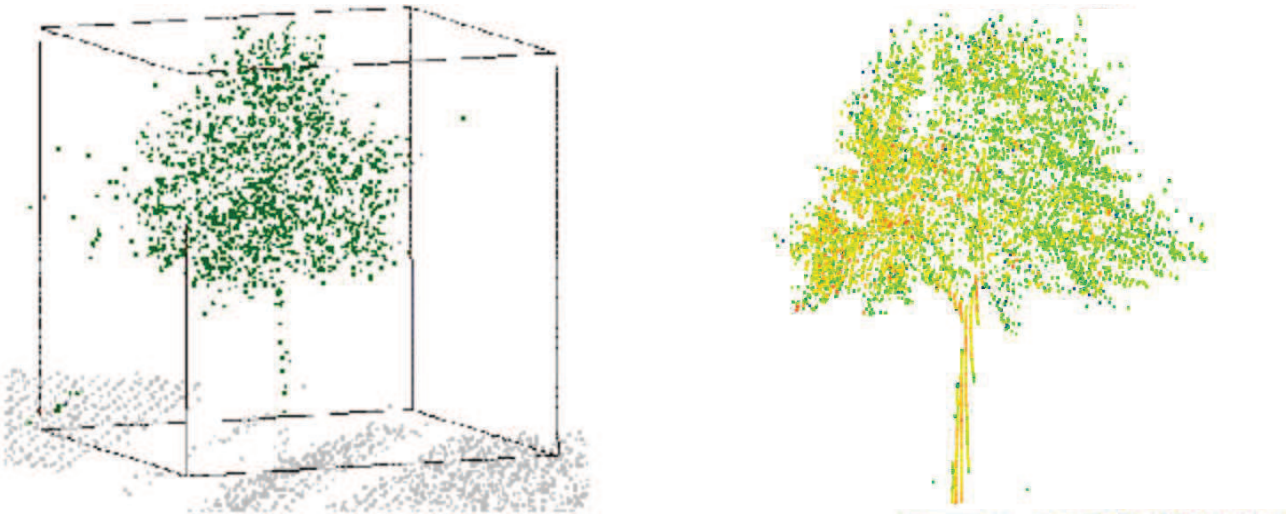

Figure 2: Restoring of the original tree points for one individual tree. **Left**. Voxelized points belonging to a tree (in dark green) and not belonging to this tree (in gray). **Right**. Using the bounding box in the left image, the original points are restored in the right image. These original points are used to determine final tree parameters like Diameter at Breast Height (DBH).

parameter, it is selected as a seed point for growing a tree by traversing the layers of the adjacent octree cells from top to bottom. Voxel cells at a certain layer in between two seed points, are assigned to one of the two seed points according to a proximity criterion. The success of this tree segmentation step is indicated by a quality flag which can be used to guide a human operator to situations were automated processing was not successful.

As a result of the tree segmentation step, tree voxels are assigned to individual trees. By determining the bounding box of all voxels belonging to one tree, a first estimation of the canopy width, tree height and tree location is obtained. Indeed, the canopy width and tree height are simply the width and height of the bounding box, while an estimation for the tree location is the intersection of the horizontal diagonals of the bounding box. This step is illustrated on the right in Figure 1. Different trees have different colors, and around each tree a bounding box is visible.

Note that all of the tree extraction steps above were performed on the uniform downsampled point cloud of, say, 30 cm resolution. As by now individual trees have been identified, it is possible and also computationally feasible to go back to the full resolution original point cloud, as the correspondences between downsampled points and original points were maintained.

The final step is therefore performed per individual tree on the original points, compare Figure 2. In the left image, the downsampled points are shown, in the right image, the original points are restored. The number of down-sampled tree points in this example is 1702, while the original number of points inside the bounding box is 22 283. Using a histogram analysis of the vertical distribution of the tree points, compare also (Popescu and Zhao, 2008), the trunk is separated from the canopy. The direction of the trunk is estimated by Principal Component Analysis (PCA) and the diameter at breast height (DBH), which is the diameter of a tree at 1m30, (Bucksch et al., 2014), is estimated by determining the diameter of a circle through tree points, after

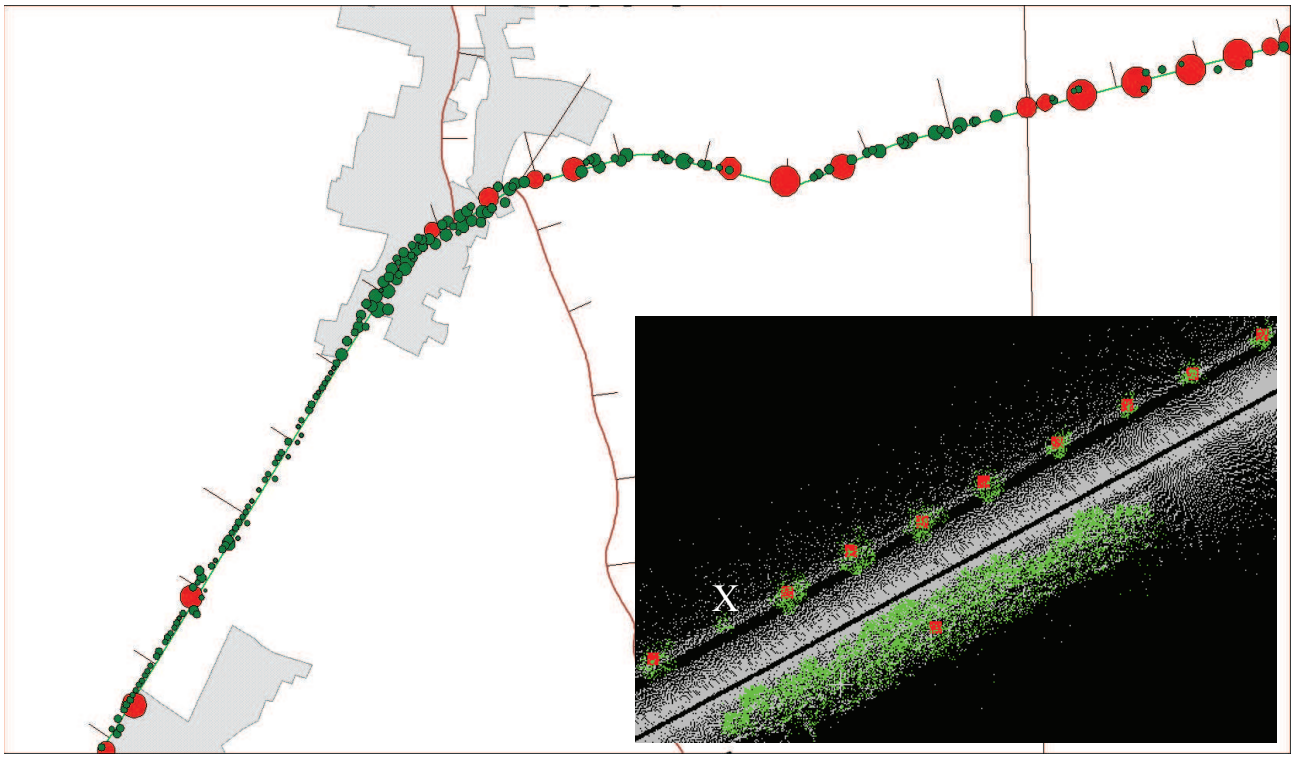

Figure 3: **Large figure:** Identified trees. Green circles correspond to tree locations marked by the method as correct, red circles correspond to tree points where the algorithm was not able to identify individual trees. **Small figure:** some tree classification and segmentation results. Green points were identified as tree points. The red markers indicate single trees (top of the road) or a cluster of trees that couldn't be segmented (bottom of the road).

Figure 4: An estimation of the Diameter at Breast Height (DBH) is obtained by fitting a circle to projected trunk points of an appropriate portion of the trunk.

removing outliers using RANSAC, (Fischler and Bolles, 1981), compare also Figure 4. The figure shows only a partially sampled circle, which corresponds to the mobile mapping system seeing only the part of the trunk that is facing the road. The PCA step in combination with restoring the original point cloud can also be used to improve the estimation of the location of the tree by determining the intersection of the principal axis with the terrain.

2.3 Sensitivity analysis

There is an apparent tradeoff between the different parameters. Downsampling with a smaller voxel size in the first step will result in a higher resolution downsampled file, which contains more details, from which consecutive steps could profit. At the same time, if the maximum number of points per tile is kept fixed, the spatial extent of the tile will shrink. This implies that more trees will be cut in two at tile boundaries, which will negatively affect the results.

Increasing the number of points per tile will in turn have a negative effect on the computational performance of the processing chain. In addition, the first three steps, downsampling, classification and tree segmentation, all us a 2D or 3D grid. How the sizes of these grids interact should be further investigated.

Note that in the current workflow the first three steps all use voxels or pixels. In the current implementation the different voxel and pixel sizes are not yet aligned. Therefore it is for example possible that when using a voxel size of 30 cm in the first step, as stated as an example above, and having a grid size of 20 cm in the second step, some grid cells are in fact empty. It would be preferably if these sizes were aligned, as it would further simplify the tuning of the remaining parameters and the interpretation of unexpected results.

3. RESULTS

All above mentioned steps have been implemented, but the final tree parameter estimation step could not yet been tested within the workflow.

As 'default' settings, the values as shown in Table are used. The large image in Figure 3 shows results for part of the 7km of road considered as case study. Green disks indicate trees identified by the processing chain. The diameter of each disk corresponds to the estimated width of the tree canopy. Red disks correspond to tree points where the segmentation method was not able to identify single trees. The algorithm indicates this by a quality flag, which guides an operator to these cases. Again, the diameter of the red disks correspond to the width of the bounding box, in

Step	Parameter	Value
Downsampling	Voxel size	0.3 m
	Max points per tile	20 000
Classification	Grid size	0.2 m
	Min. tree height	2 m
Segmentation	Voxel size	1 m
	Min. canopy diameter 6 m	

Table 1: Default settings workflow

this case of the cluster of tree points that couldn't be segmented. As such cluster in reality typically corresponds to a number of trees, the diameters of the red disks are in general larger than those of the green disks. In total 315 trees were identified using default settings. For an additional 58 tree point clusters the tree segmentation step didn't succeed in identifying individual trees. Note however, that the locations of the identified trees currently have not yet been validated using the ground truth data.

The small image in Figure 3 illustrates some of the intermediate steps. The results of the classification are indicated in green (tree points) and grey (non tree points). Locations of successfully identified trees at the top of the road are indicated by a red marker. Note that a small tree marked 'X' was not identified, probably because it was to small and therefore removed. The tree segmentation method failed on the large cluster of tree points at the bottom of the road. In this case, the location of the cluster is still reported, but with a quality flag indicating the lack of success. In this case also a human operator would probably have difficulties to separate this cluster into individual trees.

The effect of using voxels on the data volume is shown by the following example. Retiling the first 50 tiles using a voxel size of 30 cm reduced the number of points from 23 282 574 to 518 365 points, which corresponds to a reduction in data volume of 97.8 %.

Increasing the tile size could affect memory usage in a negative way but should decrease tiling effects. The effect of changing the voxel size in the first step is less obvious, as also consecutive steps use voxels. Full evaluation of results of different scenarios, including validation against ground truth, will take place after the voxel sizes have been harmonized throughout the workflow

The tests in Table 1 were run on a desktop PC with Intel Xeon 3.6GHz processor and 16GB of RAM. All algorithms where implemented in C++ and compiled and run on the Ubuntu 14.04 64-bit operating system. Running the scenario with the default settings, corresponding to the first row in Table 1 took 2573 seconds in total, which means that 1 km of data takes about 2573:7 km = 368 seconds. This processing speed corresponds to roughly 10 km an hour. This means that the initial goal of processing at the same rate as the acquisition is close but not yet met, as this probably would mean that the processing rate should be improved by a factor five. Probably this improvement could be reached by a further optimization of the current code.

The total computation time of the presented scenario's is divided over the different steps as follows: Retiling takes approximately 65 %, classification takes 32 % and tree separation 2 %. Change of scenario has no large effect on this division, that is effects are not more then a few per cent. It makes sense that computational efforts drop throughout the workflow. Retiling still considers the full input point clouds and file reading and writing is required. Classification only operates on voxels. Finally, tree separation works on tree voxels only. The final tree parameter estimation step, where the full point clouds within the bounding boxes are restored, were not available for testing yet.

CONCLUSIONS

In paper a processing chain aiming at the extraction of tree locations and tree sizes from laser mobile mapping data is presented. All-though further validation is needed, initial results indicate that the workflow is able to extract individual trees at sufficient quality and at a rate that is approximating the data acquisition rate: processing takes place at a rate of about 10 km/h. For efficient processing, the input is downsampled using voxels to a volume that is below 3 % of the original data volume. Besides validation, still harmonization between the parameters in the different steps is required. Such steps, in combination with code optimization are expected to be sufficient to reach the final goal of automatized estimation of features sampled by mobile mapping at a rate that matches the acquisition speed and at a quality that matches the result of a human operator.

ACKNOWLEDGMENTS

This work is initiated on behalf of the LISt-GmbH, kindly supported by the Saxon State Ministry for Economic Affairs, Labour and Transport, Germany. The research is partly funded by the FP7 project IQmulus (FP7-ICT-2011-318787), aiming at the design and implementation of a high volume fusion and analysis platform for geospatial point clouds, coverages and volumetric data sets.

REFERENCES

Bucksch, A., Lindenbergh, R., Abd Rahman, M. Z. and Menenti, M., 2014. Breast height diameter estimation from high-density airborne LiDAR data. IEEE Geoscience and Remote Sensing Letters 11(6), pp. 1056 – 1060.

Bucksch, A., Lindenbergh, R. and Menenti, M., 2010. SkelTre – Robust skeleton extraction from imperfect point clouds. Visual Computer 26(10), pp. 1283 – 1300.

Cabo, C., Ordonez, C., García-Cortés, S. and Martínez, J., 2014. An algorithm for automatic detection of pole-like street furniture objects from mobile laser scanner point clouds. ISPRS Journal of Photogrammetry and Remote Sensing 87, pp. 47 – 56.

Fischler, A. and Bolles, C., 1981. Random sample consensus: a paradigm for model fitting with applications to image analysis and automated cartography. Communications of the ACM 24(6), pp. 381 – 395.

Haala, N., Peter, M., Kremer, J. and Hunter, G., 2008. Mobile LiDAR mapping for 3D point cloud collection in urban areas – a performance test. International Archive of Photogrammetry, Remote Sensing and Spatial Information Sciences 37, pp. 1119 – 1127.

Krämer, M. and Senner, I., 2015. A modular software architecture for processing of big geospatial data in the cloud. Computers & Graphics 49, pp. 69 – 81.

Lim, E. and Suter, D., 2009. 3D terrestrial LIDAR classifications with super-voxels and multi-scale conditional random fields. Computer-Aided Design 41(10), pp. 701–710.

Monnier, F., Vallet, B. and Soheilian, B., 2012. Trees detection from laser point clouds acquired in dense urban areas by a mobile mapping system,. ISPRS Annals of the Photogrammetry, Remote Sensing and Spatial Information Sciences 3(3), pp. 245 – 250.

Popescu, S. C. and Zhao, K., 2008. A voxel-based lidar method for estimating crown base height for deciduous and pine trees. Remote Sensing of Environment 112(3), pp. 767 – 781.

Puente, I., Jorge, H. G. ., Martínez-Sánchez, J. and Arias, P., 2013. Review of mobile mapping and surveying technologies. Measurement 46(7), pp. 2127 – 2145.

Puttonen, E., Jaakkola, A., Litkey, P. and Hyyppä, J., 2011. Tree classification with fused mobile laser scanning and hyperspectral data. *Sensors*, 11(5), pp. 51585182. Sensors 11(5), pp. 5158 – 5182.

Rutzinger, M., Pratihast, A., Oude Elberink, S. and Vosselman, G., 2010. Detection and modelling of 3d trees from mobile laser scanning data. ISPRS Archives of Photogrammetry, Remote Sensing and Spatial Information Sciences 38(5), pp. 521 – 525.

Sirmacek, B. and Lindenbergh, R., 2015. Automatic classification of trees from laser scanning point clouds. ISPRS Annals of the Photogrammetry, Remote Sensing and Spatial Information Sciences. Vol. II-3/W5.

Triebel, R., Kersting, K. and Burgard, W., 2006. Robust 3D scan point classification using associative markov networks. In: Proceedings of the 2006 IEEE International Conference on Robotics and Automation, Orlando, United States.

Vallet, B., Brédif, M., Serna, A., Marcotegui, B. and Paparoditis, N., 2015. Terramobilita/iqmulus urban point cloud analysis benchmark. Computers & Graphics 49, pp. 126 – 133.

Vosselman, G. and Maas, H. (eds), 2010. Airborne and Terrestrial Laser Scanning. Whittles Publishing.

Weinmann, M., Urban, S., Hinz, S., Jutzi, B. and Mallet, C., 2015. Distinctive 2D and 3D features for automated large-scale scene analysis in urban areas,. Computers & Graphics 49, pp. 47–57.

Wu, B., Yu, B., Yue, W., Shu, S., Tan, W., Hu, C., Huang, Y., Wu, J. and Liu, H., 2013. A voxel-based method for automated identification and morphological parameters estimation of individual street trees from mobile laser scanning data. Remote Sensing 5(2), pp. 584–611.

Yang, J. and Zhang, J., 2015. Parallel performance of typical algorithms in remote sensing-based mapping on a multi-core computer. Photogrammetric Engineering & Remote Sensing 81, pp. 373 – 385.

Appendix II

Indexation and impact factor of the publications

APPENDIX B. INDEXATION AND IMPACT FACTOR OF THE PUBLICATIONS

1. Vicarious Radiometric Calibration of a Multispectral Sensor from an Aerial Trike Applied to Precision Agriculture

2. Vineyard Yield Estimation by Automatic 3D Bunch Modelling in Field Conditions

Description of the journal:

Journal:	**COMPUTERS AND ELECTRONICS IN AGRICULTURE**
URL:	**http://www.journals.elsevier.com/computers-and-electronics-in-agriculture/**
Editorial:	**ELSEVIER**
ISSN:	**0168-1699**
Impact factor (2013):	**1.486**
Quartile:	**Q1**

ISI Web of Knowledge℠

Journal Citation Reports®

WELCOME | HELP | RETURN TO LIST

2013 JCR Science Edition

Journal: COMPUTERS AND ELECTRONICS IN AGRICULTURE

Mark	Journal Title	ISSN	Total Cites	Impact Factor	5-Year Impact Factor	Immediacy Index	Citable Items	Cited Half-life	Citing Half-life
☐	COMPUT ELECTRON AGR	0168-1699	2798	1.486	2.066	0.148	189	5.6	8.2

Cited Journal | Citing Journal | Source Data | Journal Self Cites

CITED JOURNAL DATA | CITING JOURNAL DATA | IMPACT FACTOR TREND | RELATED JOURNALS

Journal Information

Full Journal Title: COMPUTERS AND ELECTRONICS IN AGRICULTURE
ISO Abbrev. Title: Comput. Electron. Agric.
JCR Abbrev. Title: COMPUT ELECTRON AGR
ISSN: 0168-1699
Issues/Year: 12
Language: ENGLISH
Journal Country/Territory: ENGLAND
Publisher: ELSEVIER SCI LTD
Publisher Address: THE BOULEVARD, LANGFORD LANE, KIDLINGTON, OXFORD OX5 1GB, OXON, ENGLAND
Subject Categories: AGRICULTURE, MULTIDISCIPLINARY | SCOPE NOTE | VIEW JOURNAL SUMMARY LIST | VIEW CATEGORY DATA
COMPUTER SCIENCE, INTERDISCIPLINARY APPLICATIONS | SCOPE NOTE | VIEW JOURNAL SUMMARY LIST | VIEW CATEGORY DATA

Journal Rank in Categories: JOURNAL RANKING

***Eigenfactor*® Metrics**
Eigenfactor® Score
0.00719
Article Influence® Score
0.577

Journal Impact Factor

Cites in 2013 to items published in: 2012 = 180, 2011 = 303, Sum: 483
Number of items published in: 2012 = 166, 2011 = 159, Sum: 325
Calculation: Cites to recent items 483 / Number of recent items 325 = **1.486**

5-Year Journal Impact Factor

Cites in {2013} to items published in: 2012 = 180, 2011 = 303, 2010 = 367, 2009 = 291, 2008 = 404, Sum: 1545
Number of items published in: 2012 = 166, 2011 = 159, 2010 = 149, 2009 = 118, 2008 = 156, Sum: 748
Calculation: Cites to recent items 1545 / Number of recent items 748 = **2.066**

Journal Self Cites

The tables show the contribution of the journal's self cites to its impact factor. This information is also represented in the cited journal graph.

Total Cites	2798	**Self Cites**	383 (13% of 2798)
Cites to Years Used in Impact Factor Calculation	483	**Self Cites to Years Used in Impact Factor Calculation**	104 (21% of 483)
Impact Factor	1.486	**Impact Factor without Self Cites**	1.166

Journal Immediacy Index

Cites in 2013 to items published in 2013 = 28
Number of items published in 2013 = 189
Calculation: Cites to current items 28 / Number of current items 189 = **0.148**

Journal Cited Half-Life

The cited half-life for the journal is the median age of its items cited in the current JCR year. Half of the citations to the journal are to items published within the cited half-life.
Cited Half-Life: 5.6 years

Breakdown of the citations ***to the journal*** by the cumulative percent of 2013 cites to items published in the following years:

Cited Year	2013	2012	2011	2010	2009	2008	2007	2006	2005	2004	2003-all
# Cites from 2013	28	180	303	367	291	404	151	105	242	105	622
Cumulative %	1.00	7.43	18.26	31.38	41.78	56.22	61.62	65.37	74.02	77.77	100

Cited Half-Life Calculations:
The cited half-life calculation finds the number of publication years from the current JCR year that account for 50% of citations received by the journal. Read help for more information on the calculation.

Cited Journal Graph

Click here for Cited Journal data table

This graph shows the distribution by cited year of citations to items published in the journal COMPUT ELECTRON AGR.
Citations to the journal (per cited year)

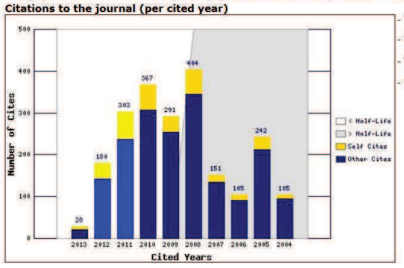

- The white/gray division indicates the cited half-life (if < 10.0). Half of the journal's cited items were published more recently than the cited half-life.
- The top (gold) portion of each column indicates Journal Self Citations: citations to items in the journal from items in the same journal.
- The bottom (blue) portion of each column indicates Non-Self Citations: citations to the journal from items in other journals.
- The two lighter columns indicate citations used to calculate the Impact Factor (always the 2nd and 3rd columns).

Journal Citing Half-Life

The citing half-life for the journal is the median age of the items the journal cited in the current JCR year. Half of the citations in the journal are to items published within the citing half-life.
Citing Half-Life: 8.2 years

Breakdown of the citations ***from the journal*** by the cumulative percent of 2013 cites to items published in the following years:

Cited Year	2013	2012	2011	2010	2009	2008	2007	2006	2005	2004	2003-all
# Cites from 2013	89	389	553	502	475	461	372	362	337	314	2689
Cumulative %	1.36	7.31	15.76	23.43	30.69	37.73	43.42	48.95	54.10	58.90	100

Citing Half-Life Calculations:
The citing half-life calculation finds the number of publication years from the current JCR year that account for 50% of citations in the journal. Read help for more information on the calculation.

Citing Journal Graph

Click here for Citing Journal data table

This graph shows the distribution by cited year of citations from current-year items in the journal COMPUT ELECTRON AGR.

Citations from the journal (per cited year)

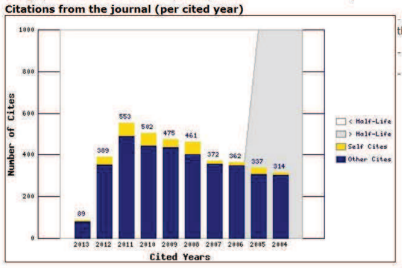

- The white/grey division indicates the citing half-life (if < 10.0). Half of the citations from the journal's current items are to items published more recently than the citing half-life.
- The top (gold) portion of each column indicates Journal Self-Citations: citations from items in the journal to items in the same journal.
- The bottom (blue) portion of each column indicates Non-Self Citations: citations from the journal to items in other journals.

Journal Source Data

	Citable items			Other items
	Articles	Reviews	Combined	
Number in JCR year 2013 (A)	185	4	189	4
Number of references (B)	6124	415	6539	4.00
Ratio (B/A)	33.1	103.8	34.6	1.0

Journal Ranking

For **2013**, the journal **COMPUTERS AND ELECTRONICS IN AGRICULTURE** has an Impact Factor of **1.486**.

This table shows the ranking of this journal in its subject categories based on Impact Factor.

Category Name	Total Journals in Category	Journal Rank in Category	Quartile in Category
AGRICULTURE, MULTIDISCIPLINARY	56	10	Q1
COMPUTER SCIENCE, INTERDISCIPLINARY APPLICATIONS	102	49	Q2

Category Box Plot

For **2013**, the journal **COMPUTERS AND ELECTRONICS IN AGRICULTURE** has an Impact Factor of **1.486**.

This is a box plot of the subject category or categories to which the journal has been assigned. It provides information about the distribution of journals based on Impact Factor values. It shows median, 25th and 75th percentiles, and the extreme values of the distribution.

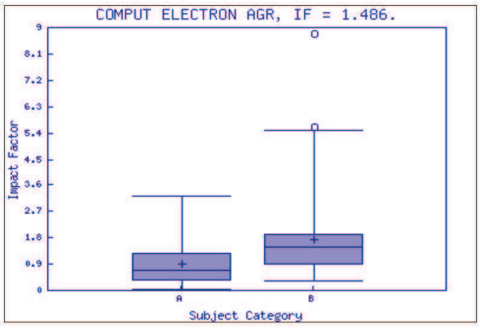

Key
A - AGRICULTURE, MULTIDISCIPLINARY
B - COMPUTER SCIENCE, INTERDISCIPLINARY APPLICATIONS

3. Dense Canopy Height Model from a low-cost photogrammetric platform and LiDAR data

Description of the journal:

Journal:	**TREES-STRUCTURE AND FUNCTION**
URL:	**http://www.editorialmanager.com/tsaf/default.aspx**
Editorial:	**SPRINGER**
ISSN:	**0931-1890**
Impact factor (2014):	**1.651**
Quartile:	**Q1**

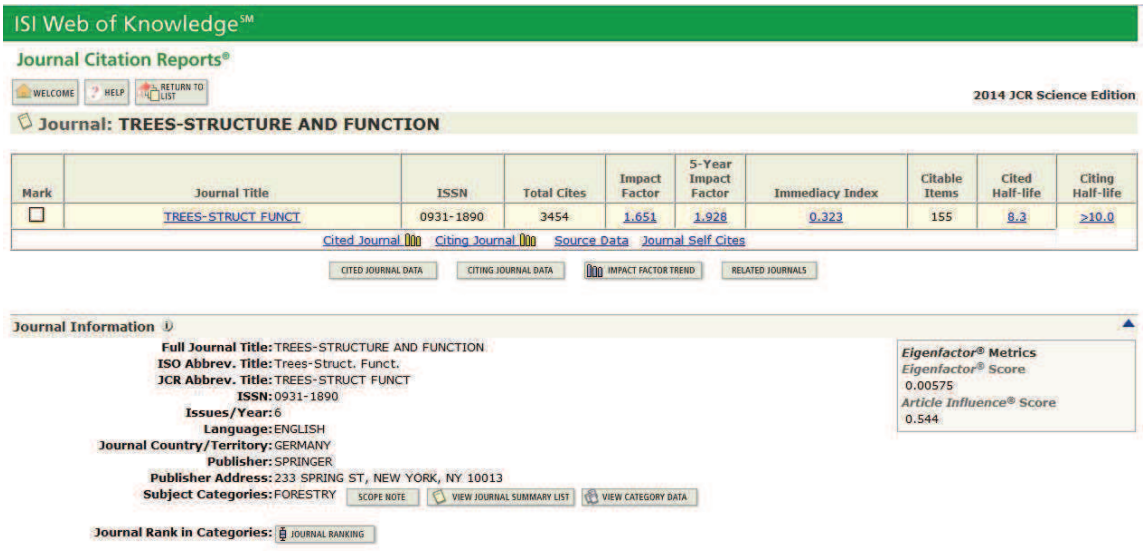

ISI Web of Knowledge℠

Journal Citation Reports®

WELCOME | HELP | RETURN TO LIST

2014 JCR Science Edition

Journal: TREES-STRUCTURE AND FUNCTION

Mark	Journal Title	ISSN	Total Cites	Impact Factor	5-Year Impact Factor	Immediacy Index	Citable Items	Cited Half-life	Citing Half-life
☐	TREES-STRUCT FUNCT	0931-1890	3454	1.651	1.928	0.323	155	8.3	>10.0

Cited Journal | Citing Journal | Source Data | Journal Self Cites

CITED JOURNAL DATA | CITING JOURNAL DATA | IMPACT FACTOR TREND | RELATED JOURNALS

Journal Information

Full Journal Title: TREES-STRUCTURE AND FUNCTION
ISO Abbrev. Title: Trees-Struct. Funct.
JCR Abbrev. Title: TREES-STRUCT FUNCT
ISSN: 0931-1890
Issues/Year: 6
Language: ENGLISH
Journal Country/Territory: GERMANY
Publisher: SPRINGER
Publisher Address: 233 SPRING ST, NEW YORK, NY 10013
Subject Categories: FORESTRY SCOPE NOTE | VIEW JOURNAL SUMMARY LIST | VIEW CATEGORY DATA

Journal Rank in Categories: JOURNAL RANKING

Eigenfactor® Metrics
Eigenfactor® Score
0.00575
Article Influence® Score
0.544

Journal Impact Factor

Cites in 2014 to items published in:	2013 = 210	Number of items published in:	2013 = 158
	2012 = 330		2012 = 169
	Sum: 540		Sum: 327
Calculation: Cites to recent items	540	= **1.651**	
Number of recent items	327		

5-Year Journal Impact Factor

Cites in {2014} to items published in:	2013 = 210	Number of items published in:	2013 = 158
	2012 = 330		2012 = 169
	2011 = 255		2011 = 105
	2010 = 225		2010 = 108
	2009 = 260		2009 = 124
	Sum: 1280		Sum: 664
Calculation: Cites to recent items	1280	= **1.928**	
Number of recent items	664		

Journal Self Cites

The tables show the contribution of the journal's self cites to its impact factor. This information is also represented in the cited journal graph.

Total Cites	3454	**Self Cites**	246 (7% of 3454)
Cites to Years Used in Impact Factor Calculation	540	**Self Cites to Years Used in Impact Factor Calculation**	43 (7% of 540)
Impact Factor	1.651	**Impact Factor without Self Cites**	1.520

Journal Immediacy Index

Cites in 2014 to items published in 2014	= 50		
Number of items published in 2014	= 155		
Calculation: Cites to current items	50	= **0.323**	
Number of current items	155		

Journal Cited Half-Life

The cited half-life for the journal is the median age of its items cited in the current JCR year. Half of the citations to the journal are to items published within the cited half-life.
Cited Half-Life: 8.3 years

Breakdown of the citations ***to the journal*** by the cumulative percent of 2014 cites to items published in the following years:

Cited Year	**2014**	**2013**	**2012**	**2011**	**2010**	**2009**	**2008**	**2007**	**2006**	**2005**	**2004-all**
# Cites from 2014	50	210	330	255	225	260	192	149	176	192	1415
Cumulative %	1.45	7.53	17.08	24.46	30.98	38.51	44.06	48.38	53.47	59.03	100

Cited Half-Life Calculations:
The cited half-life calculation finds the number of publication years from the current JCR year that account for 50% of citations received by the journal. Read help for more information on the calculation.

Cited Journal Graph

Click here for Cited Journal data table

This graph shows the distribution by cited year of citations to items published in the journal TREES-STRUCT FUNCT.

Citations to the journal (per cited year)

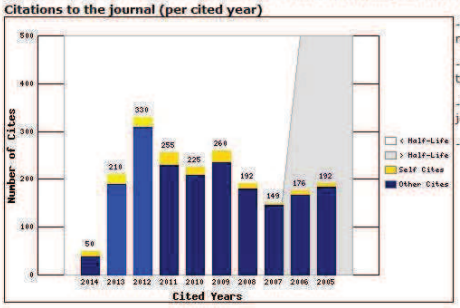

- The white/grey division indicates the cited half-life (if < 10.0). Half of the journal's cited items were published more recently than the cited half-life.
- The top (gold) portion of each column indicates Journal Self Citations: citations to items in the journal from items in the same journal.
- The bottom (blue) portion of each column indicates Non-Self Citations: citations to the journal from items in other journals.
- The two lighter columns indicate citations used to calculate the Impact Factor (always the 2nd and 3rd columns).

Journal Citing Half-Life

The citing half-life for the journal is the median age of the items the journal cited in the current JCR year. Half of the citations in the journal are to items published within the citing half-life.
Citing Half-Life: >10.0 years

Breakdown of the citations ***from the journal*** by the cumulative percent of 2014 cites to items published in the following years:

Cited Year	2014	2013	2012	2011	2010	2009	2008	2007	2006	2005	2004-all
# Cites from 2014	57	317	431	412	432	407	402	379	356	348	4329
Cumulative %	0.72	4.75	10.23	15.46	20.95	26.12	31.23	36.05	40.57	44.99	100

Citing Half-Life Calculations:
The citing half-life calculation finds the number of publication years from the current JCR year that account for 50% of citations in the journal. Read help for more information on the calculation.

Citing Journal Graph

Click here for Citing Journal data table

This graph shows the distribution by cited year of citations from current-year items in the journal TREES-STRUCT FUNCT.
Citations from the journal (per cited year)

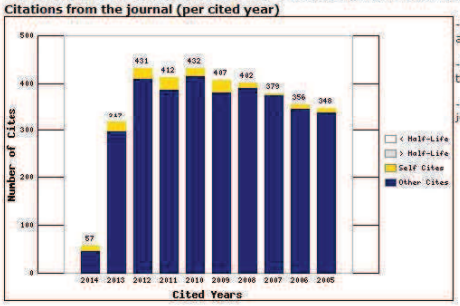

- The white/grey division indicates the citing half-life (if < 10.0). Half of the citations from the journal's current items are to items published more recently than the citing half-life.

- The top (gold) portion of each column indicates Journal Self-Citations: citations from items in the journal to items in the same journal.

- The bottom (blue) portion of each column indicates Non-Self Citations: citations from the journal to items in other journals.

Journal Source Data

	Citable items			
	Articles	Reviews	Combined	Other items
Number in JCR year 2014 (A)	151	4	155	3
Number of references (B)	7635	229	7864	6.00
Ratio (B/A)	50.6	57.2	50.7	2.0

Rank in Category: TREES-STRUCTURE AND FUNCTION

Journal Ranking

For **2014**, the journal **TREES-STRUCTURE AND FUNCTION** has an Impact Factor of **1.651**.

This table shows the ranking of this journal in its subject categories based on Impact Factor.

Category Name	Total Journals in Category	Journal Rank in Category	Quartile in Category
FORESTRY	65	18	Q2

Category Box Plot

For **2014**, the journal **TREES-STRUCTURE AND FUNCTION** has an Impact Factor of **1.651**.

This is a box plot of the subject category or categories to which the journal has been assigned. It provides information about the distribution of journals based on Impact Factor values. It shows median, 25th and 75th percentiles, and the extreme values of the distribution.

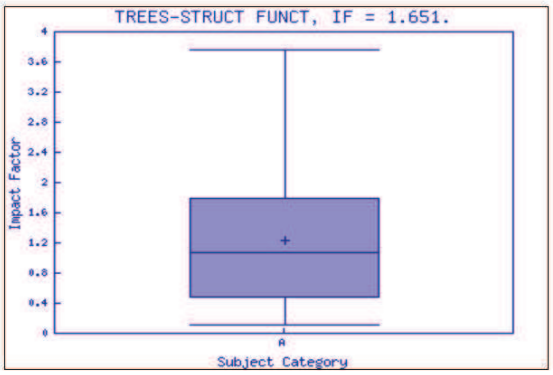

Appendix III

MULRACS software

APPENDIX C. MULRACS SOTWARE

MULRACS-Multispectral Radiometric Calibration Software

Type: Registration of intellectual property

Reference: SA-00/2015/4722

University: University of Salamanca

UNESCO codes:

- 2209.18 Photometry
- 2209.20 Radiometry
- 2209.90 Image Processing
- 3311.11 Optical Instruments

Authors:

- Susana Del Pozo Aguilera
- Mónica Herrero Huerta
- David Hernández López
- Pablo Rodríguez Gonzálvez
- Diego González Aguilera

Abstract:

MULtispectral RAdiometric Calibration Software (MULRACS) developed in Matlab, is a software to radiometrically calibrate passive sensors at close-range distances (unaffected by atmosphere scattering and absorption of solar radiation). It is based on the vicarious calibration process, specifically on the radiance-based method likely to be applied for both mono-spectral and multi-spectral sensors. After the calibration process, geo-referenced images with physical values (reflectance or radiance) and different vegetation index can be generated. These images have a high potential for studies about natural resource surveys, material inspections, precision agriculture… having a strong impact in

the International Scientific Community and private companies in order to perform image analysis. Figure A shows the MULRACS interface.

Characteristics:

MULRACS software is purpose-built to assist the radiometric calibration process and help to effectively manage and control of passive sensors. In that sense, MULRACS software allows performing a rigorous sensor calibration through the vicarious radiance-based calibration method. From multiple artificial targets collected in several images, a robust least squares adjustment is applied, following equation 1.

$$Radiance_i = f(F0_i, F1_i, DN_i) + \Delta\alpha_i \quad (1)$$

where $F0_i$ (offset) and $F1_i$ (gain), are the calibration parameters of the sensor, DN_i is the digital number of the control surface derived from the images and α_i is a correction coefficient, all of them per *i*th channels of the sensor.

The robust estimation chosen is based on Danish Method which iteratively applied weights according to the residual value of each previous iteration in order to dismiss outlier effects.

Inputs:

- ✓ Artificial Lambertian control surfaces
- ✓ Spectral response curve of the control surfaces
- ✓ Quantum efficiency of CCD/CMOS and filters of the passive sensor
- ✓ Collection of images with their capture parameters (focal length, ISO, exposure time and aperture)

Outputs:

- ✓ Radiometric calibration parameters per channel
- ✓ Statistical calibration results
- ✓ Solar irradiance
- ✓ Radiance images
- ✓ Reflectance images
- ✓ Vegetal index images

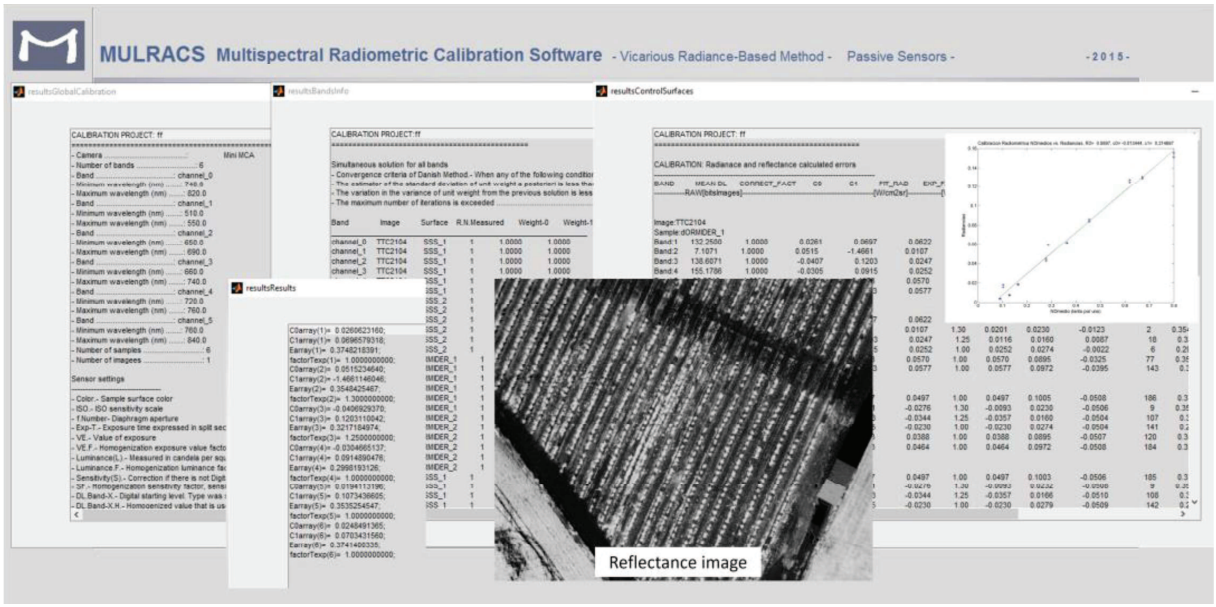

Figure A: MULRACS interface

Appendix IV

Extra merits

APPENDIX D. EXTRA MERITS

1. Iberdrola Cathedra Grant in collaboration with the University of Salamanca (Spain) at TIDOP Research Group. 2011-2012

The fellowship at TIDOP research group within the Department of Cartographic Engineering and Land of the Polytechnic University of Avila, with Diego González Aguilera as tutor, lasted 12 months. It was centered on the study of close-range photogrammetry and multispectral analysis applied to precision agriculture.

2. National Investigation Project Staff: "Energetic Modeling for Smart Cities (Ensmart)". University of Salamanca (Spain). 2013-2014

Reseach staff of EnsMart National Project, with Diego González Aguilera as main researcher, during 2013 and 2014 at the University of Salamanca. It was based on the use of computer vision techniques, close-range aerial photogrammetry, Mobile LiDAR System data and processing of thermal images in urban buildings for energetic modeling.

3. European Investigation Project Staff: "IQmulus: A High-volume Fusion and Analysis Platform for Geospatial Point Clouds, Coverages and Volumetric Data Sets". Delft University of Technology (The Netherlands). 2015

Reseach staff of IQmulus European Project, with Roderik Lindenbergh as main reseacher, during 2015 at Delft University of Technology. The contribution is based on the application of data from Mobile LiDAR System in the characterization of urban trees by creating a bigdata platform.

4. Participation in the "International benchmarking on terrestrial laser scanning methods for forestry". Finnish Geospatial Research Institute (FGI) (Finland). 2015

Participation in "TLS benchmarking 2016" project, with Xinlian Liang, Harri Kaartinen and Juha Hyyppä as main researchers from the FGI. The objective of the benchmarking

project is to evaluate the quality, accuracy, and feasibility of automatic, semi-automatic or manual tree extraction methods based on terrestrial laser scanner data.

5. Participations in the ISPRS congress: SilviLAser, Geospatial Week (France). 2015

Presentation of a methodology to extract geometrical parameters of urban trees through Mobile LiDAR System in the ISPRS Geospatial Week (2015).

6. Guest Researcher at the Institute for Regional Development of Castilla-La Mancha (Spain) in the department of Remote Sensing and Geographic Information System. 2014

The research stay at the Institute for Regional Development of Castilla-La Mancha, with David Hernandez Lopez as tutor, lasted two months (01/07/2014-31/08/2014). It was based on the acquisition and analysis of multispectral images by an alternative aerial platform.

7. Collaboration stay at the Technological University of Delft (The Netherlands) in the department of Geoscience and Remote Sensing. 2015

The research stay at the Delft University of Technology, with Roderik Lindenbergh as tutor, lasted five months (01/02/2015-30/06/2015). This work considered the automated, large scale extraction of tree parameters sampled by a Mobile LiDAR System for direct application in urban tree inventories.

8. Software Development: "MULRACS (MULtispecpectral RAdiometric Calibration of different sensors)". Susana Del Pozo-Aguilera, Mónica Herrero-Huerta, David Hernández-López, Pablo Rodríguez-Gonzálvez and Diego González-Aguilera. 2015

Software for radiometric calibration of passive multispectral close-range sensors.

9. Software Development: ATPE (Automatic Tree Parameter Extraction by mobile LiDAR system). Mónica Herrero-Huerta and Roderik Lindenbergh. 2015

Software for the extraction of tree geometric parameters coming from Mobile LiDAR System data.